Search for multiple neutrino flares from Active Galactic Nuclei with the IceCube Detector

D i s s e r t a t i o n

zur Erlangung des akademischen Grades

d o c t o r r e r u m n a t u r a l i u m

(Dr. rer. nat.)

im Fach Physik

eingereicht an der

Mathematisch-Naturwissenschafltichen Fakultät I

der Humboldt-Universität zu Berlin

von

M.Sc. Angel Humberto Cruz Silva

Präsident der Humboldt-Universität zu Berlin:

Prof. Dr. Jan-Hendrik Olbertz

Dekan der Mathematisch-Naturwissenschaftlichen Fakultät I:

Prof. Dr. Elmar Kulke

Gutachter: 1. Prof. Dr. Elisa Bernardini
2. Prof. Dr. Marek Kowalski
3. Prof. Dr. Elisa Resconi

Tag der mündlichen Prüfung: 04.11.2015

Abstract

Active Galactic Nuclei are among the best candidate sources for high-energy cosmic rays. High-energy neutrinos are expected to be produced in these sources via interactions of cosmic rays with matter or photon fields present in the source vicinity. The resulting neutrino flux may exhibit time variability on the same time scales than the ones observed in the electromagnetic radiation that is emitted from these sources with flare durations ranging from minutes to several days depending on the photon energy.

Time variability can be taken into account in high-energy neutrino searches in order to increase their detection probability with respect to search methods that include only energy and spatial information. In this work, two new methods are developed to look for high-energy neutrino flares emitted from Active Galactic Nuclei: the Multi-flare and Multi-flare stacking method.

The Multi-flare method is designed to be sensitive not only to one bright flare emitted from a single source, as considered in other existing search methods, but also to several weak flares that might not be detected individually. This is achieved by developing a likelihood stacking approach that analyzes the cumulative neutrino emission from several flares. This method does not assume a-priori time coincidences with photon flares observed in the electromagnetic spectrum, allowing uncorrelated neutrino emission with different flare durations as considered in some emission models.

The Multi-flare stacking method is an extension of the Multi-flare method to include several sources that might be too weak for individual detection.

The two search methods are applied to a pre-selected list of Active Galactic Nuclei, composed of Flat Spectrum Radio Quasars and BL-Lacs, using data of the IceCube Neutrino Observatory taken between May-2009 and May-2012. No statistically significant neutrino flares are detected and fluence upper limits are calculated for each selected source. These limits are on average a factor of two better than previous upper limits from single-flare searches.

Keywords: Neutrino, flares, cosmic rays, AGN, IceCube

Zusammenfassung

Aktive galaktische Kerne gehören zu den besten Quellkandidaten der hochenergetischen kosmischen Strahlung. Es wird erwartet, dass hochenergetische Neutrinos durch Interaktion der kosmischen Strahlung mit Materie oder Photonfeldern in der Nähe der Quellen erzeugt werden. Der resultierende Neutrinofluss kann dieselbe Zeitvariabilität aufweisen wie elektromagnetische Strahlung die von diesen Quellen emittiert wird.

Diese Zeitvariabiltät kann in Neutrinoanalysen zusätzlich zu Energie-und Ortsinformationen benutzt werden, um die Detektionswahrscheinlichkeit zu erhöhen. Im Rahmen dieser Arbeit werden zwei neue Methoden entwickelt, welche benutzt werden um nach Neutrinoflares in Aktiven Galaktischen Kernen zu suchen: Die Multi-flare- und Multi-flare-Stacking-Methode.

Die Multi-flare-Methode ist so enworfen, dass sie nicht nur sensitiv auf einen hellen Flare ist, wie es in vorherigen Methoden der Fall gewesen ist, sondern auch auf weitere schwächere Flares welche normalerweise individuell nicht detektiert werden können. Dies wird durch einen likelihood Ansatz erreicht welcher effektiv den kumulativen Neutrinofluss mehrerer Flares analysiert. Die Multi-Flare-Methode benötigt keine Zeitkoinzidenz mit Ausbrüchen im elektromagnetischen Spektrum. Sie ist auch sensitiv auf unkorrelierterNeutrinoemission mit unterschiedlicher Dauer der einzelnen Flares, was in einigen Emissionsmodellen vorkommt.

Die Multi-Flare-Stacking-Methode ist eine Erweiterung der Multi-Flare-Methode auf zusätzliche Quellen. In ihr werden mehrere schwache, variable Quellen, welche individuell zu schwach sein können um detektiert zu werden, zusammen mit der Stackingmethode analysiert.

Die beiden Analysemethoden werden auf eine vorselektierte Liste von Aktiven Galaktischen Kernen angewandt, welche aus Flat Spectrum Radio Quasaren und BL-Lac Objekten besteht. Hierfür werden drei Jahre Daten des IceCube Neutrinoteleskops verwendet, welche zwischen 2009 und 2012 aufgezeichnet wurden. Kein statistisch signfikanter Neutrinoflare wurde gefunden und obere Fluenzgrenzen für jede der Quellen werden ausgerechnet. Diese Grenzen sind im Durchschnitt um einen Faktor zwei besser als vorherige Obergrenzen von Analysen einzelner Flares.

Schlagwörter: Neutrino, Strahlungsaus-brüche, Kosmische Strahlung, AGN, IceCube

Contents

Chapter 1

Introduction

The origin of ultra-high-energy cosmic rays (UHECR), protons and heavier nuclei with energies $\gtrsim 10^{19}$ eV, remains unknown more than 50 years after their discovery [1, 2]. Several astrophysical objects have been proposed as candidate sources of UHECR [3]. One of the most promising candidates are Active Galactic Nuclei (AGN); galaxies known to be powerful emitters of electromagnetic radiation in a wide range of wavelengths going from radio frequencies to TeV gamma-rays. Proton acceleration may take place at several possible sites within the AGN structure such as at the magnetosphere of the super-massive black hole located at its center [4] or at relativistic jets present in some of this objects [5].

The trajectories of charged particles are deflected due to the presence of extra and intergalactic magnetic fields, making it difficult to trace back the location of their source based on measurements of their arrival direction at Earth. These deflections might be small for UHECR, but the lack of conclusive evidence of spatial correlation of the their arrival directions with the positions of known AGN, makes the evidence of UHECR production in this kind of sources to remain elusive [6, 7].

Another approach to look for evidence of proton acceleration in astrophysical objects consists in the detection and study of the energy spectra of high-energy neutrinos and gamma-rays. According to the so called hadronic models, these particles are expected to be produced in collisions of high-energy protons with photon or matter fields present in the vicinity of the source [5, 8, 9]. Since these particles are neutral, they are unaffected by magnetic fields and their arrival directions would point back to the source location.

Particular features of the the gamma-ray energy spectra of astrophysical objects may provide evidence of hadronic interactions as in the case of recent observations of Super Nova Remnants [10]. However, this is not always easy to accomplish since gamma-rays can also be produced in leptonic models via interactions of accelerated electrons with photon target fields present in the object environment. The gamma-ray energy spectra of several AGN can be well described by both leptonic and hadronic models [9]. The detection of high-energy neutrinos would provide complementary evidence of the existence of hadrons being accelerated in these objects [11].

The IceCube Neutrino Observatory is one of the experiments that have looked for this evidence during the past few years. It consists of 5160 light sensors installed in the ice

at the geographic south pole occupying an instrumented volume of 1 km^3 [12]. Neutrino interactions with the nuclei of the surrounding ice or the nearby bedrock produce secondary charged particles that induce Cherenkov light. The direction and energy reconstructions of neutrino-induced events are based on the detection of this light. These reconstructions have been used in several searches of a localized excess of events above the atmospheric neutrino and muon background generated by interactions of cosmic rays with nuclei of the Earth atmosphere. So far, these searches have not resulted in a statistical significant detection of a localized astrophysical neutrino flux [13, 14, 15].

Another kind of approach looks for an excess of events over the atmospheric background focusing on their energy distribution without requiring a localized excess i.e it looks for a diffuse flux. The very first evidence of this kind was provided by the IceCube Collaboration, detecting at the 5.7σ level a flux of high-energy neutrinos of astrophysical origin [16, 17]. Recently, some AGN have been considered as plausible counterparts of these events [18]. However, given the uncertainties in the arrival directions of most of the detected events, their spatial distribution is consistent with an isotropy and therefore no association with an astrophysical object has been made yet.

AGN are known to emit photon flares at different wavelengths and in various time scales, ranging from minutes in TeV gamma-rays [19, 20] to several days in the GeV band [21]. If this radiation is produced in hadronic interactions, the associated neutrino emission may exhibit similar time variability. One way to increase the detection probability of high-energy neutrinos emitted from these sources is to include in the search method the arrival time information of the events since by looking at short time windows the atmospheric background decreases.

Search methods that include time information are known as time-dependent methods. One of these methods, developed elsewhere, aims to find a single bright neutrino flare located at any point in the sky or at locations of selected AGN [22, 23, 24]. The method is referred as an un-triggered search since it does not consider a photon counterpart a-priori. Another method takes into account information extracted from photon observations for a given source, for example gamma-rays detected in the GeV or TeV energy range, in order to define time windows where neutrinos are expected simultaneously to the photon flares. These approach is referred a triggered search [22, 23].

In this thesis two additional time-dependent methods were developed and applied to IceCube data taken between May-2009 and May-2012 using a a pre-selected list of AGN as candidate sources. The first method is sensitive to a set of neutrino events which might form not only a single flare, as assumed in the un-triggered search, but are distributed in several weak flares that might not be detected individually [25]. These multiple neutrino flares are not assumed a-priori to be synchronous with photon flares as considered in triggered searches. The developed search method therefore allows to find several neutrino flares of different durations with no photon counterparts as proposed in some emission models [26, 27].

Since individual sources might be too weak for individual detection, a second method

was developed to look for an accumulated neutrino emission from several flaring AGN. In this approach the number of events a single source would have to emit in order to reach the discovery threshold is less than if the source is analyzed individually.

Chapter 2 gives a short overview on cosmic ray observations and a description of the cosmic ray interactions that would produce high-energy neutrinos, together with a brief description of several astrophysical objects that are proposed in the literature as cosmic ray and high-energy neutrino sources. Chapter 3 focuses on AGN and their phenomenology ending with a description of the criteria to select a list of flaring AGN, to be tested with the search methods developed in this thesis. Chapter 4 presents the field of neutrino astronomy describing the principle of operation of a neutrino telescope and the main sources of background. Chapter 5 describes the IceCube Neutrino Observatory, the direction and energy reconstruction methods and the event selection steps to generate the data samples to be used. Chapter 6 presents the statistical tools that is the basis of the search methods developed in this thesis which are described in detail in Chapter 7. Finally, Chapter 8 shows the results of applying these methods to the pre-selected AGN and Chapter 9 presents the summary and outlook of this work.

Chapter 2

Cosmic Rays and High-Energy Neutrinos

The main features of cosmic rays and the general models for acceleration mechanisms are summarized in this chapter. After a description of the cosmic ray interactions that are expected to produce high-energy neutrinos, several candidate sources of cosmic rays and neutrinos are briefly described.

2.1 Cosmic Rays

Cosmic rays consist on a flux of charged particles such as electrons, protons and heavier nuclei arriving to the Earth atmosphere. They were discovered more than 100 years ago and up to now their origin is not completely understood. Several experiments have studied cosmic ray phenomena by measuring for example their energy spectrum at different energies. In the following the main features of cosmic rays are briefly described.

2.1.1 Cosmic Ray Spectrum

Figure 2.1 shows the flux of cosmic rays as a function of their kinetic energy as measured by different experiments. In general the cosmic ray spectrum follows a power law:

$$\frac{dN}{dE} \propto E^{-\gamma_{cr}}, \tag{2.1}$$

where N is the number of particles per unit of area and per unit of time and γ_{cr} is referred as the spectral index. The power law behavior can be explained in terms of shock acceleration as described in the next section.

There are several features in the cosmic ray energy spectrum visible as changes in the spectral index γ_{cr} at different energies. At energies above $E > 10^{14}$ eV the cosmic ray flux has been measured indirectly by ground-based detectors. This is achieved via the detection

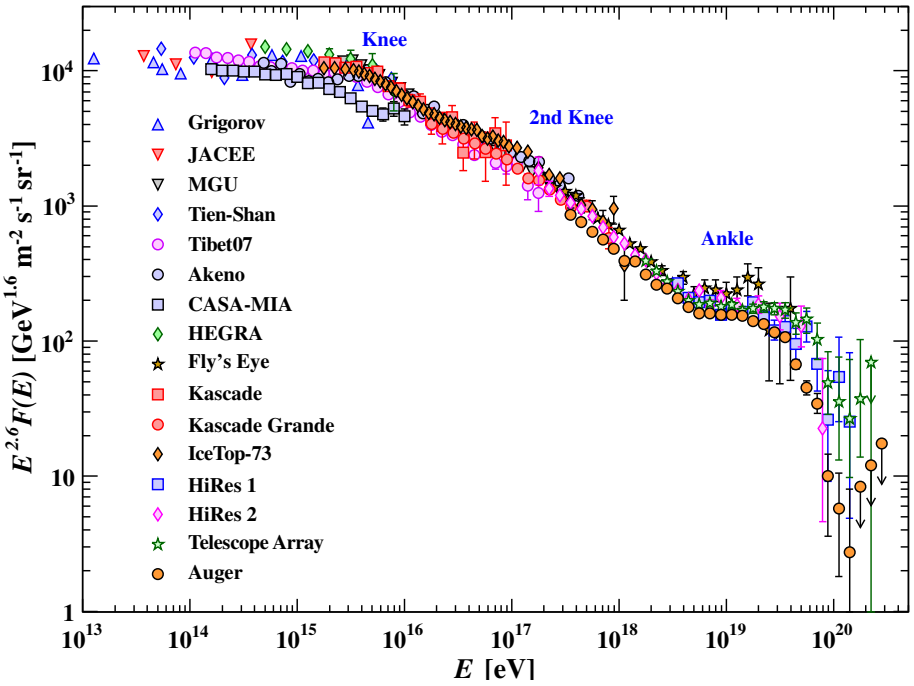

Figure 2.1: Cosmic ray spectrum as measured by different air shower experiments. Several features appear as a change in the slope (spectral index of a power law) labeled as the knee, 2nd knee and the ankle. Taken from [28].

of air showers of secondary particles produced in interactions with the nuclei of the Earth atmosphere. At these energies the cosmic ray flux decreases steeply ($\gamma_{cr} \approx 2.7$) up to the feature known as the "knee" located above $E \approx 3 \times 10^{15}$ eV where the spectral index change to $\gamma_{cr} \approx 3.10$.

Cosmic rays with energies below and around the knee are believed to be mainly of galactic origin. This is because the energy range around the knee can be associated with the maximum energy galactic accelerators such as Super Nova Remnants and binary systems (briefly described in section 2.3) could provide in acceleration of charged particles such as protons and helium nuclei. [3, 29]. Another feature known as the second knee is seen at $E \approx 4 \times 10^{17}$ eV which is interpreted in terms of the maximum energy achieved in galactic accelerators for heavier nuclei (Actinides) [30].

Ultra-high-energy cosmic rays (UHECR) are detected at energies around and above 3×10^{18} eV where a feature known as the ankle is visible. This feature is commonly interpreted as the the effect of a population of cosmic rays produced in extra-galactic sources, such as AGN and Gamma-Ray-Bursts (see section 2.3), starting to dominate the spectrum [32, 33]. The last feature in the cosmic ray spectrum is a rapid decrease of the particle flux at energies above 5×10^{19} eV. This feature could be associated with the suppression of cosmic rays due to interactions with cosmic micro-wave background

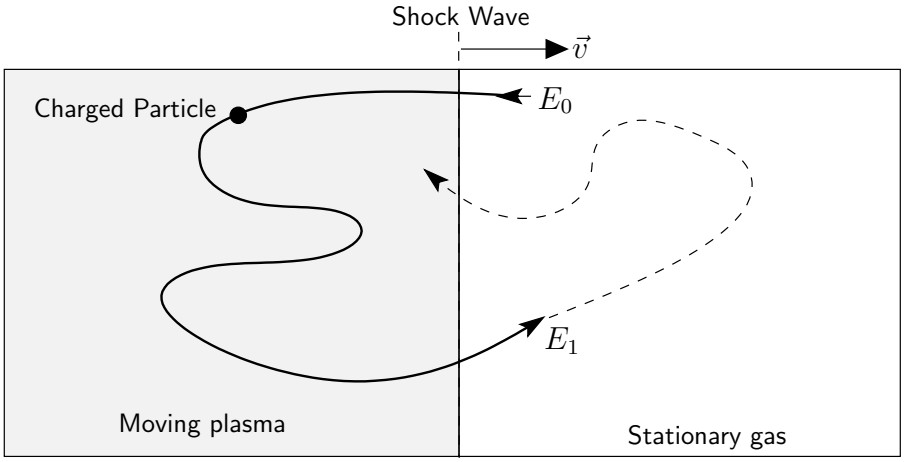

Figure 2.2: Sketch of the diffusive shock acceleration mechanism. A charged particle with initial energy E_0 crosses a shock front that propagates at a supersonic velocity $\vec{v}$. After being scattered by an inhomogeneous magnetic field the charged particles achieves a constant energy gain $(E_1 - E_0)/E_1 \propto |\vec{v}|/c$ when it crosses again the shock front. This process is repeated until the charged particle escapes the magnetic confinement [31].

photons (CMB) also referred as the GZK (Greisen-Zatsepin-Kuzmin) cut-off [34]. In these interactions cosmic rays lose energy either by the production of a Δ-resonance or by direct electron-positron pair production. The mean free path for this interactions at energies around 10^{18} eV is about 200 Mpc and therefore sources located at larger distances should not contribute significantly to the flux of UHECR at Earth [6].

Another interpretation of the rapid decrease at these energies is that the high-energy cosmic ray sources run out of acceleration power and cannot produce particles of higher energies [2, 3].

2.1.2 Acceleration Mechanism

One of the most popular models for particle acceleration in astrophysical environments is known as diffusive shock acceleration, also referred as first-order Fermi acceleration mechanism. A first version of such mechanism was proposed by Enrico Fermi in 1949 [36] and revisited by several authors in the late 1970s [37, 38]. This model is based on the idea that several astrophysical phenomena can be described by the collision of moving plasmas that generates disturbances in the plasma density known as shock fronts which move at supersonic speeds. Figure 2.2 illustrates the acceleration mechanism: a charged particle pass several times through a shock front, moving at a velocity v, due to the influence of a turbulent magnetic field scrambling its trajectory. In a single crossing the particle gains a fraction of energy proportional to $\beta = v/c$. This process continues until enough energy is obtained for the particle to escape the magnetic field confinement.

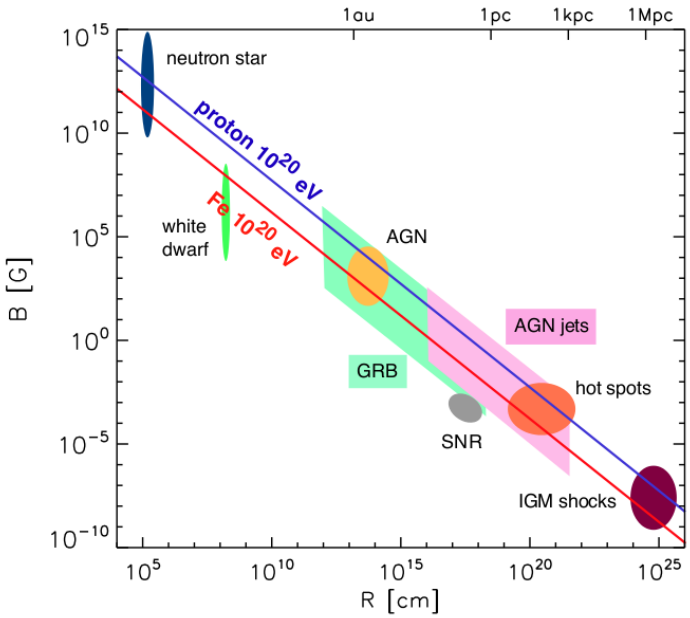

Figure 2.3: Updated Hillas Plot (taken from Ref. [3] which shows an update of the original plot found in Ref. [35]). The uncertainties in the acceleration size R and the magnetic field B estimated for different astrophysical objects are shown in the colored regions. Above the blue (red) line protons (Iron nuclei) the maximum acceleration energy is $E_{\text{max}} \geq 10^{20}$ eV (see Eq. 2.2).

Once the probability that the charged particle does not escape the acceleration region in a single crossing is taken into account, the final outcome of this process is a power law energy spectrum for the accelerated particles with spectral index $\gamma_p = 2$ for non-relativistic shocks and between 2.1 and 2.4 for relativistic shocks [39, 2]. Detailed Monte Carlo simulations predict a softer ($\gamma_p > 2$) or a harder ($\gamma_p < 2$) spectrum depending on the conditions of the astrophysical environment such as the level of magnetic turbulence [40] or the presence of multiple shock fronts propagating at different velocities [41].

The observation at Earth of cosmic rays with an even softer spectrum ($\gamma_{cr} \approx 2.7$) is commonly interpreted as the effect of charged particles at higher energies escaping the Milky-Way galaxy since they are not longer confined by the galactic magnetic field which is estimated to be of the order of a few μG [32].

If the Larmor radius of a particle is larger than the size of the acceleration region R the particle escapes this region. This sets a limit on the maximum energy a charged particle can gain given by the Hillas condition [35] which for the case of relativistic shocks is [39]:

$$E_{\text{max}} = \Gamma \beta Z e B R, \tag{2.2}$$

where Γ is the Lorentz factor, Z is the charge of the particle in units of the electron charge

e and B is the magnitude of the magnetic field present in the particular astrophysical object being considered.

Figure 2.3 shows the so-called Hillas plot in which the parameter space for the size of the acceleration region and the magnitude of the magnetic field is shown for different astrophysical objects including the uncertainties in these parameters (colored regions). The Hillas condition for $E_{\text{max}} = 10^{20}$ eV ($\beta \approx 1$) is satisfied at the regions above the blue (protons) and red (Iron Nuclei) lines. The AGN parameter space is illustrated in this plot for different proposed acceleration regions within the AGN structure[1]: jets (pink region), hot spots (orange region) and nuclei (yellow region). Some regions of the AGN parameter space satisfy the Hillas condition and therefore this objects have been considered since long good candidates for sources of UHECR. Other candidate objects include Gamma-Ray-Bursts (GRB) and neutron stars which are described briefly on section 2.3.

2.1.3 Cosmic Ray Astronomy

Experimental evidence is still required to establish the sources of high-energy cosmic rays. A natural idea for this kind of evidence is to look at the arrival direction of the observed cosmic rays and investigate space correlations with known astrophysical objects. However, this can only be done for UHECR since the trajectories of cosmic rays are deflected by the presence of interstellar magnetic fields [42] and this deflection is small for UHECR[2]

In 2007 the Pierre Auger Collaboration announced evidence for correlation of the arrival directions of 27 UHECR with the locations in the sky of known AGN which reached maximum significance for around 400 sources located at distances less than 71 Mpc from the Earth [44]. This correlation was not confirmed by a similar analysis using data of the HiRes telescope [45]. Figure 2.4 shows the arrival direction of UHECR detected by these two experiments together with the position of the ~ 400 AGN. The significance of the correlation decreased by a factor of two by using the arrival directions of new UHECR detected by the Pierre Auger Observatory (69 in total). The data is still inconsistent with isotropy at the 99% confidence level but with the current data no claim can be made on AGN being the sources of UHECR [6].

2.2 High-Energy Neutrinos

Charged particles accelerated in astrophysical environments may interact with target fields present in the vicinity of these objects. Two target fields are considered in theoretical models of these environments: photon radiation fields (proton-photon models) and ambient gas material (proton-Nuclei or proton-proton models).

[1] The AGN structure is discussed in detail in chapter 3

[2] For protons with energies around 10^{19}eV the deflection is less than 3° for a magnetic field of 1nG [43]. However, it should be noted that deflections in the extragalactic magnetic fields could be much larger ($\sim 15^{\circ}$) according to some calculations [2].

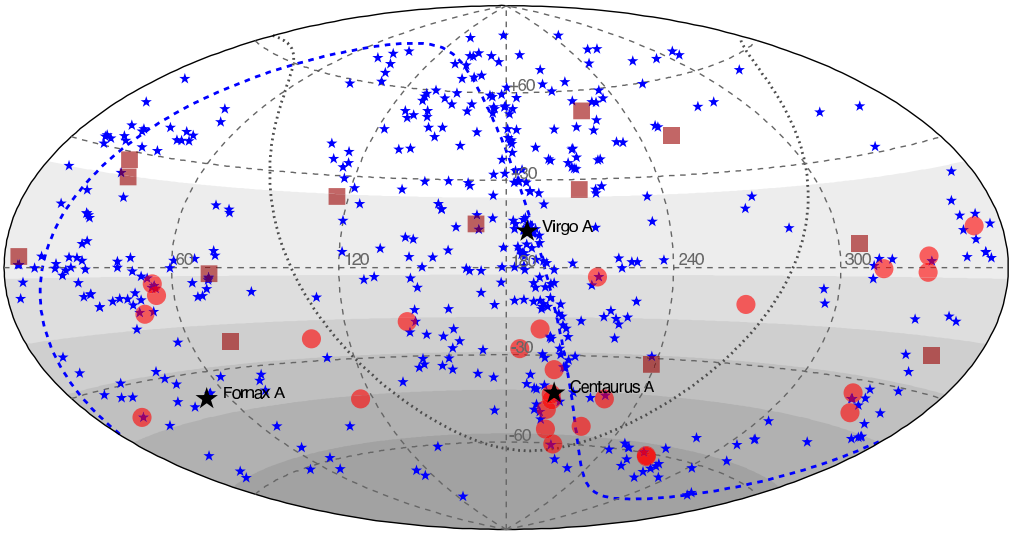

Figure 2.4: Arrival directions in equatorial coordinates of the UHECR observed by the Pierre Auger Observatory (circles) and the HiRes telescope (squares). The blue stars show the positions of ~ 400 known AGN at distances less than 71 Mpc from the Earth for which the analysis provided the largest significance [44], although no claim was done on AGN being the sources of UHECR. No significant correlation was seen by the HiRes telescope [45]. Taken from [32].

The main channel for inelastic collisions of high-energy protons with photon fields is the direct production of electron-positron pairs ($p + \gamma \rightarrow e^+ + e^- + p$) [4]. The cross section for this process, also know as the Bethe-Heitler pair production, is two orders of magnitude larger than the photo-meson production [46] in which π-mesons are produced in the decay of the produced $\Delta(1232)$-resonance:

$$p + \gamma \rightarrow \Delta^+ \rightarrow n + \pi^+ \text{ in } 1/3 \text{ of the cases,} \tag{2.3}$$

$$p + \gamma \rightarrow \Delta^+ \rightarrow p + \pi^0 \text{ in } 2/3 \text{ of the cases.} \tag{2.4}$$

Even with a smaller cross section, this process is the main energy loss process for high-energy protons since on average only a small fraction of the proton energy is transferred to the positron-electron pairs while in the case of photo-meson production the proton can transfer $> 13\%$ of its energy to the secondary products [46]. Additional pions can be generated from second order channels such as the decay of resonances at higher masses (N(1440) ... $\Delta(1700)$, etc), direct-pion production, multi-pion production and Kaon decays, where the last two processes become dominant at high energies of the incoming proton. [47, 48].

For the second interaction channel i.e collisions with nuclei of the ambient material N,

mesons are also produced via:

$$p + N \rightarrow \pi^+ + \pi^- + \pi^0, \tag{2.5}$$
$$p + N \rightarrow K^+ + K^- + K^0. \tag{2.6}$$

In these interactions heavier particles such as D-mesons and Λ_c^+ particles are produced at a lower rate but can become dominant at high proton energies. If the density of the ambient medium is sufficiently low the pions produced in both interaction channels decay before further interaction with other particles into neutrinos and gamma-rays:

$$\pi^+ \rightarrow \mu^+ + \nu_\mu, \tag{2.7}$$
$$\pi^- \rightarrow \mu^- + \bar{\nu}_\mu, \tag{2.8}$$
$$\pi^0 \rightarrow \gamma + \gamma. \tag{2.9}$$

The subsequent muon decay provides an addional neutrino flux:

$$\mu^+ \rightarrow e^+ + \nu_e + \bar{\nu}_\mu, . \tag{2.10}$$

Depending on the theoretical model considered there could be additional contributions to the neutrino flux such as neutrinos from the decay of the neutrons (see Eq. 2.3):

$$n \rightarrow p + e^- + \bar{\nu}_e, \tag{2.11}$$

and neutrinos product of the decay chain of heavier mesons (see Eq. 2.6):

$$\begin{aligned} K^\pm &\longrightarrow \mu^\pm + \nu_\mu(\bar{\nu}_\mu) && (63.55\%), && (2.12)\\ &\longrightarrow \pi^\pm + \pi^o && (20.66\%),\\ &\longrightarrow \pi^+ + \pi^\pm + \pi^\pm && (5.59\%),\\ &\longrightarrow \pi^0 + \mu^\pm + \nu_\mu(\bar{\nu}_\mu) && (3.35\%),\\ D^\pm &\longrightarrow \mu^\pm + \nu_\mu(\bar{\nu}_\mu) + X, && (17.2\%), && (2.13)\\ \Lambda_c^+ &\longrightarrow \Lambda + \mu^+ + \nu_\mu, && (2.0\%) && (2.14)\\ &\longrightarrow e^- + \nu_e, && (2.1\%) \end{aligned}$$

where the corresponding branching ratios are quoted in parentheses. The magnitude of the contribution from Kaon decay chains to this neutrino flux depends on the assumptions made in each model like for example which target field is considered [47, 48, 49]

The decay of neutral and charged pions (Eqs. 2.7,2.8, 2.9) ilustrates the connection between high-energy neutrinos and gamma-rays as this two messengers would be produced in different decay channels of the same hadronic interactions. Since high-energy gamma-rays can also be produced by leptonic process i.e by the interactions of high-energy electrons at the source (see section 3.2), their mere detection does not guarantee that the hadronic interactions described in this section take place. High-energy neutrinos could provide unambiguous evidence of hadronic acceleration in these sources.

In the GZK scenario high-energy protons interact with the cosmic micro-wave background ($p + \gamma_{CMB}$) producing the secondaries described above i.e $e^{\pm}$ pairs and π-mesons. The rapid decrease observed in the cosmic ray spectrum at the highest energies (see Figure 2.1) can be interpreted as the observable consequence of the photo-production of π-mesons [31, 3]. A high-energy neutrino flux from these interactions is refered as a cosmogenic neutrino flux which is predicted to peak at around 1 EeV but has not been observed yet [11].

The energy spectra of neutrinos emmited in these and other potential sources have been calculated in several theoretical approaches taking into account the relevant decay chains and energy losses for various astrophysical enviroments. In the case of proton-proton interactions taking place in the vicinity of objects such as AGN, the energy spectrum of astrophysical neutrinos follows at first approximation the energy spectrum of the parent cosmic rays producing them, [50] while in proton-photon interactions the energy spectrum reflects the spectrum of the target photons [51, 48]. In these models high-energy neutrinos are predicted to be emitted with an energy spectrum peaking in the TeV-PeV range.

Neutrino flavor ratio

The benchmark neutrino production scenario due to pion decays (Eqs. (2.7) (2.10)), results in a neutrino flavor ratio $\nu_e : \nu_\mu : \nu_\tau = 1 : 2 : 0$. Other theoretical scenarios predict a different initial flavor ratio that depends on the interaction channel and on the energy range considered [52, 53]. One example of these kind of scenario is known as the muon-damped mode in which muons produced in pion-decays (Eq. 2.7) lose energy before it decays in further interactions with the environment, such as a field of target photons. The ν_e and $\bar{\nu}_\mu$ contributions from its decay (Eq. 2.10) are therefore suppresed. Pions on the other hand have a life time two orders of magnitude smaller than muons and therefore they almost always decay before interacting. The initial flavor ratio of the emitted neutrino flux in this case is $\nu_e : \nu_\mu : \nu_\tau = 0 : 1 : 0$.

As discussed in section 4.1 the neutrino flavor changes during its propagation to the Earth due to neutrino oscillations. The benchmark production scenario with an initial flavor ratio of $1 : 2 : 0$ therefore becomes $1 : 1 : 1$ at the Earth. This ratio change if other scenarios, like the one described above, take place at the source [52, 49, 53].

2.2.1 First Evidence of an Astrophysical Neutrino Flux

As will be discussed in section 4.3, the background in analyses aiming to find evidence of astrophysical neutrinos consists is a flux of secondaries refered as atmospheric neutrinos and muons. This secondaries are produced in the same interactions for the proton+Nuclei case presented above when cosmic rays arriving to the Earth interact with nuclei of the atmosphere. The first evidence of an astrophysical neutrino flux was provided by the IceCube Collaboration in 2013 by observing 28 neutrino candidate events in two years of data where around 10 events are expected from atmospheric backgrounds [16]. Figure 2.5

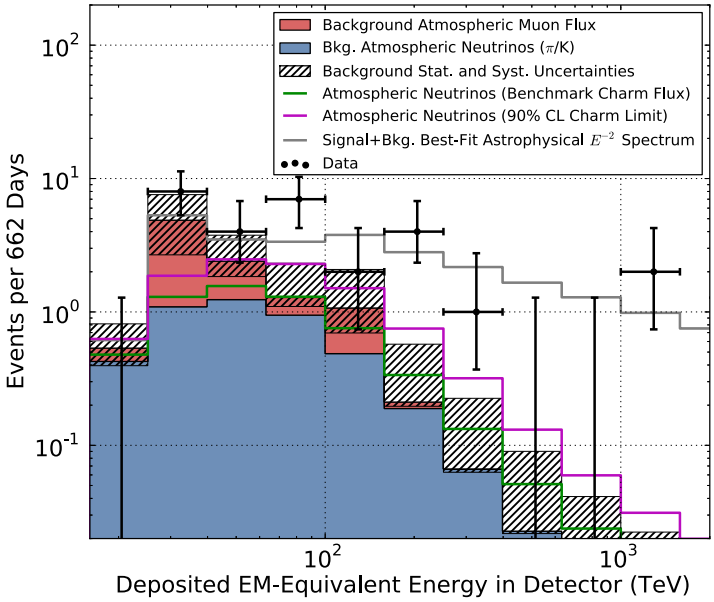

Figure 2.5: Energy spectrum of the events detected by the IceCube Neutrino Observatory in two years of data. An excess of events is observed above the atmospheric background at deposited energies above 100 TeV. Taken from [16].

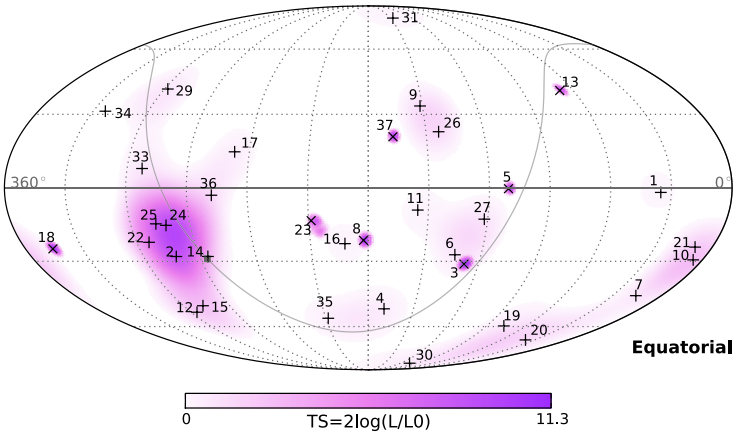

Figure 2.6: Arrival directions of the events observed in two years of data of the IceCube Neutrino Observatory in galactic coordinates together with an estimation of the significance of their clustering in terms of a test statistic TS (color bar). Approximately 40% of the events are expected to originate from atmospheric backgrounds. No significant clustering in space was found. Taken from [16].

shows the energy spectrum of the observed events where and excess over the estimated background is seen at high energies. A follow-up analysis, which uses an additional year of data rejects at the 5.7σ level a pure atmospheric origin of the observed events [17]. Assuming a power law of the energy spectrum the best fit spectral index is $\gamma = 2.3 \pm 0.3$.

The study of the arrival directions of the observed events did not show a significant space clustering (see Figure 2.6) and therefore their distribution is consistent with an isotropic flux [17]. The source of these astrophysical neutrinos is still unknown. It is worth to note that most of the detected events have angular resolutions up to 15° and therefore are not well suited for point source searches [3]

An additional analysis of the IceCube data, designed to observe the diffuse astrophysical neutrino flux down to 35 TeV, resulted in the first contraints of the neutrino flavor ratio at Earth. While the data is consistent with the benchmark neutrino flavor $1:1:1$ other scenarios, such as $0:1:0$ and $1:0:0$, are excluded at the $2-3\sigma$ level [54].

2.3 Candidate Sources of Cosmic Rays and High-Energy Neutrinos

2.3.1 Galactic Candidate Sources

Super Nova Remnants (SNR)

Super Nova Remnants result from the explosion of aging stars. This explosion generates a plasma with velocities up to 10% the speed of light which interacts with interstellar media, such as molecular clouds, resulting in the formation of shock fronts in which hadrons could be accelerated. SNR are usually considered as being the dominant sources of cosmic rays up to the knee feature at energies around 3 PeV [29].

So far around ten Super Nova Remnants have been observed in the TeV range [55], however, this is not enough evidence of effective hadron acceleration and subsequent photon emission produced in pion decays (Eq. 2.9). Accelerated electrons could also generate gamma-rays in the TeV range via bremsstrahlung or inverse compton scattering of low energy photons.

Figure 2.7 shows the energy spectrum of the SNR IC 443 at energies above 100 MeV together with different model fits [10]. The data match the characteristic energy spectrum of gamma-rays produced in pion decays providing direct evidence of pion production in these sources and therefore evidence of proton acceleration. Despite this evidence high-energy neutrinos in the direction of SNRs have not been detected [14, 15, 56].

[3] The concept of a point source search using events with sub-degree angular resolutions is described in chapter 4.

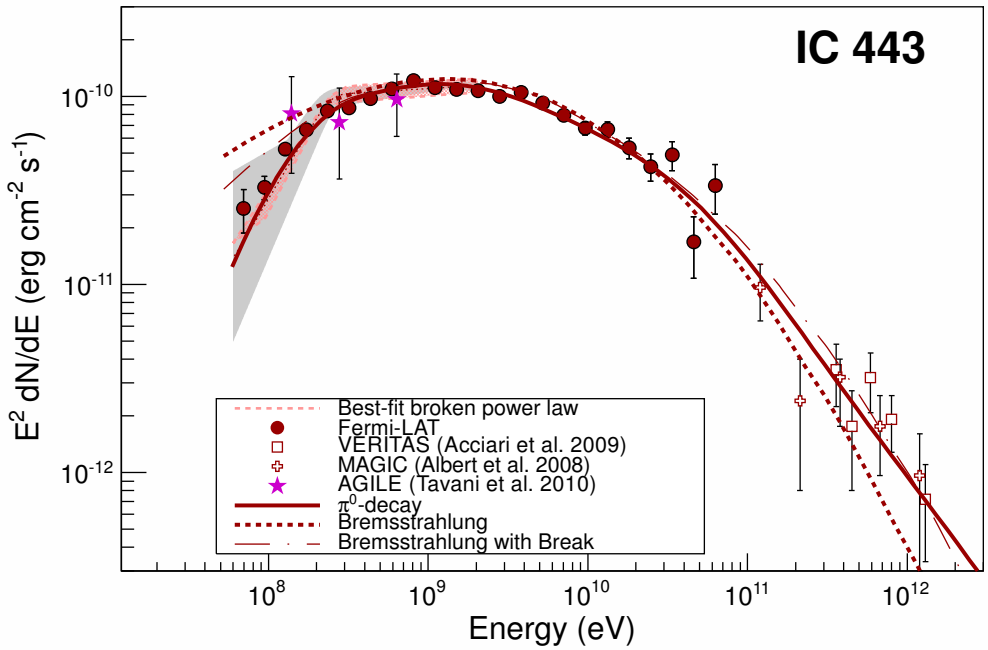

Figure 2.7: Gamma-ray energy spectrum of the SNR IC443. The solid red line is the gamma-ray spectrum produced in neutral pion decays and the red dots are the experimental data measured by the Fermi Large Area Telescope (Fermi-LAT). This observation provides the first direct evidence of proton acceleration in SNRs. Plot taken from [10].

Microquasars and X-ray Binaries

Binary sistems are composed of a compact object (a black hole or neutron star) accreeting material provided by a companion star. High-mass X-ray binaries (HMXB) have a star with a mass of about $10 - 20$ solar masses whereas low mass X-ray binaries (LMXB) have a companion of a mass comparable with the Sun [31]. Besides being know as X-ray sources some of these objects are also TeV gamma-ray sources. Hadronic interactions could be produced by protons being accelerated in the high magnetic field provided by the compact object colliding with the accreting material from the companion star.

Microquasars are a class of X-ray binaries where relativistic jets are produced. These jets could be responsible of particle acceleration via the Fermi mechanism. These systems are variable radio sources exhibiting bursts of activity on timescales of several days . Neutrinos could be produced in the same burst providing a time-dependent neutrino signal. Recent observations by the IceCube Neutrino Observatory have not detected a neutrino flux from selected microquasars [22, 23].

Soft Gamma-ray Repeaters

Soft Gamma-ray repeaters are objects that exhibit a periodic X-ray emission with periods up to 10 seconds and high luminosity bursts of about 1 second observed in GeV gamma-rays. The most popular model for this kind of objects is a neutron star producing a very high magnetic field, on the order of 10^{15} G. The bursts are usually interpreted as being produced in re-arrangements of the magnetic field in which hadrons could be accelerated [57, 58].

2.3.2 Extra-Galactic Candidate Sources

Gamma-Ray-Burst (GRBs)

GRB are among the most energetic explosions in the universe. They release in a few seconds a similar amount of energy than the Sun will emit in 10 billion years. GRBs are typically observed first in photons at the keV-MeV band with a spectrum following a broken power law i.e the energy spectra is modeled with two power law functions each one with a different spectral index [59]. This emission is followed by a decaying photon emission observed in radio and X-rays [60].

The origin of GRBs is still unknown. Core collapse Super Nova are the pressumed progenitors for GRBs of duration of more than 2 seconds while GRBs of shorter durations are believed to be produced in the merging of two black holes or two neutron stars. Highly relativistic shock fronts formed in this explosions could accelerate cosmic rays above 10^{17} eV and high-energy gamma-rays and neutrinos would be produced by the intreractions of this accelerated charged particles with the keV-MeV photon field [61, 62]. A recent non-detection of high-energy neutrinos from GRBs by the IceCube Neutrino Telescope contrained the parameter space for efficient neutrino and UHECR production [63]. However, a revisit of neutrino production model predicts a high-energy neutrino flux an order of magnitude lower than previously considered and therefore GRBs might not be ruled out yet as sources of UHECR [64].

Star-burst Galaxies

Well known as being sources of photons in far infra-red Starburst galaxies have a higher star formation rate compared to regular galaxies. This implies a higher rate of SuperNova explosions which collective effect could be an enhacement in the flux of cosmic rays and neutrinos [62, 65, 66, 67]. However, high-energy neutrinos from these sources have not been detected [14, 15, 56].

Active Galactic Nuclei (AGN)

AGN are galaxies with a super-massive black hole of about $10^6 - 10^9$ solar masses in their center, known as being very bright and variable sources of electromagnetic radiation going observed in radio frequencies up to the gamma-rays in the TeV range. They are considered

among the best candidate sources of both high-energy cosmic rays and neutrinos and since they are the objects being studied in the current work they are discussed in detail in the next chapter.

Galaxy Clusters

Galaxy clusters consists on hundred to thousand gravitationally bound galaxies and are one of the largest structures observed in the univerese. Cosmic rays could be generated in this structures by shock acceleration that results from the structure formation or from some of the powerful AGN that compose it [68, 69, 70].

Chapter 3

Active Galactic Nuclei as Candidate Sources of Variable Neutrino Emission

In this chapter the main characteristics of Active Galactic Nuclei (AGN) are presented together with a brief description of the models predicting emission of high-energy neutrinos. In the last part, the criteria to select candidate AGNs for flaring neutrinos sources is described. These sources are used as test objects for the searches developed in this thesis and described in chapter 7.

3.1 A Brief Introduction to Active Galactic Nuclei

Among all the galaxies in the observed universe, only about 1% are classified as Active Galactic Nuclei. The first object of this category, now named 3C 273, was discovered in 1963 showing extreme radio-emission unlike other stellar objects known at the moment [71]. AGNs in general are now known as being bright sources of electromagnetic emission going from the radio regime to TeV energy range. These sources exhibit different features depending on the wavelength being observed.

A general unification scheme for AGNs was proposed by Urry and Padovani in 1995 [72]. The model propose that the different observed features correspond to the same kind of object being observed from different inclination angles. In this model AGNs are described as galaxies powered by a rotating super-massive black hole of masses in the order of $10^6 - 10^9$ times the solar mass located at its core. A sketch of the AGN morphology is shown in Figure 3.1 Top. The central black hole is surrounded by hot accretion disk that emits electromagnetic radiation from the optical/ultra-violet band to the soft X-ray band. The accreting material is provided by a surrounding dusty torus which is visible in the infrared band. Prominent highly collimated relativistic jets are present for some AGNs which exhibit intense radio emission. The jet axis is parallel to the rotation axis of the super-massive black hole.

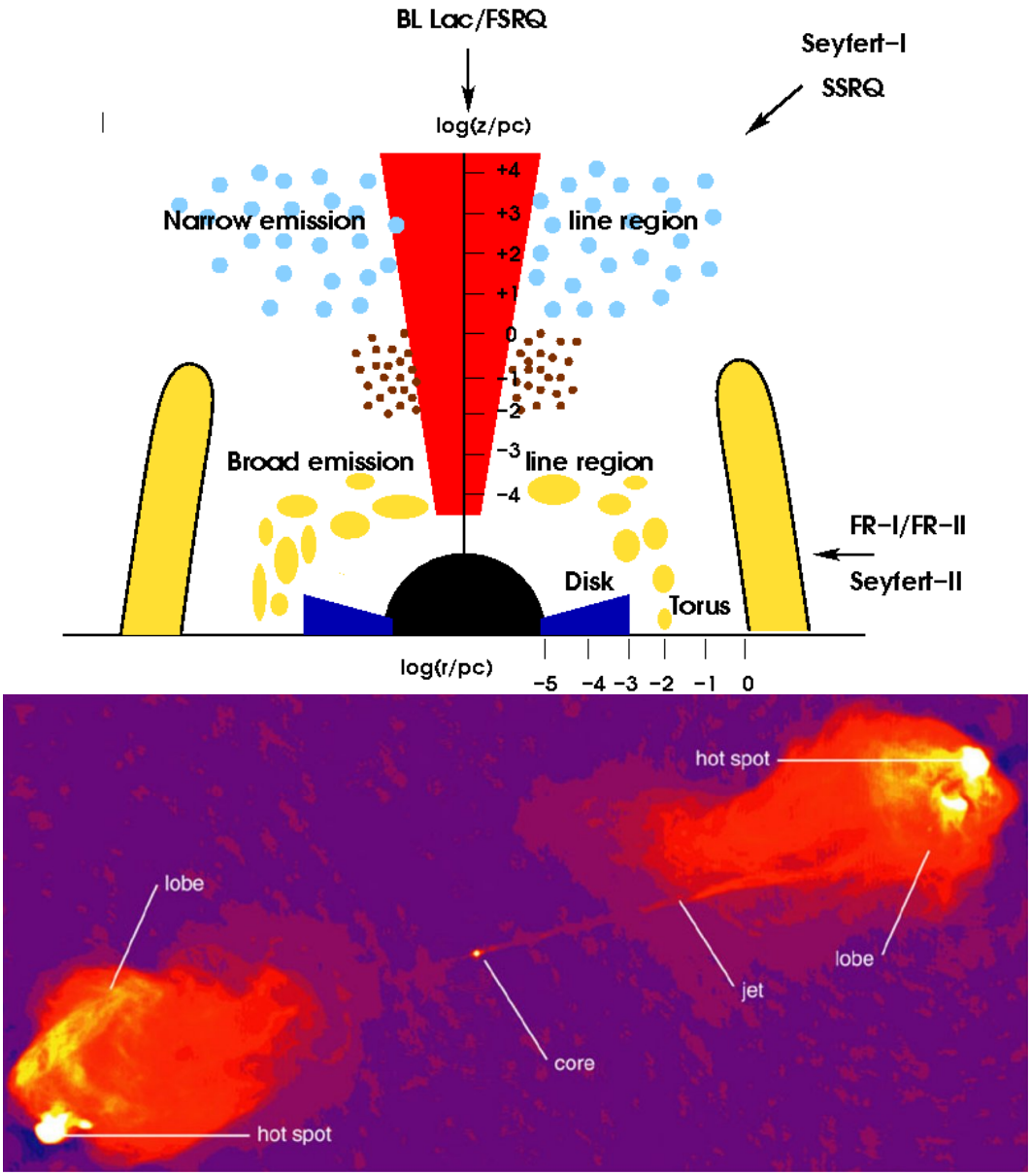

Figure 3.1: Top: Sketch of the Active Galactic Nuclei structure. Blazars are defined as AGNs for which the jet is seen at the Earth from small angles ($\lesssim 10^{\circ}$). Plot taken from [62]. Bottom: Radio Galaxy CygnusA as seen in radio frequencies. Jets are observed as very narrow collimated structures while radio lobes are larger than the host galaxy (shown at the center of the picture) with sizes going from 10 to 10^3 kpc across. Hot spots of radio emission are illustrated in bright yellow [73].

Radio Loudness	**Optical Emission Line Properties**		
	Type 2 (Narrow Line)	**Type 1** (Broad Line)	**Type 0** (Unusual)
Radio-quiet:	Seyfert 2	Seyfert 1 QSO	
Radio-loud:	NLRG { FR I FR II	BLRG SSRQ FSRQ	Blazars { BL Lacs (FSRQ)
	decreasing angle to the line of sight $\longrightarrow$		

Figure 3.2: Simplified classification scheme for AGNs. Taken from [74].

Several gas clouds are formed at different regions of the AGN geometry from which optical lines have been detected. These clouds are named after their optical properties: Broad Line region (BLR) and Narrow line region (NLR). For some AGNs, the jets form hot spots and lobes that have been observed as strong radio emitter structures as shown in Figure 3.1 Bottom. Acceleration of charged particles could take place close to the nuclei, the jets, the hot spots or the lobes of the AGN via diffusive shock acceleration (see section 2.1.2).

Several observational features are taken into account in AGN classification as shown in Figure 3.2. Such features include the host galaxy type, related with the radio intensity, the properties of the optical emission lines and the orientation angle of the AGN jet axis with respect to the observer. If an AGN is being observed at large angles ($\sim 90°$) the dusty torus can obscure the radiation emitted from the BLR and from the accretion disk and hence some of the AGNs would not exhibit this radiation features (FR-I, FR-II, Seyfert-II in Figure 3.1). In this context, Blazars are defined as AGNs that are being observed at small angles ($\lesssim 10°$).

Blazars are further classified as BL-Lac Objects or Flat Spectrum Radio Quasars (FSRQs). This classification is based on the properties of their emission lines and on the radio luminosity at a frequency of 178 MHz (L_{178}). BL-Lacs have absent or weak emission lines (with widths < 5 Å) and $L_{178} < 2.5 \times 10^{26}$ W/Hz while FSRQs have strong and broad emission lines (with width > 5 Å) and $L_{178} > 2.5 \times 10^{26}$ W/Hz [62, 72]. An additional characteristic of Blazars is observed in their spectral energy distribution (SED) which include GeV and TeV gamma-ray observations and is described next.

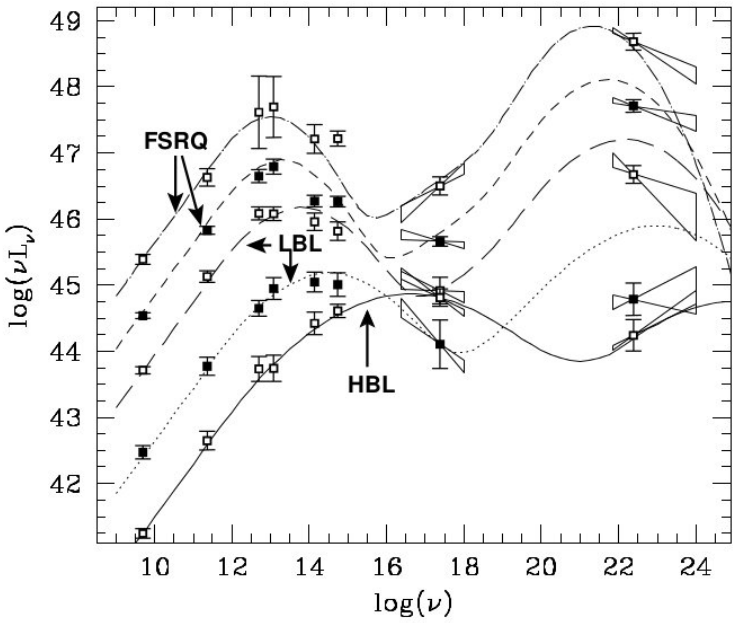

Figure 3.3: Example of characteristic double-bump spectral energy distribution (SED) for Blazars. These objects are further classified taking into account the frequency of the first peak (synchrotron peak) ν_{sy}. Taken from [62].

3.2 The Spectral Energy Distribution

The spectral energy distribution or SED (energy flux per logarithmic energy interval) of Blazars is known to exhibit a characteristic double bump structure as shown in Figure 3.3. Depending on the Blazar under study, the bump at low energies has been observed in frequencies from the radio-UV to X-rays while the second one is observed at high energies from the X-ray band up to TeV gamma-rays[1].

The first bump at low energies is believed to be synchrotron radiation from electrons being accelerated in the AGN jet and is usually referred as the synchrotron peak. Blazars are further classified according to the frequency $\nu = \nu_{sy}$ at which this synchrotron peak is located. The abbreviations found in the literature are LSP (low synchrotron peaked: $\nu_{sy} < 10^{14}$ Hz), ISP (intermediate synchrotron peaked: 10^{14} Hz $< \nu_{sy} < 10^{15}$ Hz) and HSP (high synchrotron peaked:$\nu_{sy} > 10^{15}$Hz)[2]. The luminosity at low energies decreases for larger values of ν_{sy} [72]. In general there are two theoretical models to describe the second bump at high energies referred as leptonic and hadronic models as described next.

[1]In addition, a narrow bump is present for some AGNs in the ultraviolet region ($\sim 10^{15} Hz \approx 10$ eV) attributed to thermal emission from the accretion disk known as the "blue bump" (not shown)[75].

[2]In earlier references this classification only existed for BL-Lacs and in this case the abbreviations used were LBL, IBL and HBL to denote the LSP, ISP and HSP subclasses of BL-Lacs.

3.2.1 Leptonic Models

In leptonic models the second high energy bump is interpreted as the effect of low energy seed photons being up-scattered to the GeV and TeV regime by the accelerated electrons in the relativistic jet in a process known as inverse Compton scattering (ICS):

$$e^- + \gamma_{\text{Low E}} \rightarrow e^- + \gamma_{\text{High E}}. \tag{3.1}$$

The seed photons could be (i) internal photons produced by electron synchrotron radiation i.e the photons responsible of the low energy bump in the SED or (ii) external photons such as the electromagnetic radiation being emitted from the accretion disk, the torus, the NLR or the BLR. In most cases the observed high energy bump for individual AGNs is modeled as the sum of the contributions from different regions providing external seed photons [76, 77].

3.2.2 Hadronic Models

Proton acceleration could occur near to the AGN core due to effects such as magnetic reconnection and direct field acceleration [4] or at the AGN jet via diffusive shock acceleration [5]. In hadronic models the high energy bump of the SED is attributed to direct proton synchrotron radiation, radiation from secondary particles generated in hadronic interactions, or a combination of both. A direct consequence of these models is a high-energy neutrino flux produced in the interactions of the high-energy protons with a photon or matter target field present in the AGN vicinity.

The Proton Blazar Model (PBM) [51], for example, considers proton-photon interactions. The seed photons for these interactions are provided by the low energy synchrotron radiation generated by co-accelerated electrons. The second bump in the SED is then produced by a mixture of gamma-rays from neutral pion decays, proton synchrotron radiation, synchrotron radiation generated by secondary particles (muons, pions and kaons) as well as electromagnetic cascades initiated by the electrons from charged-pions decays [78]. The Proton Blazar Model requires magnetic fields with magnitudes in the order of several tens of Gauss necessary to accelerate protons to $E_p > 10^{19}$ eV. This model favors LBLs over HBLs in terms of high energy neutrino fluxes since LBLs have high luminosity of the low energy component (see Figure 3.3) suggesting higher photon target densities required for efficient photo-pion production.

Other models involving proton-photon interactions, consider the seed photons as being provided by external radiation such as infrared emission from the accretion disk [79, 80] or scattered radiation from the Broad Line Region [81, 82, 83]. These kind of models are more suitable for FSRQs considering their strong emission lines and their characteristic "blue bump" observed in optical-infrared wavelengths. In these models TeV gamma-rays are attenuated by photon-photon interactions with the optical-infrared photons in the environment producing pairs ($\gamma + \gamma \rightarrow e^+e^-$) [80, 83]. The attenuation of TeV gamma-rays is consistent with the fact that only a small fraction of FSRQs have been observed in the

TeV regime [55] and with gamma-ray measurements on the GeV band where a cut-off is observed at a few GeV for most FSRQs and some LBLs [84].

Hard-spectrum BL-Lacs are selected as promising source candidates in Ref. [85] based on a proton-proton interaction model. In this case the target material is provided by the accretion flow falling into the super-massive black hole at the core of the AGNs. This model suggests that the GeV gamma-rays measured from BL-Lacs have a significant contribution from gamma-rays generated from pion-decays. Proton-proton interactions could occur also far away from the core where protons accelerated in the jet collide with ambient gas. However, these models require rather high densities of target material along the jet for efficient pion production which are not expected in AGN jets [86, 5].

3.3 Time Variability in the Electromagnetic Emission of Active Galactic Nuclei

One of the characteristic properties of blazars is their time variability manifested in increments of the photon flux that can reach factors of 10 or more times the observed baseline flux. These flux changes in time are referred as flares. Typical flare durations go from day scales for GeV gamma-rays [21] down to minutes for some sources observed at the TeV domain [20, 19].

In the context the so called one-zone leptonic models, the time variability in the low-energy bump of the SED should be correlated with the variability of the high-energy bump. This is because in this kind of models, the low-energy photons are the target field for the inverse Compton scattering that produces the high energy component. While the optical emission of some AGNs have been observed to be correlated in time with GeV emission [87, 88], there are some cases in which "orphan flares", high-energy photon flares without low-energy counterparts, have been detected [89]. Uncorrelated variability for particular AGNs has been observed between X-rays and GeV gamma-rays [90] and between radio and GeV gamma-rays with time delays of up to 70 days [91]. One example of an orphan-GeV flare is shown in Figure 3.4. The bright gamma-ray flare in this case is observed ~ 150 days ahead of a bright optical flare [89]. A particular interesting case was observed for the AGN 1ES-1959+650 for which an orphan TeV flare was detected [92].

Within a leptonic interpretation, the observation of a flare in a given wavelength with no correlated flares in other wavelengths has inspired models with multiple emission zones which predicts time-lags [89, 93, 94]. However, a persistent trend of time lags or lead patterns over multiple observations at different wavelengths has not been found yet [95, 93]. Hadronic models provide an alternative scenario to describe uncorrelated electromagnetic emission. As described in the last section, the GeV-TeV photon emission in these models is explained as primary or secondary radiation generated by high energy protons. This radiation can vary in time independently of the low energy part of the SED. If the GeV-TeV photon emission is dominated by neutral-pion decays, the time variability observed in this energy

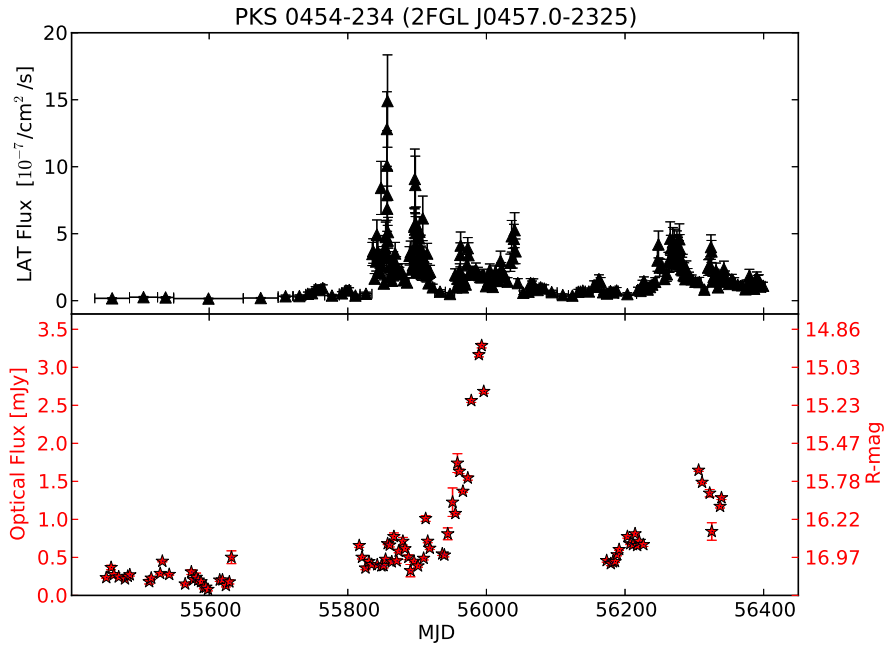

Figure 3.4: Gamma-ray (upper panel) and Optical (bottom panel) light curves for the AGN PKS 0454-234. The timescale of variations in this wavelengths is typically in the order of one to several days. This particular set of light-curves show an example of a bright gamma-ray flare with no (or very small) optical counterpart. Plot taken from [89].

band suggests in a first approximation that the high-energy neutrino flux produced in these models would also exhibit time variability in roughly the same time scales.

On the other hand, neutrino flares may be uncorrelated with GeV-TeV photon flares. In proton-photon models, for example, the observation of GeV-TeV flares implies a low density of low energy photons in the vicinity of the source so these gamma-rays are not absorbed by pair production. This scenario sets an upper limit on the density of the target photon field, during the flare emission, which would be too low for efficient neutrino production [26]. In these models, high energy neutrinos can escape the photon fields while gamma-rays are absorved. The model in Ref. [96] predicts time lags between optical and GeV gamma-ray flares in the order of several days. Since in the case of FSRQs the photon target field for proton-photon interactions is believed to be provided mainly by the optical emission of the accretion disk or the broad line region, the associated neutrino flares may be correlated with the optical flares and not with the gamma-ray flares [82].

The search methods for high-energy neutrino flares developed in the current thesis explore the possible time variability of neutrino emission without assuming time coincidences with photon flares. These methods test a list of candidate AGNs which selection is described next.

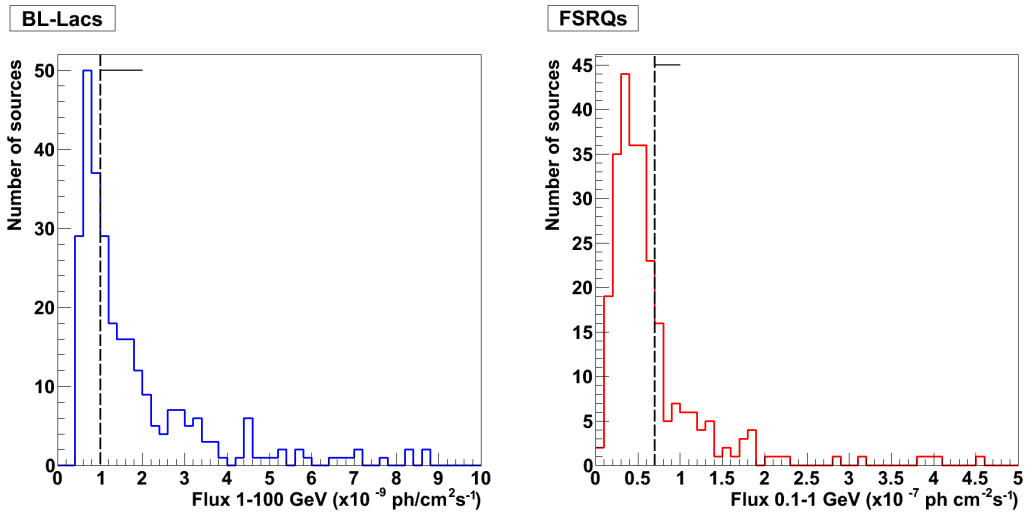

Figure 3.5: Distribution of the photon flux for BL-Lacs and FSRQs in the first Fermi LAT catalog. The vertical lines indicate the thresholds chosen to select bright AGN (flux>threshold) to be tested as neutrino flaring sources.

.

3.4 Selection of Candidate Sources

The selection of candidate neutrino sources is based on general predictions of the hadronic models described in this chapter. using as a starting point the first and second Fermi-LAT catalogs [97]. These catalogs are composed of around 1000 AGNs that have been detected in GeV gamma-rays.

As a first approximation, bright sources in the GeV band could also be bright in neutrinos. Therefore, a threshold on the photon flux is set in the selection of both FSRQs and BL-Lacs. As mentioned in section 3.2.2, the Fermi LAT has measured a cut-off in the energy spectra of most FSRQs located in the ragnge $1-10$ GeV depending on the source, which is consistent with high-energy gamma-rays being attenuated by (i) the low-energy photon fields present in this kind of sources and (ii) the extra-galactic background light [80, 83, 84]. Therefore, the photon flux threshold to select FSRQs is set in the energy range $0.1-1$ GeV since the flux in this energy range dominates the overall luminosity. For the case of BL-Lacs the optical lines are weak or absent and no significant GeV-TeV gamma-ray attenuation is expected. This is consistent with the fact that most of the AGNs observed in the TeV regime are BL-Lacs [55]. Therefore, the energy range for the photon flux used in the selection of these sources is $1-100$ GeV. Figure 3.5 shows the distribution of photon fluxes in the considered energy ranges for BL-Lacs and FSRQs in the first Fermi-LAT catalog. The thresholds to select bright sources is shown in vertical dashed lines.

The promising AGNs for neutrino production listed in Ref. [85] have rather hard spec-

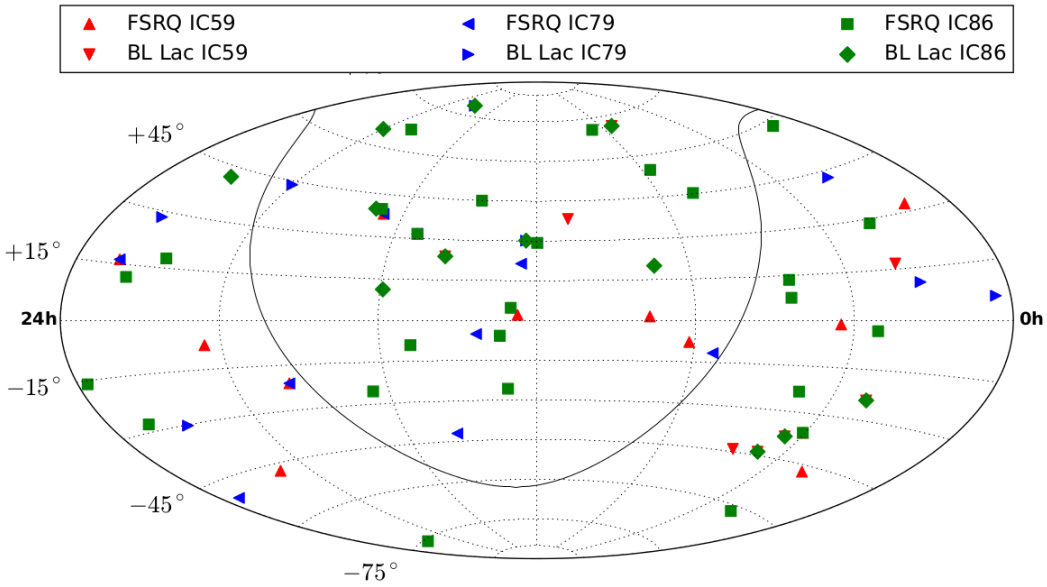

Figure 3.6: Sky map in equatorial coordinates with the positions of the selected AGNs to be tested with three years of IceCube data corresponding to the seasons 2009-2010 (IC59), 2010-2011 (IC79) and 2011-2012 (IC86). The black line represents the galactic plane.

tra[3]. A threshold for the spectral index is therefore set for the AGN selection. In the model in Refs. [81, 82] FSRQs are more promising than BL-Lacs as high energy neutrino sources, since in BL-Lacs the scattered radiation is weaker providing less photon target densities for efficient pion-production via proton-photon interactions. These assumptions hold regardless of the measured photon spectral index in the GeV range and therefore for the selection of promising sources the threshold in the photon spectral index is not set for FRSQs in the Fermi catalog.

The final selection criteria for promising AGN is then defined as:

- **BL-Lacs:** Average flux $[1 - 100$ GeV$] > 8 \times 10^{-8}$ photons cm^{-2}s^{-1} AND spectral index < 2.3
- **FSRQs:** Average flux $[0.1 - 1$ GeV$] > 1 \times 10^{-9}$ photons cm^{-2}s^{-1}

With this selection most of the candidate sources listed in Refs. [83, 51, 80, 85] are included.

In order to select those AGNs with higher changes to be variable in time, a variability index as defined by Fermi-LAT is used as a selection parameter. The variability index is constructed as the test statistic of a likelihood test based on monthly light curves. The null hypothesis in this test correspond to the source being steady. A source is classified as being variable at the 99% level if the variability index is equal or greater than 41.6 [97].

[3]The spectral index for a power law energy spectra is less than $\gamma \approx 2$ for the promising sources in Ref. [85]

On top of the selection described above, only AGNs that exhibit electromagnetic flares at different wavelengths were selected. For each one of these AGN a time T_m that indicates a flaring episode is taken either from the Astronomer Telegrams page [98] or from other references for particular AGN. As will be discussed in chapter 7 the time T_m sets the center of a search time window with duration of 80 days in which several neutrino flares are looked for. The search method itself however does not assume time coincidences beween neutrino and photon flares, so the search time windows serves only as a first guess in which neutrino flares can be found.

The selection of promising AGNs described in this section was performed for three different seasons each one covering a year of data of in the IceCube experiment: 2009-2010 (IC59), 2010-2011 (IC79), and 2011-2012 (IC79). For each year of data sources exhibiting photon flares were selected. The lists of the selected AGN are shown in chapter 8 together with the results of applying the search-methods described in chapter 7. Figure 3.6 shows the distribution in equatorial coordinates of the positions of the selected sources.

Chapter 4

High-Energy Neutrino Astronomy

The previous chapters provided an overview on the production mechanisms of astrophysical neutrinos mediated by cosmic ray interactions. Several astrophysical objects were introduced as neutrino source candidates emphasizing in Active Galactic Nuclei and their phenomenology. In order to detect high energy neutrinos, large detector volumes are needed to overcome the fact that the neutrino interaction probabilities are small. In this chapter the main aspects of high energy neutrino propagation and detection are presented. Emphasis is made on ν_μ interactions since these are the events that provide better angular resolution and are considered in the point search methods described in chapter 7.

4.1 Neutrino Propagation: Oscillations in Vacuum

As briefly discussed at the end of section 2.2, the astrophysical neutrino flux resulting from the decays of pions, muons and kaons could have different contributions to the final neutrino flavor composition at the source depending for example on the energy range at which these decays dominate. Once astrophysical neutrinos are produced in these processes they travel path lengths in the order of $1\text{Gpc} \sim 3 \times 10^{25}$ m for extra-galactic sources [52].

It is well known that neutrinos change flavor during their propagation in path lengths up to 10^{10} m, in the case of solar neutrinos, in a phenomenon known as neutrino oscillations. This effect has been observed experimentally in neutrino fluxes from different sources such as solar neutrinos, accelerator neutrinos and atmospheric neutrinos [99, 100, 101]. In principle neutrino oscillations can also be observed for astrophysical neutrinos giving the opportunity of testing the effect for larger path lengths [53]. In the following the derivation of neutrino oscillation probabilities is briefly described following Ref. [99].

Neutrino oscillations arise from the fact that they have non-zero masses. Neutrino flavor eigenstates described in the basis of mass eigenstates are given by:

$$\left| \nu_\alpha \right\rangle = \sum_{j=1}^{3} U^*_{\alpha j} \left| \nu_j \right\rangle, \tag{4.1}$$

where $\alpha = e, \mu, \tau$ describe the different neutrino flavor eigenstates and $j = 1, 2, 3$ describe the different mass eigenstates. $U_{\alpha j}$ are the elements of the 3×3 Maki-Nakagawa-Sakati matrix (MNS) which relates the mass and flavor eigenstates. The probability for a neutrino produced with initial flavor α to be detected in the flavor β is given by:

$$P(\nu_\alpha \to \nu\beta) = |\langle\, \nu_\beta \,|\, \nu_\alpha \,\rangle|^2. \tag{4.2}$$

where:

$$|\, \nu_\beta \,\rangle = \sum_{k=1}^{3} U^*_{\beta k} |\, \nu_k \,\rangle. \tag{4.3}$$

Applying Schrodinger equation and using the approximation that the mass eigenstates evolve in time as plane waves in vacuum:

$$|\, \nu_{j,k}(t) \,\rangle = e^{-i(E_{j,k})t} |\, \nu_{j,k}(t=0) \,\rangle, \tag{4.4}$$

where $E_{j,k}$ are the energies of the mass eigenstates j, k. Replacing 4.4 in 4.1 and 4.3 the transition probability 4.2 for a given time t becomes:

$$P(\nu_\alpha \to \nu_\beta) = |\langle\, \nu_\beta(t) \,|\, \nu_\alpha(t=0) \,\rangle|^2 \tag{4.5}$$

$$= \sum_{k,j} U^*_{\alpha k} U_{\beta k} U_{\alpha j} U^*_{\beta j} \exp\left(-i \frac{\delta m^2_{jk} L}{2E}\right), \tag{4.6}$$

written in natural units ($c = \hbar = 1$). $L = t$ is the distance between the production and detection points and $m^2_{jk} = m^2_j - m^2_k$ is the difference of the squared mass of the mass eigenstates j and k. The transition probability 4.6 has an oscillatory behavior with amplitudes proportional to the elements of the MNS matrix and oscillation phases given by

$$\Delta_{jk} = \frac{\delta m^2_{jk} L}{4E} \approx 1.27 \left(\frac{\delta m^2_{jk}}{\text{eV}}\right) \left(\frac{L}{\text{km}}\right) \left(\frac{E}{\text{GeV}}\right)^{-1}. \tag{4.7}$$

Since the path lengths L traveled by astrophysical neutrinos is in the order of 10^{22} km even for very high energy neutrinos ($E \approx 10^{15}$ eV) the oscillation phase is large ($\Delta_{ij} >> 1$). Taking into account the uncertainties in the estimation of distance to the production site L, and the uncertainties in the energy measurement (see chapter 5) the transition probability $P(\nu_\alpha \to \nu_\beta)$ is averaged out over many oscillations giving:

$$P(\nu_\alpha \to \nu_\beta) = \sum_{j=1}^{3} |U_{\alpha j}|^2 |U_{\beta j}|^2. \tag{4.8}$$

Using the experimental values for the parameters involved in the calculation of the MSN matrix elements ($U_{\alpha j}, U_{\beta j}$) it can be shown that a initial flavor ratio for the benchmark production scenario $\nu_e : \nu_\mu : \nu_\tau = 1 : 2 : 0$ (see section 2.2) is then detected at Earth

as $\nu_e : \nu_\mu : \nu_\tau = 1 : 1 : 1$ [102, 103]. Alternative scenarios give different flavor ratio predictions and therefore measuring the flavor ratios at Earth can provide insight on the production mechanisms (see Refs. [102, 104] for a review on neutrino flavor calculations for astrophysical neutrinos and [100] for a review on neutrino theory).

Resent constraints on the flavor ratio for astrophysical neutrinos have been provided by the IceCube collaboration. The scenarios briefly described in section 2.2, that predict flavor ratios $1 : 2 : 0$ and $0 : 1 : 0$ at the source, are well compatible with the data while an scenario in which neutron decays dominate the neutrino flux (see Eq. 2.11) giving an initial flavor ratio $1 : 0 : 0$ is disfavored with a significance of 3σ [54].

4.2 Neutrino Detection

Astrophysical neutrinos are detected at Earth via the secondary particles they generate in weak force interactions with matter. At the energies discussed here (∼TeV-EeV) neutrinos resolve the individual constituent quarks of the target nuclei N in a process known as deep inelastic scattering (DIS). Depending on the mediator of the weak interactions ($W^\pm$ or Z^0) the DIS processes taken place are:

$$\nu_l(\bar{\nu}_l) + N \xrightarrow{W^\pm} l^-(l^+) + X \qquad \text{Charged Current (CC)} \qquad (4.9)$$

$$\nu_l(\bar{\nu}_l) + N \xrightarrow{Z^0} \nu_l(\bar{\nu}_l) + X \qquad \text{Neutral Current (NC)} \qquad (4.10)$$

where X denotes the remnant of the target nuclei N. This remnant interacts with the surrounding medium generating a cascade of charged particles also referred as an hadronic shower. The cross section for neutrino-nucleon interactions increase with the neutrino energy as shown in Figure 4.1. For high energies ($E_\nu > 10^{15}$ eV) the cross sections for neutrino and anti-neutrino nucleon scattering are nearly identical and therefore anti-neutrino+Nucleon cross sections are not shown in the plot.

In general neutrino interactions with the electrons of the target material can be neglected with respect to neutrino-nucleon interactions since their cross sections are around two order of magnitude smaller. However one special case arise for the $\bar{\nu}_e$-electron scattering in which a resonance forms at around 6 PeV also known as the Glashow resonance [105].

4.2.1 Absorption of Neutrinos in the Earth

The main consequence of the rise of the cross section with the neutrino energy is the absorption of high energy neutrinos in the PeV-EeV range transversing the Earth. Absorption effects are usually described in terms of the interaction length defined as the average distance traveled by the incoming neutrinos inside a material before interacting. The interaction length is given by:

$$L_{int}(E_\nu) = \frac{1}{N_A \sigma_{\nu N}(E_\nu)}, \qquad (4.11)$$

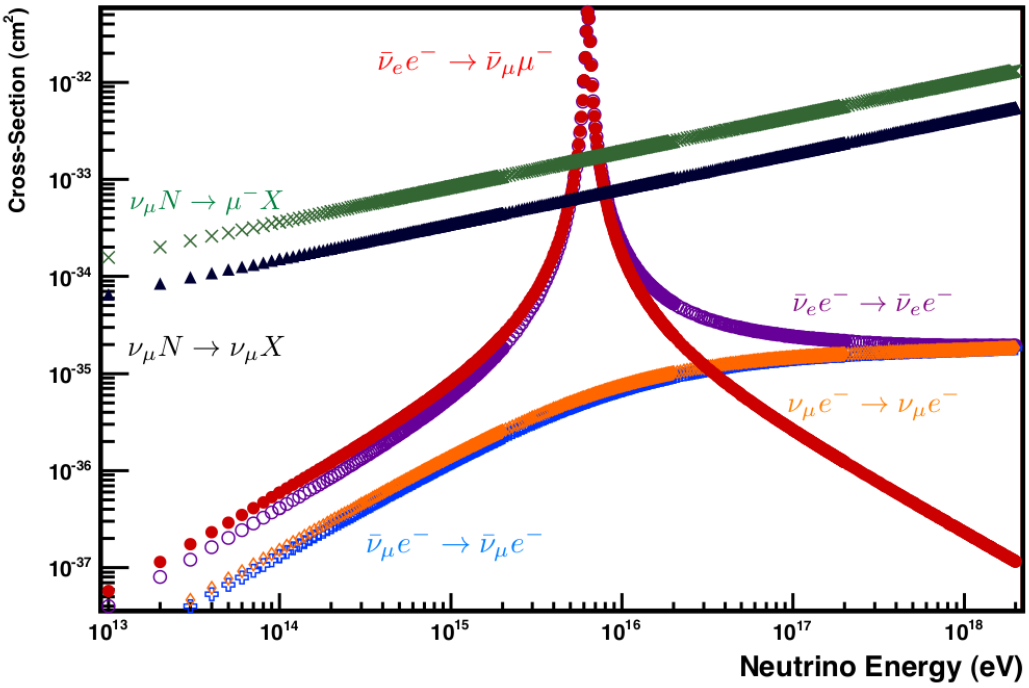

Figure 4.1: Cross sections for neutrino-nucleon and neutrino-electron scattering as function of the neutrino energy. Plot taken from [106].

where $N_A = 6.02 \times 10^{19}\text{cm}^{-3}$ is the water-equivalent Avogadro's number and $\sigma_{\nu N}(E_\nu)$ is the neutrino-nucleon cross section as function of the neutrino energy.

Figure 4.2 shows the interaction lengths as function of the neutrino energy E_ν together with the water-equivalent Earth diameter. The interaction length at high energies is smaller than the Earth diameter limiting the detection of high energy neutrinos traveling through the Earth with energies above ~ 100 TeV. Neutrinos with smaller energies transversing the Earth can still interact in the vicinity of the sensitive volume of the detector.

The distance a particle have to travel in certain material before interacting at the detector are also referred as column depths. High energy neutrinos in the PeV-EeV range can be detected if they arrive from directions with column depths smaller than the interaction length. The detection probability of high energy neutrinos not only depends on the neutrino interaction length L_{int} but also on the range of the neutrino-induced muons which is described next.

4.2.2 Muon Propagation in Ice

During propagation, muons lose energy by ionization and radiative losses such as bremsstrahlung, pair production and photo-nuclear interactions. The mean energy loss per unit of

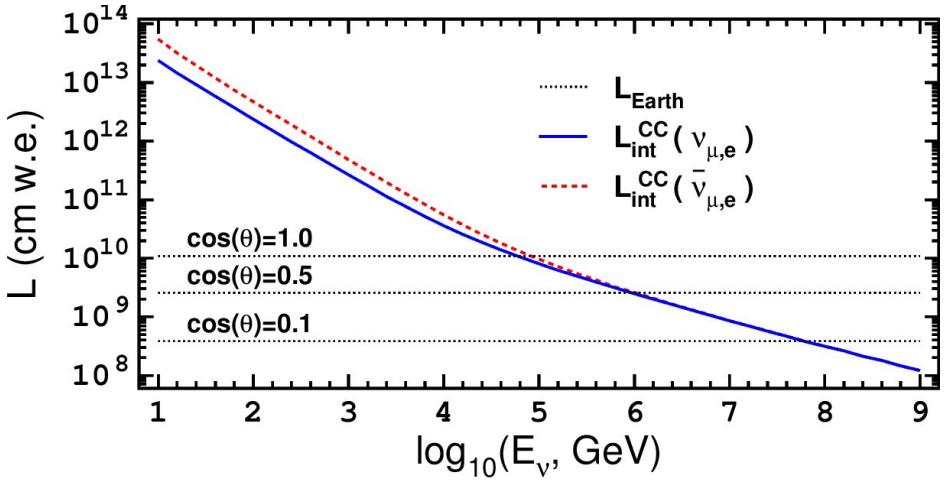

Figure 4.2: Water-equivalent (w.e) interaction length as function of the neutrino energy. The horizontal dashed lines are the Earth column depth expressed in terms of the nadir angle: $\cos(\theta) = 1.0 \rightarrow 10^{10}$ cm (w.e) which correspond to the Earth diameter. Plot taken from [107].

distance is approximated as [108]:

$$\left\langle -\frac{dE_\mu}{dx} \right\rangle = a + bE_\mu \tag{4.12}$$

where $a = 0.24$ GeVm^{-1} and $b = 0.00032$ m^{-1} for ice [109]. The first constant term accounts for ionization losses while the other losses such as stochastic bremsstrahlung losses increase linearly with energy. The critical energy at which the radiative losses equal ionization losses is defined as $E_{\text{crit}} = a/b \approx 750$ GeV. Above this critical energy radiative losses dominate. Muons with energies below E_{crit} are regarded also as minimally ionizing muons.

The photons generated in stochastic bremsstrahlung losses generate electromagnetic cascades in the interaction medium. The muon and the charged particles produced in electro-magnetic cascades induce Cherenkov light as described in the next section.

The mean energy loss is used to calculate the muon range as:

$$R_\mu = \int_{E_0}^{E_\mu} \left\langle -\frac{dE'}{dx} \right\rangle^{-1} dE' \approx \frac{1}{b} \ln\left(1 + \frac{E_\mu}{E_{\text{crit}}}\right). \tag{4.13}$$

For example a muon with energy $E_\mu \approx 1$ TeV has a range of $R_\mu \approx 2$ km while for $E_\mu \approx 1$ PeV the range becomes $R_\mu \approx 20$ km. Since a muon can travel large distances depending on its energy, in the case of neutrino-induce muons the interaction vertex could be located outside the instrumented volume of the neutrino telescope. In this case, the muon loses energy before entering the detector and therefore the deposited energy inside the sensitive

volume is smaller than the total energy. A better estimation of the total energy can be achieved by looking for events contained in the sensitive volume. The methods to estimate the muon energy are discussed in chapter 5.

4.2.3 Cherenkov Radiation

A charged particle traveling in a dielectric medium with a velocity v polarize its constituent molecules. Water molecules, in the case of ice, are exited by the electric field of the moving charged particles returning to their ground state by emitting light. If the charged particles travel faster than the phase velocity of light in the medium i.e:

$$\beta = \frac{v}{c} \geq \frac{1}{n(\lambda)}, \tag{4.14}$$

where $n(\lambda)$ is the refraction index of the medium for the wavelength λ, then the emitted light of the molecules in the path of the charged particle interfere constructively forming a coherent wavefront of light in a cone shape. The angle between the direction of the incoming charged particle and the cone wavefront it generates is given by:

$$cos(\theta_c) = \frac{1}{\beta n(\lambda)}. \tag{4.15}$$

In the case of ice as propagation medium and relativistic particles ($\beta \approx 1$), θ_c takes values in the range $40.5 - 42.5^\circ$ depending on the light wavelength. The number of photons emitted per unit of length and wavelength is given by the Frank-Tamm formula:

$$\frac{dN}{dxd\lambda} = \frac{2\pi\alpha}{\lambda^2}\sin^2(\theta_c). \tag{4.16}$$

Integrating over wavelengths from 300 to 600 nm, at which the photo-multipliers detect light in the IceCube Neutrino Observatory, the number of emitted photons per unit of length is $N \approx 200$ photons/cm.

4.2.4 Neutrino Telescope Principle

The energy and direction estimators of individual events detected in a neutrino telescope are based on the propagation and detection of the Cherenkov light that the charged leptons induce in the interaction medium. This estimators are described in chapter 5 as implemented in the case of the IceCube Neutrino Telescope.

The astrophysical neutrino searches described in chapters 6 and 7 focus on the events product of charged current interactions of muon neutrinos i.e $\nu_\mu(\bar{\nu}_\mu) + N \xrightarrow{W^\pm} \mu^-(\mu^+)$. As discussed later in this chapter, muon trajectories follow straight paths with lengths in the order of tens of km for incoming neutrino energies in the TeV-EeV range. The kinematic

angle between the incoming muon neutrino and the produced muon is parametrized as [110]:

$$\Psi \approx 0.7^{\circ} \left(\frac{E_{\nu}}{\text{TeV}} \right)^{0.7} \tag{4.17}$$

where E_{ν} is the neutrino energy. At 1 TeV the kinematic angle is $\Psi \approx 0.7^{\circ}$ which is smaller than the detector angular resolution of reconstructed muon events in the order of 1° at this energy (see chapter 5 for event reconstruction details). The reconstructed trajectory of the secondary muon therefore points approximately in the same direction than the incoming neutrino. This makes neutrino-induced muon tracks appropriate events for neutrino astronomy and point source searches since they point back approximately to their direction of origin.

Possible deflections in the muon trajectory due to the Earth magnetic field and Coulomb scattering at energies above 1 PeV are too small to be resolved within the detector reconstruction capabilities. The muon charge cannot be estimated on the basis of curved trajectories in absence of an stronger magnetic field. Since the charge of the secondary muons is related with the nature of the incoming particles (Eq. 4.9) neutrinos and anti-neutrinos cannot be distinguished in a high neutrino telescope as in the case of IceCube.

Since the cross sections of neutrino interactions are small even at high energies[1] large volumes of interaction material are needed in order to increase the interaction probability. The interaction medium in the case of the IceCube Neutrino telescope is the Antarctic ice at the south pole (see chapter 5 for more details on the IceCube detector). With 1 km^3 of instrumented volume, and depending on the production model at the source, early estimations of astrophysical energy neutrino event rates in this kind of telescopes predicted in the order of a few (~ 10) astrophysical neutrino signal events per year (see for example Refs. [111, 112]). The searches of these events are performed in the presence of background events as described next.

4.3 Background for the Detection of Astrophysical Neutrinos

As briefly described in section 2.2, the very same $p + N$ interactions that are believed to take place in the environment of the sources of cosmic rays and produce astrophysical neutrinos take place also at Earth when cosmic ray particles collide with nuclei of the atmosphere. The subsequent cascade of particles or shower generated in these interactions can be made of up to several thousand particles depending on the incoming cosmic ray energy [113] (see Figure 4.3 for an illustration of an atmospheric shower). The two main background components for the search of astrophysical neutrinos are atmospheric muons and atmospheric neutrinos produced in these showers.

[1] in the order of 10^{-32} cm^{-2} for 1 PeV neutrino energy

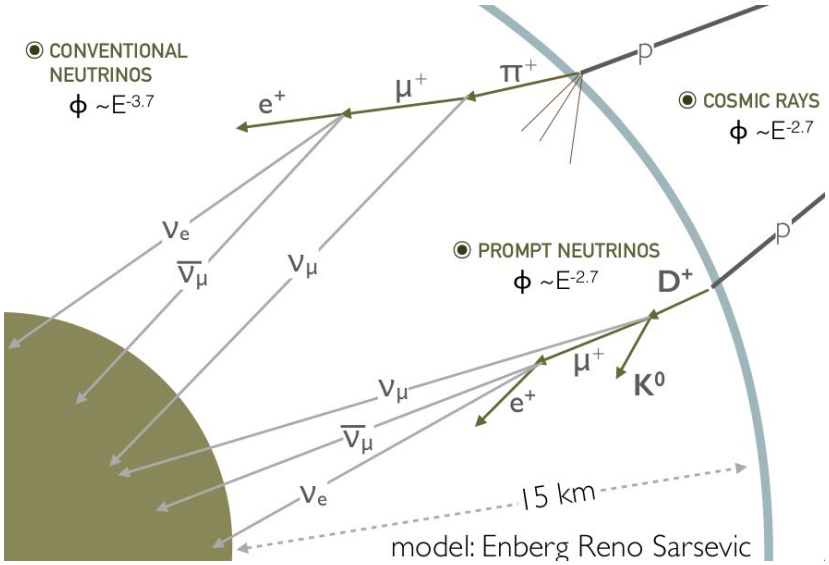

Figure 4.3: Sketch of the atmospheric neutrino and muon flux produced by cosmic ray interactions in the Earth atmosphere.

4.3.1 Atmospheric Muons

Atmospheric muons are produced mainly in pion and kaon decays (see Eqs. 2.7, 2.8 and 2.12). In the atmosphere pions and kaons lose energy in interactions with the target nuclei before they decay. The atmospheric muon energy spectrum is then softer than the energy spectrum of the primary cosmic ray particles producing them which follows a power law $E^{-2.7}$ (see section 2.1). The resulting muon energy spectrum follows approximately a power law $E^{-3.7}$ at high energies ($\gtrsim 100$ GeV) [113].

For the IceCube neutrino telescope, located at the south pole, atmospheric muons produced in the northern hemisphere are absorbed by the Earth. This is because their range R_μ (see Eq 4.13) is in the order of several tens of km for the energies considered here which is smaller than the Earth diameter of ~ 6000 km.

Atmospheric muons produced in the southern hemisphere, also refereed as down-going atmospheric muon events, are the main background for astrophysical neutrino searches in this region of the sky for which the number of atmospheric muon events is expected to be six orders of magnitude larger than the astrophysical neutrino flux. If only reconstructed tracks transversing the sensitive volume of the detector are taken into account, muon-tracks produced by atmospheric muons and those produced in high energy neutrino interactions cannot be distinguished. As described in chapter 5, additional techniques such as the use of a surface detector to veto events likely to be produced in atmospheric showers or select events for which their interaction vertex is reconstructed inside the sensitive volume, are used to distinguish tracks induced by atmospheric muons or neutrinos from events induced by astrophysical neutrinos.

In addition, several hundreds of low energy muons produced in a single shower, also known as muon bundles, can mimic an energetic muon track produced by a high energy neutrino and additional techniques are needed in order to reduce this source of background. Searches of astrophysical neutrinos in the northern hemisphere are also affected by the down-going atmospheric muon flux: Two down-going atmospheric muons arriving close in time (coincident events) can resemble the Cherenkov light signature of a single up-going event i.e a neutrino-induced muon track arriving from the northern hemisphere.

There are several ways to decrease the muon background in neutrino telescopes which are described in more detail in chapter 5. On one hand the energy spectrum of astrophysical neutrinos is expected to follow a power law E^{-2} (see section 2.2). Since this is a harder energy spectrum than the spectrum of atmospheric muons, energy cuts are used to get rid of low energy atmospheric muons since at energies in the PeV-EeV range the astrophysical neutrinos would start to dominate. On the other hand, as discussed in section 4.2.2, at high energies radiative losses dominate the muon energy losses and this can be used to distinguish high energy muon tracks from low energy muon bundles as their energy loss profile is different. Additionally, dedicated direction reconstructions can that take into account the event topology provide an additional tool to decrease the number of coincident down-going muon events that mimic and up-going event.

Finally, the atmospheric muon rates depend on weather conditions. Changes in the temperature of the atmosphere are accompanied by changes in the density of air molecules and since the pions and kaons that are produced in air showers are more likely to interact before decaying in a dense and cold atmosphere, this effect translates in changes in the muon rate in the order of $\pm 10\%$ [22, 114].

4.3.2 Atmospheric Neutrinos

The atmospheric neutrino flux is produced in the same decays that generate the atmospheric muon flux i.e mainly in decays of pions and kaons product of comic ray interactions in the atmosphere. Their energy spectrum follows also a power law $E^{-3.7}$ as described in the previous section. The atmospheric neutrino flux has been measured by several experiments and is shown Figure 4.4. Since atmospheric neutrinos can transverse the Earth an interact close to the detector depending on their initial energy they are the main source of background for astrophysical neutrino searches in the northern hemisphere.

The atmospheric neutrino flux product of pion and kaon decays is also referred as the conventional atmospheric neutrino flux. An additional neutrino flux is produced in the decay of heavier mesons such as D-mesons and Λ_c^+ (see Eqs. 2.13 and 2.14). Since this heavier mesons have smaller lifetimes they almost always decay before further interactions with the atmosphere nuclei. Therefore their energy spectrum follows the spectrum of the parent cosmic rays i.e $E^{-2.7}$ and it is referred as prompt atmospheric neutrinos (see Figure 4.3) [116].

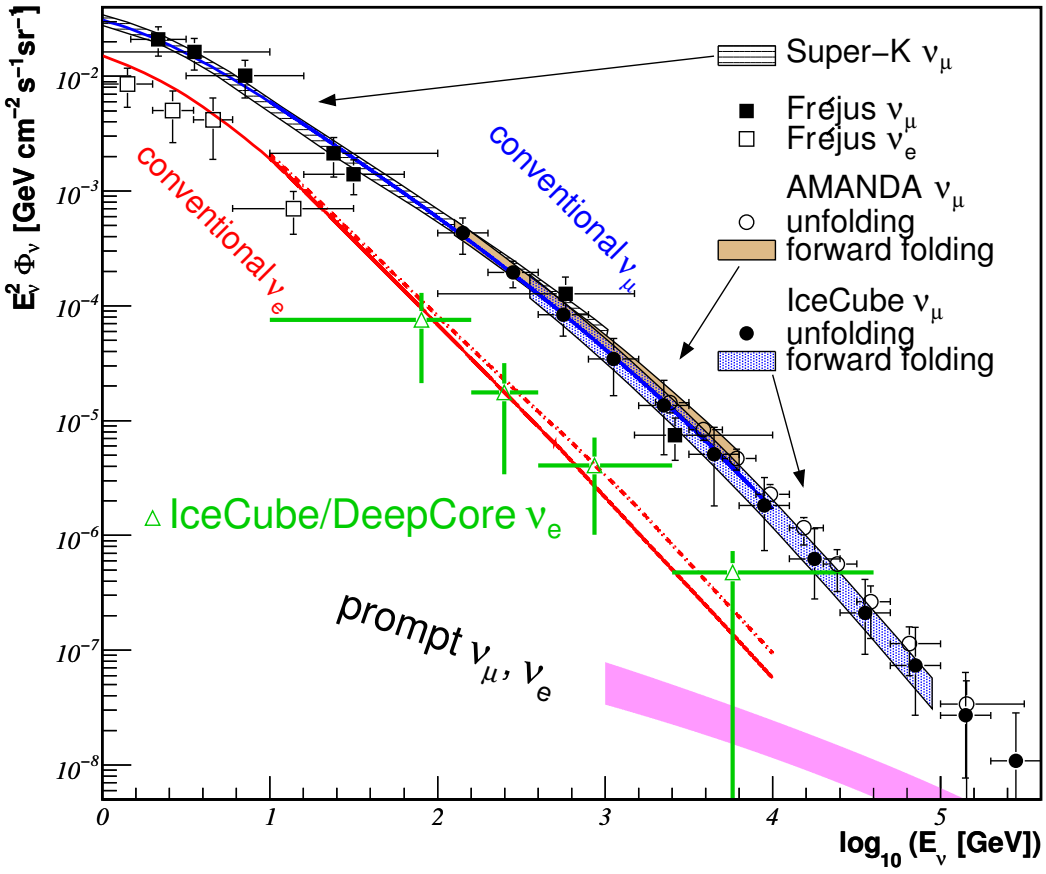

Figure 4.4: Conventional electron-neutrino and muon-neutrino atmospheric flux measured by several experiments as function of the neutrino energy. Taken from [115].

4.4 Search Concept for Point Sources of Astrophysical Neutrinos

There are several ways to test the hypothesis of having a population of high energy neutrino events generated outside the Earth atmosphere. These searches differ on the assumptions made on the signal properties such as the position on the sky of potential neutrino sources (AGNs, GRBs, binary systems, etc), the spatial extension of the source compared with the experimental angular resolution (point source or extended source), and the contribution of several sources being added up (stacking and diffuse analyses) as described next.

In a stacking analysis, several astrophysical objects, such as AGNs, are thought to be too weak for individual detection. In order to increase the detection probability in this kind of search, a set of objects with known positions is considered in a single the statistical test. On the other hand, A diffuse search tests the hypothesis of having a flux of high energy neutrinos above the atmospheric neutrino and muon background. This test does

not require a spatial clustering of the vents and if the observation is significant, as in the case of the astrophysical neutrino flux already detected [17], it can be intrepeted as the overall contribution of several unresolvable high energy neutrino sources. In this kind of analysis the relevant information taken into account is the energy distribution of the events and not their spatial distribution.

In a point source search the signal is defined as a statistically significant population of neutrino-induced muon tracks clustering in particular direction in the sky. There are additional parameters that help to distinguish a signal from the background:

1. Energy distribution: In the second order Fermi acceleration case, the energy distribution of astrophysical neutrinos should follow a power law E^{-2}, whereas the energy distribution of atmospheric neutrinos at high energies ($\gtrsim 1$ TeV) follows $E^{-3.7}$ [117].

2. Time distribution: As mentioned earlier changes in the atmospheric neutrino and muon flux are less than $\pm 10\%$ due to seasonal variations. Since the time variability at the sources is expected to produce larger changes in the neutrino flux (see section 3.3), event timing information can be used as a discrimination parameter.

   Including time information in the analysis is the core of the methods developed in this thesis and described in chapter 7.

Different analysis methods differ in the way the parameters described above (space, energy, time) are taken into account. The binned method for example is one of the methods implemented in previous IceCube analyses in order to calculate the significance of a clustering of events in space [118, 24]. This approach used only the direction reconstruction of the events to calculate the significance of an excess of events over the expected number of background events contained in a predefined circular bin in the sky.

Previous works demostrated than the detection probability increases by including additional information into the analysis, such as the reconstruction error and the energy estimators for each event [24, 119]. This additional parameters are included in a unbinned likelihood method as described in chapters 6 and 7

Chapter 5

Reconstruction and Selection of Events in the IceCube Detector

In this chapter the main technical aspects of the experimental set-up for the detection of astrophysical neutrinos is described. This chapter begins with a description of the IceCube neutrino telescope and its main components. Next the event direction and energy reconstructions strategies are presented. Finally the strategies for event selection are described.

5.1 The IceCube Neutrino Observatory

The IceCube Neutrino Observatory is composed of three sub-detectors located at the geographic south pole: the IceTop array, the IceCube array and the DeepCore array as shown in Figure 5.1.

The IceTop array consists of 324 light sensors distributed in 81 stations arranged in an hexagonal array. Each station consists of two tanks filled with bubble-free ice and each tank contains two sensors. This surface array was designed to detect air showers of secondary particles produced by cosmic rays in the range 300 TeV to 2 PeV interacting with nuclei in the atmosphere [120, 121].

The IceCube array consists of 5160 light sensors buried in the Antarctic ice at depths between $1450\,\mathrm{m}$ and $2450\,\mathrm{m}$ [12]. These sensors are distributed among 86 strings also arranged in an hexagonal geometry. The distance between strings is 125 m and the distance between the light sensors in each string is 17 m. While construction data was taken for partially completed string configurations. The season from May 20-2009 to May 31-2010 is referred as IC59, the season from May 31-2010 to May 12-2011 is referred as IC79 and the season from May 12-2011 to May 15-2012 correspond to data taken with the completed detector referred as IC86-I. The reconstruction of the direction and energy of events in the IceCube array relies on the detection of Cherenkov radiation (described in section 4.2.3) at the light sensors and is presented in section 5.2. Finally the Deep Core array consists of 480 DOMs distributed over 8 strings. The smallest spacing between DOMs is 7 m and

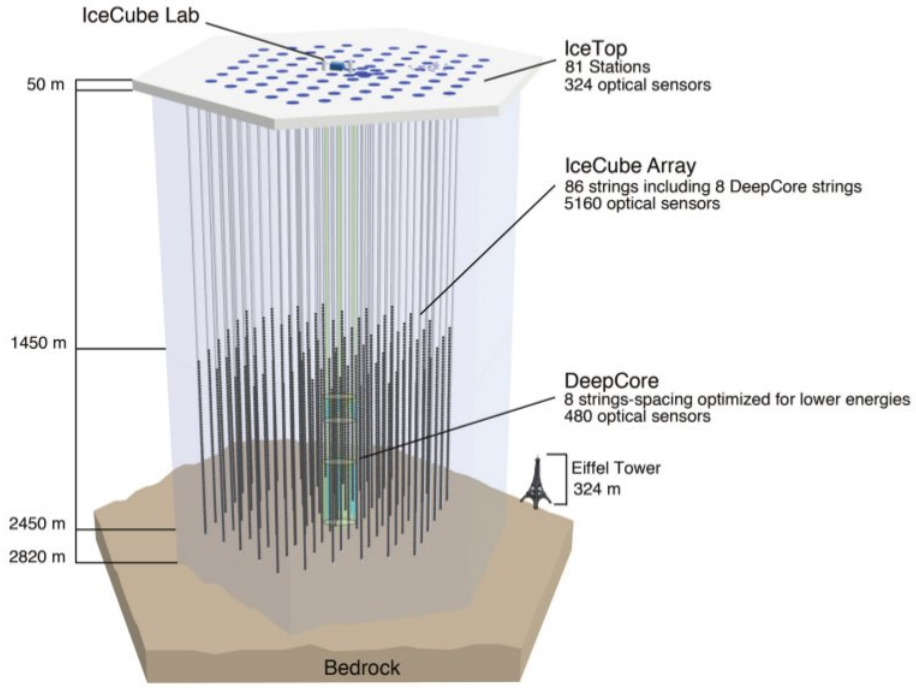

Figure 5.1: The IceCube Neutrino Observatory: The IceTop array is located at the surface while the IceCube and DeepCore arrays are buried in the Antarctic ice.

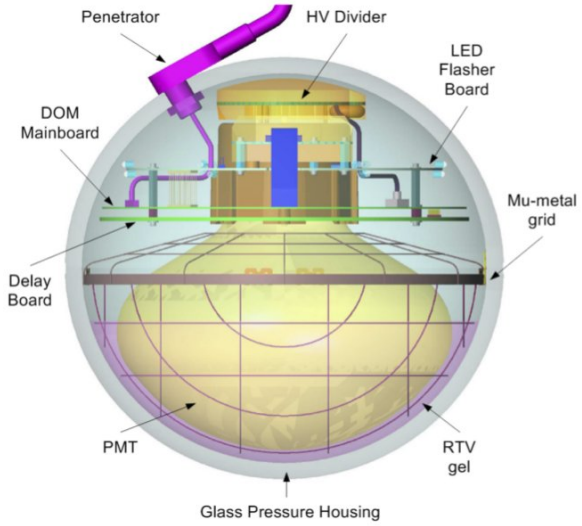

Figure 5.2: Components of the the digital optical module (DOM)

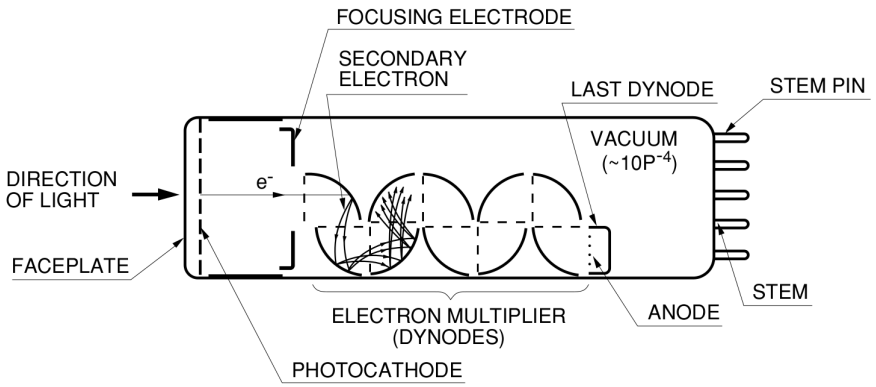

Figure 5.3: Sketch of a photo-multiplier tube (PMT). Taken from [122]

the smallest spacing between strings is 70 m. The DeepCore array have smaller spacing between light sensors than the IceCube array both in string to string distance and distance between light sensors in a single string. The denser instrumentation in the DeepCore array allows to detect light produced in low energy events becoming sensitive to neutrinos of energies down to around 10 GeV [123].

5.1.1 The Digital Optical Module

The fundamental component of the IceCube array is the Digital Optical Module (DOM) shown schematically in Figure 5.2. Each DOM contains a 25 cm diameter Hamamatsu R7081-02 photo-multiplier (PMT) sensitive to light in the wavelength range of 300 nm to 650 nm [124, 125].

An sketch of a PMT is shown in Figure 5.3. When an incident photon hits the photo-cathode an electron is produced via the photo-electric effect. The generated electron, also referred as photo-electron, is then accelerated by a focusing electrode towards a dynode where secondary electrons are produced. A series of 10 dynodes, for the case of the R7081-02 PMT, multiply the number of electrons via secondary electron emissions in each one of them. In this process a single incident photon leads to the generation of around 10^7 electrons that are finally collected in the PMT anode [122]. The PMT is enclosed in a 33 cm diameter glass housing resistant to the ice pressure of around 400 atm and it is surrounded by a metal grid that provides a shield for the earth magnetic field which improves the electron collection performance [126].

Each DOM includes a 2 kV high voltage power supply and a main board with the necessary electronics to readout and digitize the PMT signal. The analog signal output is a time-dependent voltage measured between the anode and the cathode, which is proportional to the collected charge, and is referred as a *waveform*. The analog signal is digitized if it crosses an integrated charge threshold corresponding to 0.25 times the charge generated by a *single photo-electron* (SPE). The digitization consists on the generation of series of data

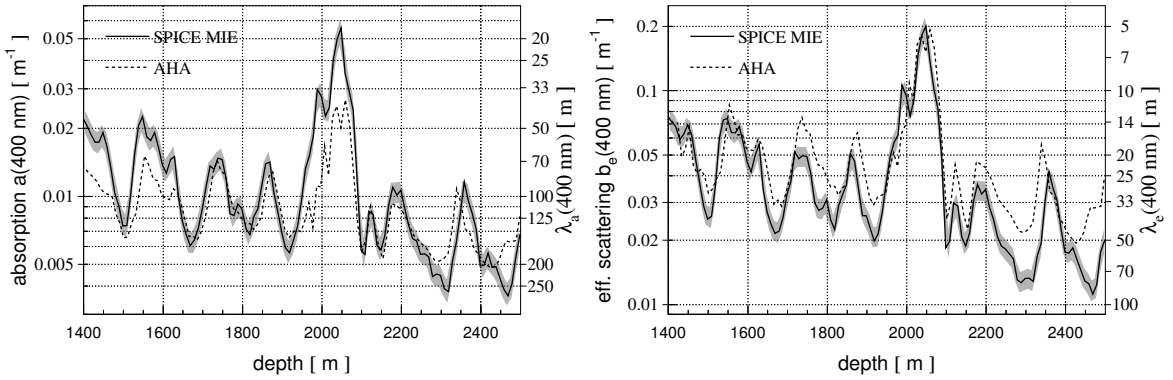

Figure 5.4: Absorption (right) and scattering (left) coefficients in the antartic ice for a wavelength of 400 nm as function of the ice depth. Two studies were developed to model the properties of the light propagation in the ice: The AHA model is described in Ref. [109] and the Spice-MIE model is described in Ref. [127]. Plot taken from [127].

blocks with a time-stamp and a voltage measurement obtained by the use of two Analog Transient Waveform Digitizers (ATWD) and a Flash Analog to Digital Converter (FADC) [125]. The ATWDs have three channels with different gains each one recording the first 420 ns of a waveform in 128 data blocks of 3.3 ns duration. The FADC allows to record longer waveforms up to 6.4μs with a 256 coarser data blocks of 25 ns duration.

The PMT is attached to the glass sphere using a room temperature vulcanization silicone (RTV) gel that serves also as an optical coupling to maximize photon transmission from the ice to the photo-cathode. Finally each DOM contains a flasher board with 12 LED pointing to different angles in a plane perpendicular to the IceCube array strings. The LEDs generate light that is used for calibration and studies of the ice optical properties as described next.

5.1.2 Optical Properties of the Antartic Ice

Since the reconstruction of events in the IceCube array depends on light detection the characteristics of the light propagation in the antartic ice are of major importance. The ice is the most transparent solid to photons in the range ~ 200 to ~ 400 nm [109]. However the presence of air bubbles and dust in the antartic ice affect the light propagation which is measured in terms of absorption and scattering properties.

Two methods were used to measure the light propagation properties of the antartic ice via the generation of artificial light sources and subsequent light detection at the DOMs. The first one was a dust logger device used during the deployment of the IceCube array DOMs and the second one is the flasher functionality of the deployed DOMs [127]. Figure 5.4 shows the measured absorption and scattering coefficients (a and b_ϵ) at the ice as function of the ice depth for a 10 m binning and a wavelength of 400 nm. The inverse of these coefficients determines the average distance a photon travel before being absorbed

($\langle 1/a \rangle \approx 110$m) and the average distance between consecutive scatterings ($\langle 1/b_\epsilon \rangle \approx 20$m).

A layered structure is observed in the measurement of the absorption and scattering coefficients. This structure corresponds to concentrations of dust that were produced by volcanic activity at the earth with subsequent accumulation of snow that compacts with time to form the antartic ice.

5.1.3 Data Acquisition and Triggering

Several processes generate noise hits at the PMT such as radioactive decays in the glass housing and thermal background of the photo-cathode that generate electrons which are further accelerated and multiplied. As a first step to reduce the number of DOMs with noise hits a digitized waveform in a given DOM is recorded and transmitted to the IceCube Control Lab (ICL) at the surface, only if a photon hit is recorded in the two neighbor DOMs, or next-to-nearest neighbor DOM, in the same string within a time window of ± 1 μs. This condition indicates that the waveform in a given DOM is product of external photons instead of noise hits of individual DOMs and is named *Hard Local Coincidence* or HLC.

The digitized and time-stamped waveforms at the DOMs are combined by requiring further trigger conditions. For the case of muon tracks, of interest for the current thesis, a Simple Majority Trigger or SMT is used. This trigger considers the waveforms of at least 8 DOMs with time-stamps within a time window of 5 μs. The waveforms within a time window of ± 10 μs around the trigger time are recorded and combined to form an *event*.

In general several photons could arrive to a given PMT within the ± 10 μs time window being recorded. If two photons arrive close in time the individual contributions overlap. An unfolding algorithm extracts from the digitized waveforms individual arrival times and collected charge using a template for a single-photo electron (SPE) response function. In this step the information from the ATWDs and FADC outputs is combined and possible differences in waveforms baselines are taken into account [128]. A series of several photo-electron response functions within a waveform is known as *Multiple-Photo-Electron pulse* (MPE).

After trigger conditions are full-filled several filters select events depending on the analysis being performed. The Muon filter for example (see section 5.3) selects track-like events based on several quantities such as a measurement of the direction reconstruction quality and energy-related quantities such as the total collected charge at the DOMs forming an events. The direction and energy reconstructions methods are described next.

5.2 Event Reconstruction

In an array of light sensors, such as the IceCube array, there are several characteristic Cherenkov light emission signatures; two of which are shown in Figure 5.5. In the case of a electron or tau neutrino interacting in the detector via CC interactions (see section 4.2) an

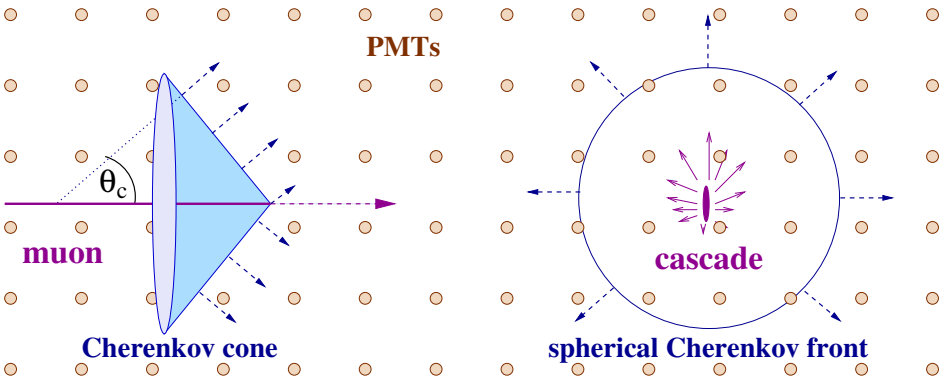

Figure 5.5: The two main event signatures in the IceCube array. Left: muon tracks produced by muon neutrinos. Right: Cascades produced by electron or tau neutrinos. Plot taken from [129].

electromagnetic cascade started by the produced lepton induce a spherical Cherenkov light pattern. On the other hand, for minimally ionizing muons (see section 4.2.2) produced either in a muon neutrino interaction or in the atmosphere, the light emission forms a Cherenkov cone that is detected as a track-like pattern. Muon track events are of particular interest for point source searches due to their sub-degree angular resolution at high energies (see section 5). The photon arrival time information and the collected charge at the involved DOMs in a event is used to reconstruct direction and energy-related variables as briefly described in next section. More detailed information on these reconstructions is found in Ref. [129]). Aspects taken into account in some of reconstructions include:

- Remaining noise hits. Before applying reconstruction algorithms to the data, DOMs known to have issues are marked and ignored. These issues include failed communication and high noise rates compared to other DOMs.

- Computational resources. Sophisticated reconstruction algorithms require certain processing time. Running these algorithms on all the events of the SMT, in the order of several thousands of events per second, is prohibitive due to the available computational resources at the South-Pole. The direction and energy reconstructions are performed in a iterative way starting from fast but simple algorithms. Quality criteria are used to select events on which more computational intensive reconstructions are applied.

- The characteristics of the ice optical properties affecting the light absorption and scattering.

- Coincident events. Two (or more) cosmic rays primaries can interact in the atmosphere and produce secondary muons from different directions in the same event within the ± 10 μs time window of the SMT.

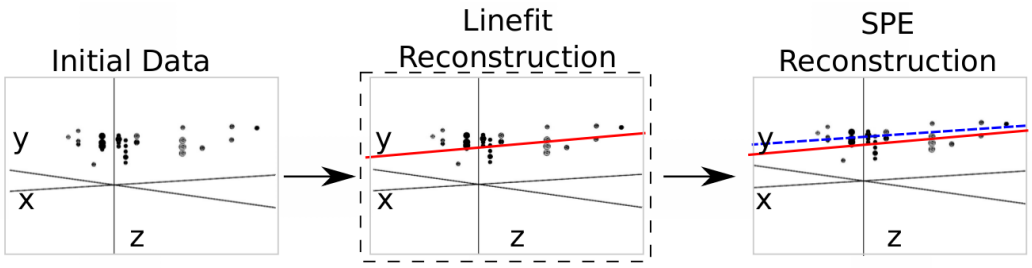

Figure 5.6: First three steps in the pipeline of a track direction reconstruction.

- Additional Cherenkov light induced by electro-magnetic cascades. These cascades are started by muon stochastic energy losses which dominates at muon energies around and above ~ 1 TeV (see section 4.2.2).

5.2.1 Direction Reconstruction

Figure 5.6 shows an sketch of the first steps taken in the direction reconstruction of muon tracks in the IceCube array. The position of a DOM i in a given coordinate system is $\vec{r}_i = (x_i, y_i, z_i)$. After noise hits are removed a total of N_{Hit} DOMs (black dots in Figure 5.6) are taken into account in the reconstruction algorithms. The simplest approach to obtain a first guess direction reconstruction is known as *Line-Fit*. This reconstruction ignores the Cherenkov nature of the light emission and the optical properties of the ice. It provides a fast way to estimate the direction of a muon track which is taken a seed for more sophisticated direction reconstruction algorithms such as the Single-Photo-Electron reconstruction (SPE) described later.

5.2.1.1 First Guess Direction Reconstruction

In the *Line-Fit* approach the muon track is taken as an infinite line. A point in this track with position $\vec{r}_0 = (x_0, y_0, z_0)$ emits light at a time t_0. The light travels in a straight line and is detected at a given DOM i at a time t_i. The arrival time t_i is taken as the first SPE hit extracted from the digitized waveform (see section 5.1.3). The position of the DOM $\vec{r}_i$ can be written as:

$$\vec{r}_i = \vec{r}_0 + \vec{v}(t_i - t_0), \tag{5.1}$$

where $\vec{v}$ is the velocity of the light in the ice. The values for $\vec{r}_0$ and $\vec{v}$ are estimated by minimizing the sum:

$$\chi^2 = \sum_{i=1}^{N_{\text{Hit}}} |\vec{r}_i - \vec{r}_0 - \vec{v}(t_i - t_0)|^2. \tag{5.2}$$

The advantage of this approach is that the χ^2 minimization have analytical solutions for

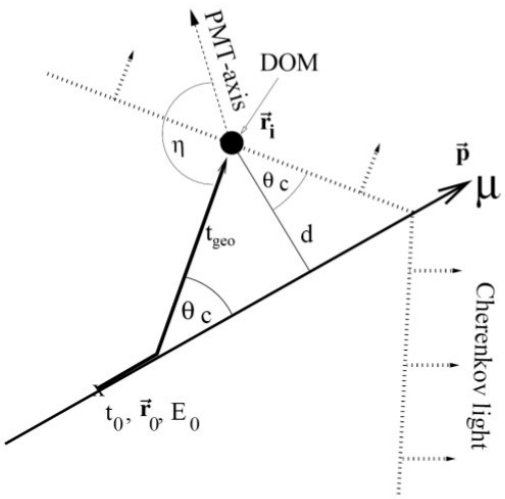

Figure 5.7: Geometric parameters for the propagation of a Cherenkov light cone induced by a muon with momentum p and energy E_0.

$\vec{r}_0$ and $\vec{v}$ reducing the calculation time with respect to more sophisticated reconstructions. The value of $|\vec{v}|$ can be used as a cut parameter to distinguish track and cascade events. The median angular resolution of this reconstruction is in the order of 5° depending on the muon energy [129].

5.2.1.2 Maximum Likelihood Reconstructions

Direction reconstructions that lead to sub-degree median angular resolutions are obtained by including more information in the reconstruction algorithm such as the nature of the light propagation, i.e the Cherenkov cone, and the effects of light absorption and scattering in the ice. Scattering effects are included by defining a time residual time as:

$$t_{\text{res}} = t_{\text{hit}} - t_{\text{geo}}, \tag{5.3}$$

where t_{geo} is the time an unscattered photon, propagating in a plane wave in the direction given by the Cherenkov cone, would take to travel from a certain point along the muon track $\vec{r}_0$ to a given DOM located at $\vec{r}_i$ (see Figure 5.7). The time t_{hit} is the measured arrival time at the same DOM.

In the Single-Photo-Electron reconstruction (SPE) the time t_{res}, as in the case of the *Line-Fit* reconstruction, is taken as the first SPE hit in time extracted from the digitized and unfolded waveform. The first hit is assumed to be created by the less scattered photon. For a total number of N_{hit} DOMs defining an event, a likelihood function is then defined as:

$$\mathcal{L}_{SPE} = \prod_{i}^{N_{\text{hit}}} p_1\left(t_{\text{res},i}|\vec{a}\right), \tag{5.4}$$

where $\vec{a}$ represents the free parameters of the track to be determined by maximizing $\mathcal{L}_{SPE}$ i.e the coordinates $\vec{r}_0$ of the vertex position at a given time t_0 and a direction given by a zenith (θ_0) and an azimuth (ϕ_0) angle. The function $p\left(t_{\text{res},i}|\vec{a}\right)$ is the probability density function (PDF) of measuring a time residual $t_{\text{res},i}$ given a track hypothesis $\vec{a}$. This PDF is given by a gamma distribution also referred as the *Pandel Function* [130]:

$$p_1(t_{\text{res},i}|\vec{a}) = \frac{\rho^{\eta} t_{\text{res},i}^{\eta-1}}{\Gamma(\eta)} e^{-\rho . t_{\text{res},i}}, \tag{5.5}$$

where $\eta = d/\lambda$ with d the perpendicular distance from the track to a DOM i (see Figure 5.7) and λ the mean photon scattering length. The parameter ρ is given by:

$$\rho = \frac{1}{\tau} + \frac{c_{\text{ice}}}{\lambda_a}, \tag{5.6}$$

where λ_a is the absorption length, c_{ice} is the speed of light in the ice and τ is a characteristic time parameter determined from photon propagation simulations.

The Multi-Photo-Electron reconstruction (MPE) takes into account the presence of N_i photon hits in a DOM i. The likelihood function in this case is defined as:

$$\mathcal{L}_{MPE} = \prod_{i}^{N_{\text{hit}}} p_1(t_{\text{res},i}, N_i|\vec{a}), \tag{5.7}$$

where the p.d.f $p(t_{\text{res},i}, N_i|\vec{a})$ is given by:

$$p_1(t_{\text{res},i}, N_i|\vec{a}) = N_i \cdot p_1(t_{\text{res},i}|\vec{a}) \cdot \left(\int_{t_{\text{res},i}}^{\infty} p_1(t|\vec{a}) dt \right)^{N_i - 1}. \tag{5.8}$$

For the maximization of the likelihood function in Eq. 5.7 the SPE reconstruction is taken as a seed. The track parameters in the SPE and MPE approaches are estimated by finding the global minimum of the negative log-likelihood $-log(\mathcal{L})$. The likelihood space defined in this way have several local minimum. In order to find the global minimum a pre-defined number of iterations for SPE and MPE minimizations are performed. The seed of each new iteration is the output of the previous iteration.

5.2.1.3 Rejection of atmospheric muon events

The dominant background in point source searches is composed of atmospheric muons (see section 4.3) generated in the southern hemisphere and reconstructed as *down-going* events i.e reconstructed with a Zenith angle $\theta < 90°$. A Bayesian approach is implemented to reduce some of this down-going tracks by defining the probability of observing the set of parameter of a muon track $\vec{a}$ given the set of hits x, using the Bayes theorem:

$$P(\vec{a}|\vec{x}) = \frac{P(\vec{x}|\vec{a})P(\vec{a})}{P(\vec{x})}, \tag{5.9}$$

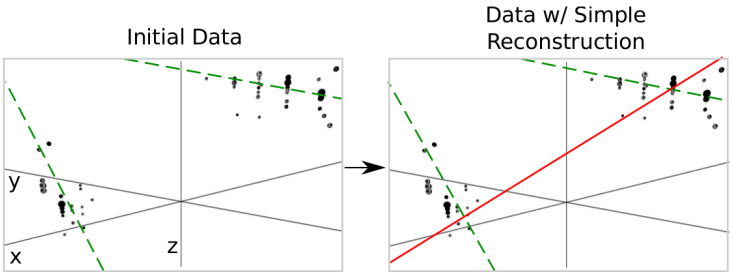

Figure 5.8: Example of two coincident down-going events (green-dashed lines) being reconstructed as an up-going event (red solid line).

where $P(\vec{x}|\vec{a})$ is given by the PDF in Eq. 5.5 and $P(\vec{a})$ is a prior probability taken as the normalized known zenith distribution of atmospheric muons [129]. A likelihood $\mathcal{L}_{Bayes}$ defined in this way describe the probability of an observed muon track being of atmospheric origin i.e generated in cosmic-ray showers.

Figure 5.8 shows an example of a *coincident event* in which two atmospheric muon tracks arrive within the a trigger time window defining an event. Within the category of coincident events also a neutrino-induced muon track and an atmospheric muon track could arrive within the same trigger window. If the track at the bottom arrives slightly earlier than the one at the top this set of hits is reconstructed as a up-going track ($\theta > 90°$). These mis-reconstructed events are rejected as up-going events by applying dedicated selection algorithms that split the set of DOM hits in two individual sets based on geometric and time conditions in order to reconstruct the track of each set of hit DOMs individually with the SPE and MPE approaches.

5.2.1.4 Uncertainty of the Direction Reconstruction

A semi-analytic method to estimate an angular uncertainty in the reconstructed directions based on the likelihood approaches described above (SPE and MPE) is described in Ref. [131]. The estimation of the angular uncertainty is extracted from the shape of $-\log(\mathcal{L}_{SPE/MPE})$ (Eq. 5.4 or Eq. 5.7) around its minimum. A narrow minimum indicates less uncertainty in the direction reconstruction than a broader one. The angular uncertainty for a event i with reconstructed direction (θ_i, ϕ_i) calculated with this method is referred as the *Paraboloid Sigma Error* σ_i.

It is worth to note that the estimate of the angular uncertainty, σ_i, depends on the energy of the event [132, 24]. This is because at high energies ($\gtrsim 1$ TeV) the direction reconstruction can be confused by the presence stochastic energy losses along the muon track which are not described in the likelihood function. This results in a underestimation of the angular uncertainty on the reconstructed direction of the track which is corrected based the real and estimated angular reconstruction calculated from Monte Carlo simulations.

The average angular resolution and pointing capabilities of the direction reconstruction

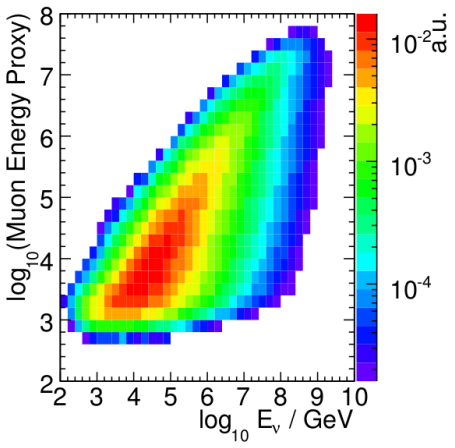

Figure 5.9: Distribution of the muon energy estimator versus the true neutrino energy simulated for a flux $dN/dE \propto E^{-2}$.

was obtained by the study of the so called "moon shadow": a deficit of muon track events around the the moon location. These studies confirm an absolute pointing of 0.7° in good agreement with the angular resolution calculated from simulations [11, 132]. The angular resolution obtained in the final event samples used in this thesis are shown in Figure 5.12.

5.2.2 Energy reconstruction

In contrast to cascade events interacting in the IceCube array (see Figure 5.5) muon track events as considered in the current thesis can interact outside the instrumented array and therefore the deposited energy within the detector is a fraction of the total energy. As mentioned in section 4.2.2 the muon energy loss scales with the muon energy at energies above ~ 1 TeV and therefore energy loss measurements provide an estimate of the total muon energy.

There are several methods developed in the IceCube Collaboration that provide energy estimators based on energy loss measurements. One of such method is described in Ref. [133] and referred as the MuE energy estimator. This method calculates the number of photons a muon with energy E_0 would emit via Monte Carlo simulations that take into account the ice optical properties to propagate the emitted photons until its detection at the DOMs. The measured photon density (photons per unit of distance) is shown to have a linear relation with the muon energy E_0 above 1 TeV and serves as an energy estimator. Figure 5.9 shows the distribution of the energy estimator versus the true neutrino energy for a simulated energy spectrum $dN/dE \propto E^{-2}$. The energy resolution of this estimator is 30% in log10(E/GeV).

Simpler approaches give energy-related estimates which are used as background rejection variables in early stages of the event selections, described in the next section, where fast

computation is needed. Some of these variables are the number of DOMs with hits in a given event and the total sum of collected charges in each DOM.

5.3 Event Selection

The SMT trigger described in section 5.1.3 selects around 2000 events per second for the 2011-2012 season which translates to about 1 TB of data produced per day. Since the satellite bandwidth allows about 100 GB of data transfer per day, an additional event selection known as the *Online Muon Filter* is performed in order to reduce the amount of events to be transferred via Satellite to the computer center at the North. After the data is transferred and stored additional *Offline processing* of the data takes place where more time-consuming reconstructions and high level event selections are performed. The main quantities considered in these event selection stages are:

1. Nch: The number DOMs (channels) considered in an event. It correlates with the neutrino-energy as high-energy neutrinos emit more light and more DOMs are activated.

2. Q_{tot}: With the same argument than Nch the charge collected in the PMT correlates with the neutrino energy. The variable Q_{tot} is the sum of the charges in the DOMs composing an event.

3. $rlogl$ and $plogl$: A measure of the quality of the fit defined as $-\mathcal{L}_{SPE/MPE}/(Nch-x)$ where $x = 5$ for $rlogl$ and $x = 2$ for $plogl$. Named the reduced log-likelihood it is analogous to the ratio $\chi^2/n.o.f$ in a χ^2 fit. Low values of these variables indicate a good quality fit.

4. $log(\mathcal{L}_{SPE/MPE}/\mathcal{L}_{Bayes})$: Bayesian Likelihood ratio. It is used to reduce the number of track events likely to be produced by atmospheric muons (see section 5.2.1.3).

5. $NDir$ and $LDir$: Number and length of Direct Pulses. A given photon hit is regarded as direct (less scattered) if the residual time t_{res} (see Eq. 5.3) is in the range $[-15$ ns : 75 ns$]$. The variable $NDir$ is the number DOM with hits that satisfy this condition. The variable $LDir$ is the maximum distance between two DOMs with direct hits which is a measure of the track length. Large values of these two variables indicate good quality muon tracks.

6. L_{empty}: It is defined as the maximum distance along the reconstructed track where DOMs in a cylinder of radius 150 m have no photon hits. Large values of this variable are an indication of coincident events.

7. σ: The estimate of the reconstruction error described in section 5.2.1.4. Small values of this parameter indicate better-quality muon tracks as the uncertainty in the reconstructed direction is small.

8. $v_{\text{Line-Fit}}$: The velocity parameter extracted from the Line-Fit reconstruction (see section 5.2.1.1).

9. MuE: the energy estimator described in the last section.

First Level Event Selection

The first stage in the event selection chain is performed directly at the computer center at the South Pole via the *Online Muon Filter*. Events in this stage are reconstructed using 4 iteration steps for the SPE reconstruction and the result is used as a seed for the MPE reconstruction. The *Online Muon Filter* select track-like events based on quality parameters of direction reconstruction ($plogl$) for up-going tracks and energy-related quantities (Nch and Q_{tot}) for down going tracks. The energy-related variables are used only on doing-going events in order to reduce in this first step the number of low energy atmospheric muons which is dominant in this region of the sky. With this selection the data rate is reduced to about 30 events per second [134].

Second Level Event selection

The second step in the event selection further reduce the number of up-going events by introducing a selection criteria in the form of cuts on event variables such as L_{empty}, $plogl$ and a variable named the Direct Ellipse cut defined as $(LDir/60)^2 + (NDir/15)^2$. At this stage 32 iterations are used for SPE reconstruction and as in the previous stage the output of this reconstruction is used as a seed for the MPE reconstructions as well as for the MuE energy estimator and for the Bayesian reconstruction. In a following step the time-consuming splitting procedure to reconstruct coincident events (see section 5.2.1.3) is performed and the selection criteria with the variables described above is applied for each individually reconstructed event.

With this selection the data rate is reduced to about 1 event/second with a signal efficiency (fraction of signal events kept after the selection) of 86% estimated from Monte Carlo simulations of signal events [134]. For down-going events zenith-dependent energy cuts are applied in order to further reduce the number of atmospheric muon events that passed the *Online Muon Filter* [134].

Final Level Event Selection

Season 2009-2010 (IC59)

The event selection for this season is described in detail in Ref. [135]. The final event selection for up-going events for this season makes use of a Boosted Decision Tree (BDT). A BDT is a machine learning algorithm designed to take into account several variables to calculate a single quantity (score) used to separate two population of events with different

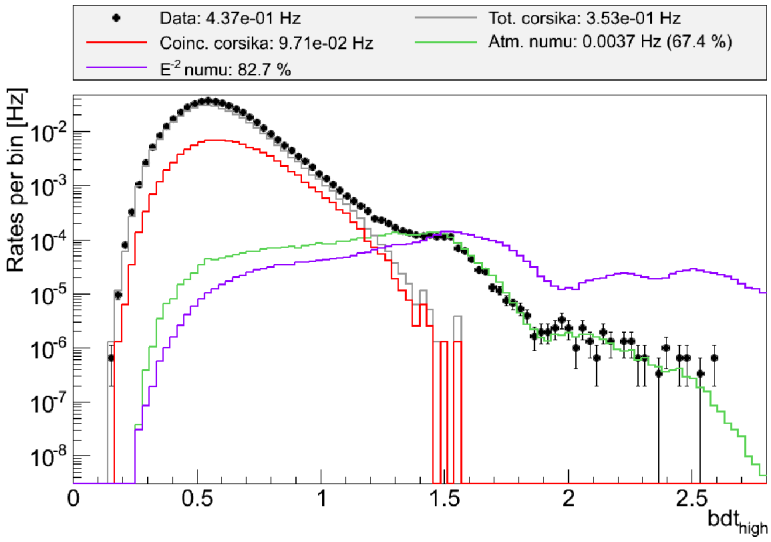

Figure 5.10: Boosted decision tree score (bdt_{high}) for the 2009-2010 data sample. Both Monte Carlo simulation and data distributions are shown. The final event selection correspond to the events with $bdt_{high} > 1.4$. Taken from Ref. [135].

characteristics. For the case event selection described here the two populations correspond to background (atmospheric muons and neutrinos) and signal events (astrophysical neutrinos). Higher values of the BDT score indicate that a given event is more "signal-like".

The variables taken into account in this selection include all the variables listed at the beginning of this section with the exception of L_{empty} and Q_{tot} resulting in the BDT score distribution shown in Figure 5.10. The total number of selected events for this selection and is shown in Table 5.1.

For the down-going region instead of a BDT straight cuts are used. These cuts are done in variables such as $plogl$, σ and a zenith-dependent energy cut used to reduce the number of low energy atmospheric neutrinos which selects a constant number of events per solid angle. In addition, the IceTop array is used as a veto since atmospheric muon events with zenith angles close to 0° are likely to produce hits in the IceTop DOMs product of the air shower in which they were created.

Season 2010-2011 (IC79)

For the event selection of the 2010-2011 season a similar approach to the 2009-2010 selection is performed. For the up-going region the data is divided into two different zenith angle samples: horizontal events (between $85^\circ - 130^\circ$) and vertical events ($130^\circ - 180^\circ$). This regions are motivated by earlier observations of cut efficiencies being zenith dependent [134]. For some variables tight cuts yield to a good signal efficiency for the horizontal region while it decreases for the vertical region in particular considering soft energy spectra

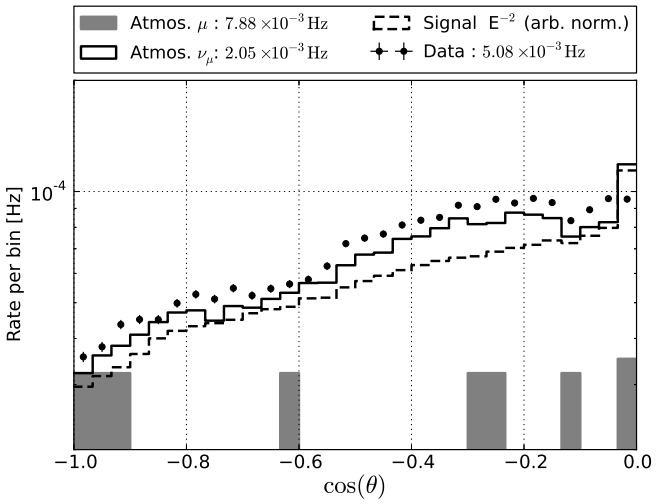

Figure 5.11: Distribution of events in Cos(Zenith) for the 2010-2011 (IC79) event sample. Taken from [14]

(the energy spectral index $\gamma < 2$) for the simulated signal.

For each zenith region a separate BDT was used including a total of 17 variables that showed signal-background discrimination power and described in Ref. [134]. The final BDT score is chosen according to the best sensitivity obtained (see section 6.2 for the sensitivity definition). Figure 5.11 shows the zenith angle distribution for events in the up-going region. A rate of 2×10^{-3} events per second is obtained with less than 3% estimated atmospheric muon contamination [14]. An IceTop veto and a zenith-dependent energy cut plus a dedicated BDT were used to select events in the down-going region. The total number of selected events in both selections is shown in Table 5.1.

Season 2011-2012 (IC86-I)

Similar to the 2010-2011 season different BDTs are used for different zenith angle regions for the 2011-2012 season. The main difference with respect to event selections in the previous seasons come in the treatment of the down-going region. Eleven variables are used in the BDT for the down-going region from which three exploit differences in the energy loss profile of single muons and muon bundles (see section 4.3.1). Individual atmospheric muons produced in a bundle have energies below the minimal ionization regime which translates in a smooth energy loss and profile and light production rate along the track. On the other hand, neutrino-induced muons above ~ 1 TeV exhibit stochastic energy losses manifested in electromagnetic cascades that emit light in narrow time windows. A likelihood ratio is calculated to estimate the probability of an observed muon track to have energy loss pattern compatible with stochastic energy loses and is included in the BDTin order to reduce the muon bundle background. The total number of events selected is shown in Table 5.1.

Figure 5.12 shows the median angular resolution for reconstructed neutrino-induced muon tracks for the three data samples used: 2009-2010 (IC59), 2010-2011 (IC79) and 2011-2012 (IC86-I) as function of the neutrino energy. Each data taking season brought improvements in the event selection and reconstruction algorithms resulting in a improvement of the median angular resolution from season to season. Angular resolutions better than 1° are achieved above 1 TeV for the 2011-2012 season.

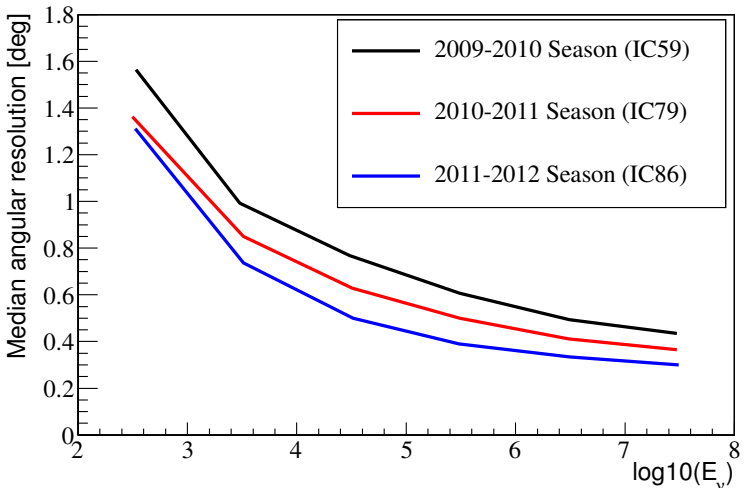

Figure 5.12: Median angular resolution of down-going neutrino-induced muon events as function of the incoming neutrino energy for the three data samples used in this thesis: 2009-2010 (IC59), 2010-2011 (IC79) and 2011-2012 (IC86-I).

Data sample name	Start time (MJD)	End time (MJD)	Livetime (days)	# Atm. ν per day	# Up-going events	# Down-going events
IC59	2009 May 20 (54971)	2010 May 31 (55347)	348	120	43339	64230
IC79	2010 May 31 (55347)	2011 May 13 (55694)	316	180	50857	59009
IC86-I	2011 May 13 (55694)	2012 May 16 (56063)	333	210	69227	69095

Table 5.1: IceCube data-sets used in the astrophysical neutrino searches described in the next chapters. The number of atmospheric neutrinos per day in the 6th column are calculated from Monte Carlo simulations [23].

Chapter 6

Analysis Methods for Point Source Searches

As described in the previous chapter, the final event sample contains up-going track-like events induced by atmospheric neutrinos arriving from the northern sky, a small fraction of up-going tracks due to mis-reconstructed atmospheric muons from the southern sky, and a sample of down-going tracks induced mostly by atmospheric muons.

At this point several analyses could be performed in order to test the hypothesis of having a population of signal events, i.e astrophysical neutrinos produced by a point source, within the selected event sample. This chapter describes the main statistical tool used in such analyses, known as the the unbinned maximum likelihood method, in which energy, direction and time information are used to discriminate signal from background. The search methods developed in the current thesis are based on this statistical tool and are described in the next chapter.

6.1 The Unbinned Maximum Likelihood Method

The unbinned maximum likelihood method tests the hypothesis of having a population of signal events within the selected data sample. The likelihood function is defined as:

$$\mathcal{L}(n_s, \gamma_s) = \prod_{i=1}^{N} \left(\frac{n_s}{N} S_i + \left(1 - \frac{n_s}{N} \right) B_i \right), \tag{6.1}$$

where n_s and γ_s are free parameters that represent the number of signal events and the signal spectral index, assuming a power law energy spectrum, respectively. The best estimates of these two parameters, $\hat{n}_s$ and $\hat{\gamma}_s$, are calculated from the likelihood fit to the data. These are the values that give the maximum value $\mathcal{L}(\hat{n}_s, \hat{\gamma}_s)$. The product goes over each event i of the selected data sample composed of N total events within a zenith band around the candidate source position. B_i and S_i are the signal and background probability density functions PDFs. These PDFs integrated over the parameter space considered (space, energy or time) give the probability of each event being either a background event or a signal event and are described next.

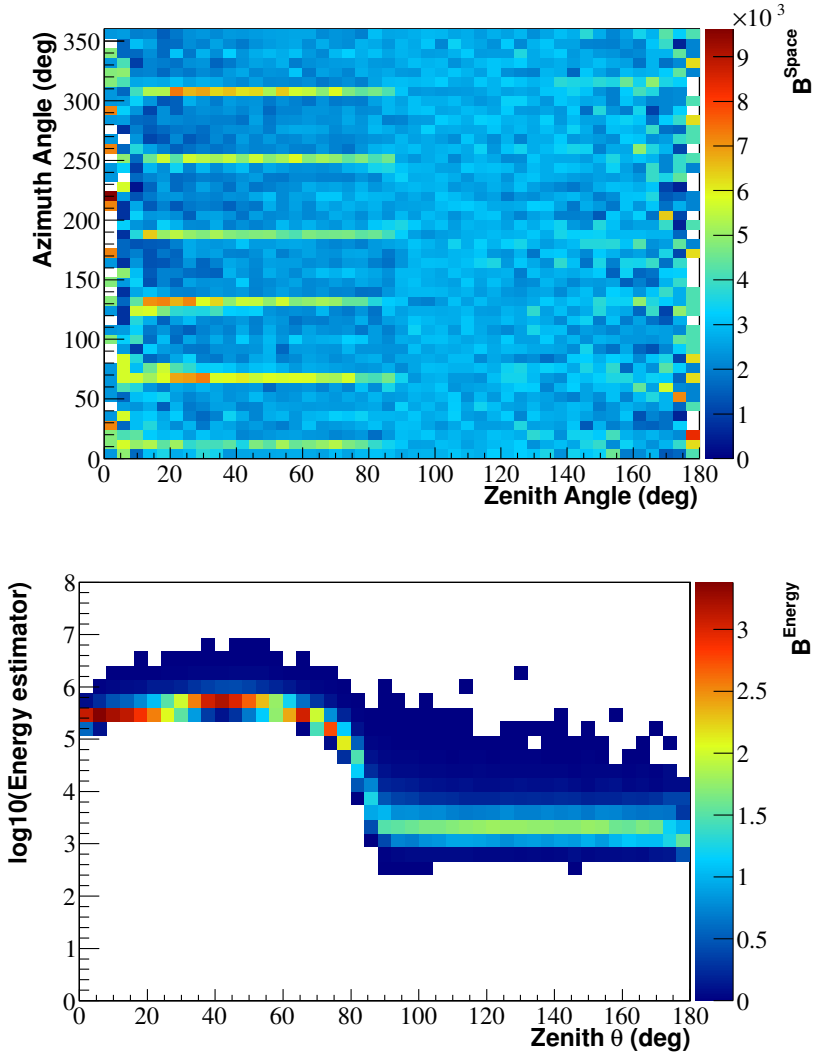

Figure 6.1: Top: Space component of the Background Probability Density Function $B^{\text{Space}}(\vec{x}_i)$. Six distinctive bands appear in the azimuth distribution due to filter conditions (see text). Bottom: Energy component $B^{\text{Energy}}(\vec{x}_i, E_i)$. The energy distribution of selected events depend on the reconstructed zenith angle. The probability density functions shown here are built from data distributions of the 2010-2011 (IC79) IceCube data-set.

6.1.1 Background Probability Density Function

The background PDF in Eq. 6.1 is defined as:

$$B_i = B^{\text{Space}}(\vec{x}_i) B^{\text{Energy}}(\vec{x}_i, E_i), \tag{6.2}$$

where $\vec{x}_i = (\theta_i, \phi_i)$ and E_i are the reconstructed direction and energy of each event i. θ_i and ϕ_i are the reconstructed zenith and azimuth angles respectively.

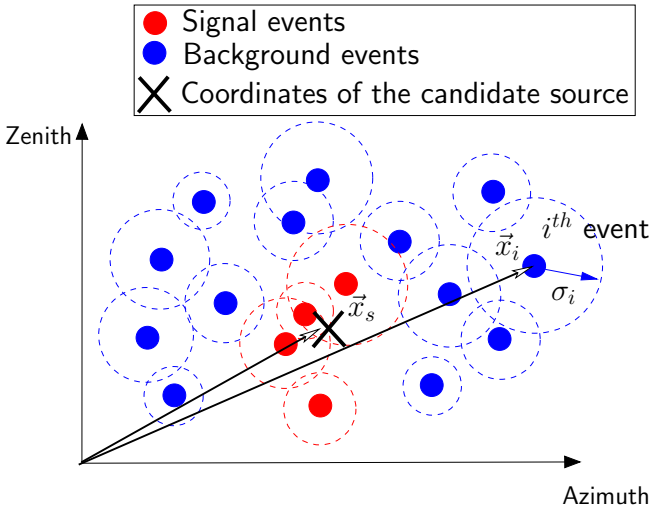

Figure 6.2: Sketch of an space clustering of events around a candidate source with coordinates $\vec{x}_s$ in the Zenith-Azimuth plane. The vector $\vec{x}_i = (\theta_i, \phi_i)$ and the parameter σ_i are the direction and reconstruction error estimates for each event i of the data sample.

The first term $B^{\text{Space}}(\vec{x}_i)$ describes the distribution in space of the events in the data sample. In the ideal case this PDF should be uniformly distributed since no spatial clustering is expected in the background events. Figure 6.1 (Top), shows the normalized distribution of the reconstructed arrival direction of the events in the 2010-2011 IceCube data-set (IC79). There are six distinctive bands in the southern sky ($\theta < 90^\circ$) which are generated by initial filter conditions that select more efficiently muon tracks that pass close to strings aligned with the six main axis of the detector geometry. By using the normalized distribution of arrival directions as background PDF this bands are automatically taken into account.

The second term $B^{\text{Energy}}(\vec{x}_i, E_i)$ describes the distribution of the energy estimator E_i. This distribution depends on the zenith angle as shown in Figure 6.1 (right). This dependence comes from two effects: zenith-dependent energy cuts were applied in the data selection in order to reduce the atmospheric muon background in the southern sky (see chapter 5) and earth absorption effects, discussed in chapter 4, makes more likely that high energy neutrinos in the PeV-EeV range interact close to the detector if they come from the southern sky (Zenith angle$< 90^\circ$) while they are absorbed if they transverse the earth (Zenith angle$> 90^\circ$).

6.1.2 Signal Probability Density Function

A point source of high energy astrophysical neutrinos is expected to manifest itself in the data as a set of events clustered in space around the position of the candidate source $\vec{x}_s$. The Signal PDF is defined as:

$$S_i = S^{\text{Space}}(|\vec{x}_i - \vec{x}_s|, \sigma_i) S^{\text{Energy}}(E_i, \gamma_s, \vec{x}_i), \tag{6.3}$$

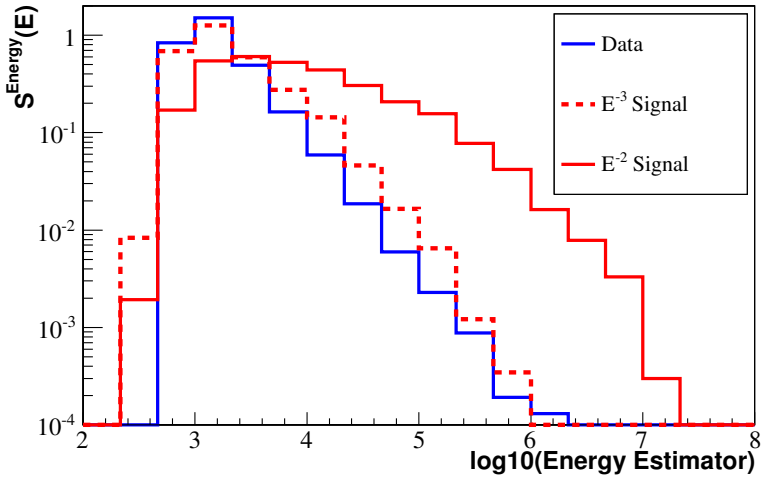

Figure 6.3: 1D projections of the energy Probability Density Function $S^{\text{Energy}}(E_i, \gamma_s, \vec{x}_i)$ for $\theta_i = 106^\circ$ and 2 values of the signal spectral index γ_s assuming a power law energy spectrum (red histograms). As a comparison the normalized energy distribution of real data is shown in blue. This corresponds to the projection of the background PDF $B^{\text{Energy}}(\vec{x}_i, E_i)$ for $\theta_i = 106^\circ$ (see Figure 6.1).

where the first term is given by:

$$S^{\text{Space}}(\vec{x}_s, \vec{x}_i, \sigma_i) = \frac{1}{2\pi\sigma_i^2} \exp^{-\frac{|\vec{x}_i - \vec{x}_s|^2}{2\sigma_i^2}} . \tag{6.4}$$

This term depends on the event direction reconstruction $\vec{x}_i$ and on the event reconstruction error σ_i. An illustration of a space clustering is presented in Figure 6.2. Depending on the event direction and reconstruction error, events close to a candidate source have a higher value of S^{Space} while events with reconstruction direction $\vec{x}_i$ far away from the source position $\vec{x}_s$ have small values of S^{Space}. To reduce the calculation time of the likelihood maximum only N events contained in a zenith band around the source position $\vec{x}_s$ are used. The size of this band is chosen to be larger than the events angular resolution typically of a few degrees in zenith. For the analysis described in the next chapter a value of 10° was chosen.

The second term of Eq. 6.3 $S^{\text{Energy}}(E_i, \gamma_s, \vec{x}_i)$ describes the distribution of the energy estimator for signal events. It is constructed from simulations of a population of neutrinos interacting with the detector with a energy distribution following a power law of spectral index γ_s. Due to the earth absorption (see section 4.2.1) this PDF depends also on the direction reconstruction $\vec{x}_i$.

Figure 6.3 shows the background and signal energy PDFs for a particular direction in the sky and different simulated spectral indexes. Events with a higher reconstructed energy

have a higher probability of being of astrophysical origin depending on the spectral index of the corresponding energy distribution.

In order to take into account the zenith and spectral index dependence of this PDF a 3D histogram is used in the likelihood maximization step. 2D projections of this histogram are shown in Figure 6.4.

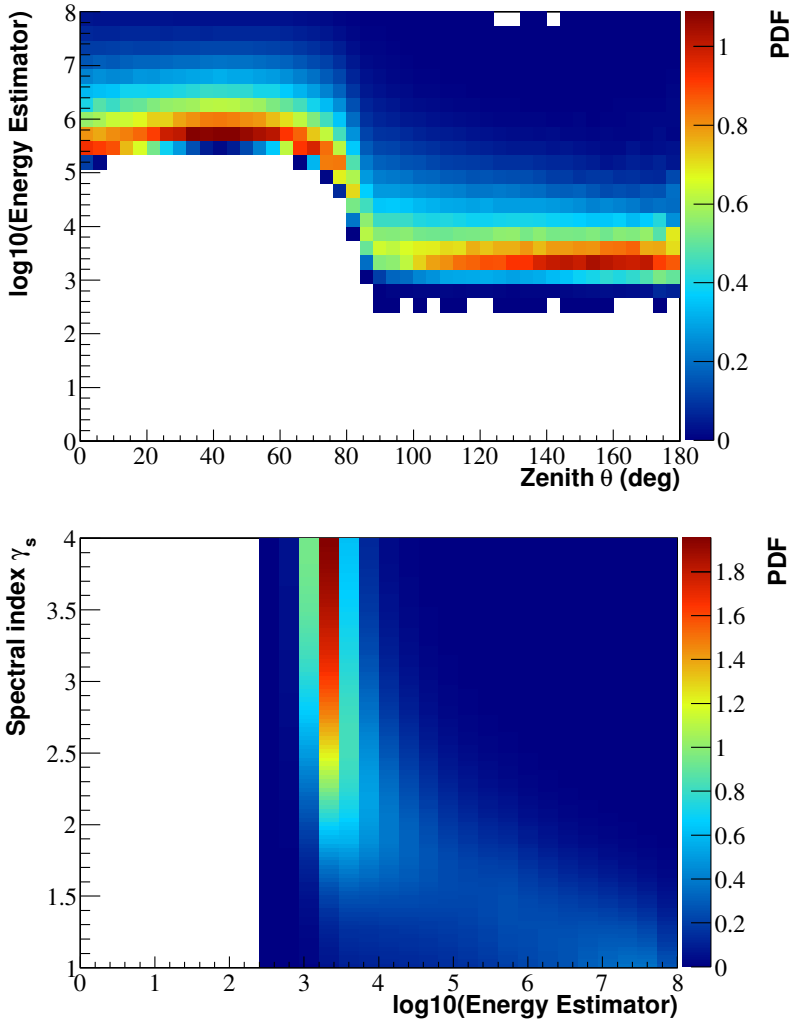

Figure 6.4: 2D projections of the 3D signal energy PDF $S^{\text{Energy}}(E_i, \gamma_s, \vec{x}_i)$. Top: Projection of the Signal Energy PDF in the Zenith-Energy plane for $\gamma_s = 2$. Bottom: Projection of the Signal Energy PDF in the γ_s-Energy plane.

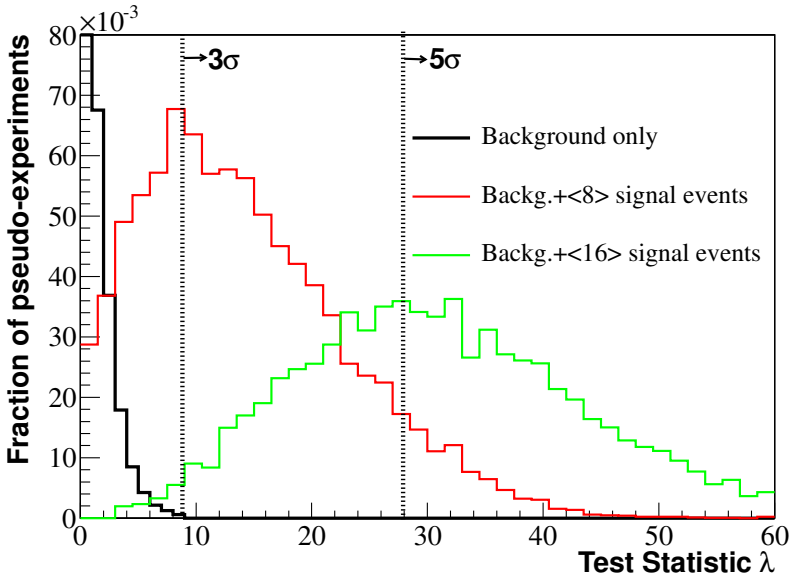

Figure 6.5: Test statistic distributions for background-only and signal plus background pseudo experiments.

6.2 Discovery Potential, Sensitivity and Upper Limits

The Test Statistic

The test statistic of the hypothesis test approach is defined as the likelihood ratio:

$$\lambda = -2\log\left(\frac{\mathcal{L}(n_s = 0)}{\mathcal{L}(\hat{n}_s, \hat{\gamma}_s)}\right), \tag{6.5}$$

where $\hat{n}_s$ and $\hat{\gamma}_s$ maximize the likelihood in Eq. 6.1. Large values of λ indicate less compatibility with the background-only hypothesis i.e $\mathcal{L}(n_s = 0)$.

Several quantities helpful to evaluate the performance of the search method and the significance of an observation (discovery potential, sensitivity and upper limits), are defined on basis of the background-only and signal plus background test statistic distributions as described below. Figure 6.5 shows the normalized distributions of test statistic values λ calculated from Monte Carlo simulations both for background-only and background plus signal simulations. Each entry in this distribution corresponds to a particular realization of simulated data which generation, used in the search methods described in the next chapter, is described next.

Generation of Pseudo-experiments

Simulated data realizations, or pseudo-experiments, are built by scrambling real data parameters such as the direction reconstruction, reconstruction error and energy estimator of

each event in the data sample. In this way the set of real event parameters in the data are kept blind while the performance of the method is evaluated.

The scrambling procedure starts with N events from real data i.e the total number of events in a declination band of width 10° centered in the source position $\vec{x}_s$. For each background-only pseudo-experiment the total number of events on it is drawn from a Poisson distribution with mean N. The parameters of each pseudo-event are drawn from histograms built from data. The procedure follows the next sequence:

1. A zenith angle value is drawn from the real data zenith distribution i.e the projection in the x axis of the Zenith-Azimuth 2D histogram shown in Figure 6.1.top.

2. Given the chosen zenith angle an azimuth angle value is drawn from the projection on the y axis of the same 2D histogram. This is done to take into account the asymetry in the Azimuth distribution that depends on the Zenith angle as shown in Figure 6.1 Top.

3. Given the chosen zenith angle a energy estimator value is drawn from the projection on the y axis of the Zenith-Energy 2D histogram (Figure 6.1 Bottom).

4. Given the chosen value of the energy estimator, a value for the uncertainty of the direction reconstruction is drawn from a 2D histogram built with these two parameters. This step is performed to take into account the dependence of the angular uncertainty estimator on the energy of a given event as described in section 5.2.1.4.

5. A time value is drawn from the time distribution of real events in order to take into account the dead time of the detector not to simulate events during this time.

The scrambling procedure hides the presence of a possible population of events with the parameters of a signal population i.e a population of muon track events clustered around a particular direction in the sky and with high values of reconstructed energy. Scrambled data is then treated as background-only pseudo-experiments.

Signal plus background pseudo-experiments are generated by injecting signal-like events on top of the background-only pseudo-experiment. Signal-like events are injected as a set of events clustered in space around a given direction in the sky $\vec{x}_s$. The signal events are injected following a power law energy distribution with a given spectral index taking as a benchmark $\gamma_s = 2$. For each scrambled map the number of signal events injected is drawn from a Poisson distribution with mean n. The resulting test statistic distributions are shifted to higher values and its mean increases with the number of injected signal events n as shown in Figure 6.5.

Definition of Performance Parameters

Several quantities of interest to evaluate the performance of the search method are defined in terms on a reference value of the test statistic λ_{ref}:

- *p-value*: This is a parameter used as a measure of the compatibility of the data sample with the background-only hypothesis. It is defined as the fraction of background-only pseudo-experiments with a corresponding test statistic larger or equal to the reference level λ_{ref} i.e the tail probability of the background distribution shown in Figure 6.5. Small values of this parameter indicates less compatibility with the background-only hypothesis.

  It is common practice in particle physics to cite the p-value of an observation in terms of a number of standard deviations σ. This correspond to the a measure of how far the observation is from the bulk of the expected background distribution assuming that it has Gaussian tails. In this approximation the relation of the p-value with σ is given by [136]:

  $$\sigma = \sqrt{2} \times \text{erf}^{-1}(1 - 2 \times \text{p-value}), \tag{6.6}$$

  where erf^{-1} is the inverse of the error function. The smaller the p-value the larger the significance of the observation. Figure 6.5 shows the values of λ_{ref} that result in a p-value corresponding to 3 and 5σ deviations. A 5σ deviation indicate a discovery in the convention usually adopted in particle physics.

- *Discovery potential*: The discovery potential is defined as the number of signal events μ_d required to obtain a p-value less than 2.87×10^{-7} (5σ significance) in 50% of the pseudo-experiments. The reference test statistic λ_{ref} is given by the median of the signal+background test statistic distribution obtained for the parameter μ_d.

- *Upper limit (at 90% confidence level)*: Given the value obtained in real data ($\lambda_{\text{ref}} = \lambda_{\textbf{Data}}$) the p-value of the observation is defined as the fraction of pseudo-experiments with $\lambda \geq \lambda_{\textbf{Data}}$. The upper limit is defined as the number of signal events μ_{90} required to obtain this p-value in 90% of the pseudo-experiments.

- *Sensitivity*: The sensitivity is defined here as the average upper limit obtained under the null hypothesis. In this case the reference test statistic λ_{ref} is given by the median of the background-only test statistic distribution. The event sensitivity is defined as number of signal events $\bar{\mu}_{90}$ required to obtain a p-value less than 0.5 in 90% of the pseudo-experiments.

The discovery potential, sensitivity and upper limits can also be expressed in terms of a flux amplitude constant, instead of number of signal events $\mu = (\mu_d, \mu_{90}, \bar{\mu}_{90})$, as [137]:

$$\Phi = \Phi_0 \frac{\mu}{N(\Phi_0)}, \tag{6.7}$$

where Φ_0 is the amplitude constant of a reference flux (for example $dN/dE = \Phi_0 E^{-2}$) and $N(\Phi_0)$ is the number of signal events that would be observed in the detector for the flux Φ_0 and is calculated from Monte Carlo simulations.

6.2.1 Trial Factor

When performing a statistical test in search for a signal, one has to take into account that the probability of observing a positive result due to background fluctuations increases if several independent statistical tests (trials) are performed. This is known as the look-elsewhere effect [138] and it is quantified by the use of the so called trial factor. This factor relates the p-value of a single trial, $P_{\text{pre-trial}}$, with the p-value corrected for performing several trials $P_{\text{post-trial}}$:

$$P_{\text{post-trial}} = T \times P_{\text{pre-trial}}. \tag{6.8}$$

for a number of independent trials N_T and assuming binomial statistics the trial factor is given by:

$$T = \frac{1 - (1 - P_{\text{pre-trial}})^{N_T}}{P_{\text{pre-trial}}}. \tag{6.9}$$

For $P_{\text{pre-trial}} \ll 1 \rightarrow T \approx N_T$. The post-trial p-value increases, and the significance decreases, with increasing number of trials N_T. If the trials are not independent, as in the case of overlapping regions in the sky being scanned, simulations are needed to estimate the trial corrected p-value $P_{\text{post-trial}}$. For the searches developed in this thesis this is calculated via pseudo-experiments. A set of pseudo-experiments is generated for each source in the selected list of sources to be tested and a distribution is built with the maximum test statistic λ obtained in each pseudo-experiment. The trial-corrected p-value is then the tail probability of this distribution given the observed value of the test statistic λ_{Data}.

6.3 Time-Integrated Point Source Searches

Several analysis of IceCube data have used the unbinned likelihood method to search for point sources using muon tracks. A time-integrated analysis looks for an excess of events using only energy and space information as described in section 6.1. There are several ways to perform such searches that include:

1. *Selected candidates search*: only selected positions $\vec{x}_s$ in the sky corresponding to promising neutrino sources are chosen. The test statistic is calculated for each one of these sources.

2. *Stacking analysis*: Several promising sources of a particular category (AGN, Starbust galaxies, molecular clouds...etc) are considered together in the same statistical test. In this way the individual contributions of each potential source are added up. This analysis modifies the signal PDF described in Eq. 6.3 in order to take into account several sources in the likelihood test (see section 7.3 for an example).

3. *All Sky search:* A test statistic is calculated for each bin of a predefined grid covering the sky. In this case the center of each bin defines the source position $\vec{x}_s$ of Eq. 6.4.

The large number of trials performed in the *All sky search* (one for each bin in the grid) implies a larger trial factor than the *Selected sources search*.

Time integrated analyses based on the muon track event selection described in chapter 5 have not found a significant excess of signal events i.e the observations are compatible with the background-only hypothesis [139, 24]. As described in the next section time-dependent analysis make use of the additional discrimination power between signal and background events obtained by including timing information in the likelihood test.

6.4 Time-Dependent Point Source Searches

Several time-dependent search methods have been developed in order to take into account the possible time variability of the neutrino sources described in section 3.3. While some of these methods are briefly described in this section, the search methods developed in the current thesis explore complementary scenarios of time-dependent neutrino emission and are described in the following chapter.

In a time-dependent search a new likelihood function of the form Eq. 6.1 is defined by including additional PDFs, which depend on the arrival time of the muon-track events t_i, as multiplicative factors in the signal and background PDFs described in sections 6.1.1 and 6.1.2. The PDFs in time-dependent searches are then defined as:

$$B_i = B^{\text{Space}}(\vec{x}_i) B^{\text{Energy}}(\vec{x}_i, E_i) B_i^{\text{Time}}(t_i, \vec{x}_i), \tag{6.10}$$

$$S_i = S^{\text{Space}}(\vec{x}_s, \vec{x}_i) S^{\text{Energy}}(E_i, \gamma_s, \vec{x}_i) S_i^{\text{Time}}(t_i). \tag{6.11}$$

The background time PDF $B_i^{\text{Time}}(t_i, \vec{x}_i)$ is built from data. Figure 6.6 shows the uptime corrected event rate [1] as function of time for the 2009-2010 IceCube data set for the up-going events (Northern Sky) and the down-going events (Southern sky). Changes in the temperature of the atmosphere produces changes in the event rate (see section 4.3). These changes are small for the northern sky dominated by atmospheric neutrinos ($\sim 2\%$), and the event rate is well fit with a constant function $F(t_i, \theta_i > 90^\circ) = C$. The southern sky is dominated by atmospheric muons and the event rate is well fit with a sinusoidal function $F(t_i, \theta_i < 90^\circ) = a \sin(bt_i + c) + d$ with a, b, c, d being the free parameters in the fit. The event rate in the southern sky change $\pm 10\%$. The time PDF is then defined as:

$$B_i^{\text{Time}}(t_i) = \frac{1}{\Delta T_{Data}} F(t_i, \theta_i), \tag{6.12}$$

where ΔT_{Data} is the uptime of the data period considered.

Each time-dependent method briefly described in the next sections defines a particular signal time PDF $S_i^{\text{Time}}(t_i)$. These signal PDFs characterize the temporal behavior of the

[1] The data quality selection and the dead time of the detector produces time gaps in the data. The average uptime of the three data sets used in this thesis is 92%.

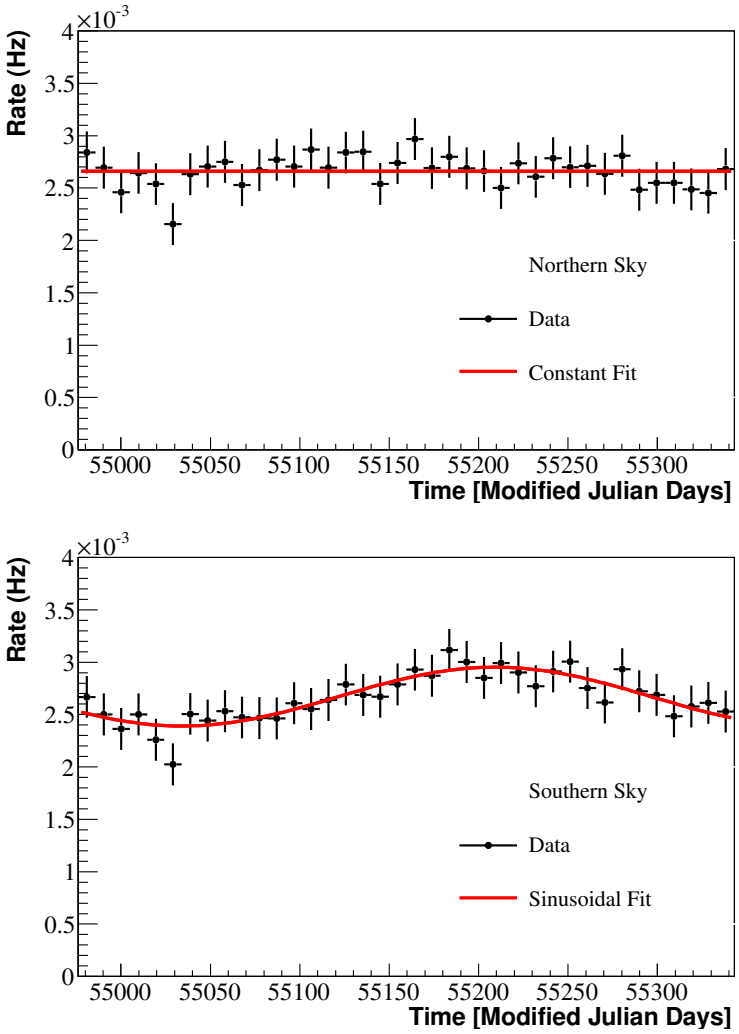

Figure 6.6: Distribution of the arrival time of the events for the 2009-2010 IceCube data set (IC59) in the northern sky (top) and in the southern sky (bottom). For the events in the northern sky a constant fit is used to define the time PDF while a sinusoidal fit is used in the events from the southern sky.

potential neutrino source in order to investigate several possible scenarios in the time domain. Two additional time-dependent methods were developed in the current thesis and are described in the next chapter.

Single Flare Search

Single flare searches aim to find the most significant set of events clustered in time at any point in the sky. The time signal PDF $S_i^{\mathsf{Time}}(t_i)$ is defined either as a box function with

variable width [24] or as a Gaussian function with its centroid and width taken as free parameters in the likelihood maximization [140].

The method is sensitive to a wide region of flare durations (from seconds to several weeks) which do not have necessarily an electromagnetic counterpart hence are also referred as un-triggered searches. In principle short bursts with durations of about 10s may be discovered at a 5σ level with approximately 2 events [22, 23]. A search of this kind described in reference [24], looked for neutrino flares in the direction of selected source candidates whereas the search in references [140, 23] is an All-sky search.

Triggered Searches

The signal hypothesis in this kind of searches assumes a one to one correlation of the arrival times of an astrophysical messenger and the possibly associated high energy neutrino flux. For example, measurements in GeV or TeV gamma-rays could indicate a flaring episode and a functional form for the time PDF $S_i^{\mathsf{Time}}(t_i)$ could be defined with this information.

The searches in Refs. [22, 141, 23] use experimental light curves obtained in the GeV band with the Fermi-Large-Area-Telecope to define the signal time PDF and test the hypothesis of a high energy neutrino flux emitted in coincidence with the observed gamma-ray flares.

Neutrino Follow-Up Programs

The two methods described so far are performed in "offline-mode". In this mode, due to several factors, the statistical test is performed up to several months after the data is acquired. This factors include availability of good quality trigger data and time-consuming procedures in the analysis such as sophisticated direction and energy reconstructions, selection of well reconstructed events, additional background reduction and the implementation of the statistical test itself.

Assuming that the high energy neutrinos are emitted in coincidence with photons at different wavelengths (either TeV gamma-rays, X-rays or optical) real-time analysis are needed in order to perform simultaneous measurements of these messengers. Dedicated event selection and statistical analyses have been implemented in recent years to take into account the timing properties of muon track events in real time to select promising time windows for neutrino emission. Given pre-defined significance thresholds of these time windows, alerts are sent from IceCube to telescopes sensitive to several wavelengths in order to trigger follow-up measurements in real time [142, 143].

6.4.1 Fluence Definition

It is usual to express the sensitivity and upper limits of a time-dependent search in terms of fluences. The fluence is defined as the integral in time of the energy flux density [144]:

$$f = \int dt \int_{E_{\min}}^{E_{\max}} dE \times E \left(\frac{dN}{dE}\right) = \Delta t \int_{E_{\min}}^{E_{\max}} dE \times E \left(\frac{\Phi}{E^2}\right) = \Delta t \Phi \ln\left(\frac{E_{\max}}{E_{\min}}\right), \quad (6.13)$$

where Φ is the amplitude constant of the flux during the duration of emission $\Delta t =$ (see Eq. 6.7). The duration of the emission Δt depends on the time PDF considered in each time-dependent analysis. As a convention within IceCube, the energy limits $E_{\min}$ and $E_{\max}$ are taken as the 5% and 95% percentile of the energy distribution of simulated signal events for a given declination band.

Chapter 7

The Multi-Flare Analyses

In this chapter two new time-dependent search methods are described. The first approach consists in a statistical test based on the unbinned maximum likelihood designed to look for a set of high energy neutrino flares here after called the Multi-flare analysis. The second approach (the Multi-flare stacking analysis) groups the selected sources in order to test the hypothesis of a cumulative time-dependent signal built by their individual contributions. The performance of these two methods is investigated for different simulated signal scenarios.

7.1 Rationale of the Method

The Multi-flare analysis is a search method complementary to the time-dependent methods described in section 6.4. Single-flare searches, for example, select only the most significant time window from a list of tested sources or from each bin in the sky. The information of other time windows is lost. As described in the next section, the Multi-flare method takes into account these other time windows in a single statistical test making the analysis sensitive not only to a single, and strong, flaring episode but to several ones, possibly weaker by their own, distributed in different ways in the time domain over the data taking period considered.

In triggered searches, on the other hand, a certain degree of model dependence arises which limits the parameter space being investigated. For example, in the case of the triggered search based on GeV light curves, it is assumed that all the photon flares observed are hadronic in nature and therefore high energy neutrinos are being emitted in time coincidence with these time windows [23]. This may not be always the case since some of the observed gamma-ray flaring episodes might have pure leptonic origin [90, 9, 145]. One example of this behavior is observed in the photon emission of the galactic black hole candidate 4U 1630-47. While a first X-ray observation is consistent with standard emission of the accretion disk a second observation performed two weeks later can be interpreted as hadronic in nature [146]. As described in section 3.3, even in the context hadronic models, neutrino flares might not have photon counterparts in the GeV-TeV range.

The Multi-flare method, described next, does not consider a-priori time coincidences with flares being observed at different wavelengths. Instead, it identifies from the data sample an overall significant deviation from the observed background by selecting promising time windows for high energy neutrino emission. This method allows large time delays between neutrino and photon flares, different flare durations for these two messengers, and neutrino flares without a photon counterparts as considered in some emission models [26, 27].

7.2 Search Algorithm for a Single Source

A graphical description of the steps taken in the Multi-flare analysis is presented in Figure 7.1. The first step consists in the construction of several time intervals with duration:

$$\Delta t_j = t_j^{\text{max}} - t_j^{\text{min}}, \tag{7.1}$$

where t_j^{min} and t_j^{max} are defined by the arrival times of two consecutive "Signal-like" events (a doublet). "Signal-like" events are defined as those events with $S_i/B_i > 1$, where S_i and B_i are the signal and background PDFs that include only space and energy information as described in sections 6.1.1 and 6.1.2. The ratio S_i/B_i is a measure of how close an event i is to the source position $\vec{x}_s$ together with a measure of its energy. For the calculation of this ratio a spectral index of $\gamma_s = 2$ is assumed for the signal energy PDF. This is the seed of the likelihood fit in which the spectral index is a free parameter allowed to vary in the range $1 - 4$. As a cross check different values of this seed ($\gamma_s = 1.5, 3$) were tested showing a negligible impact ($< 1\%$) in the best fit of the number of signal events and the signal spectral index ($\hat{n}_s$, $\hat{\gamma}_s$) for the simulated signal scenarios described in section 7.4.

Only N events within a declination band of size $\delta_s \pm 5^\circ$ around the candidate source declination δ_s (see section 6.1.2) and within a search time window of duration $\Delta T_{\text{Data}} = 80$ days, centered in the time T_m, are considered. The choice of the values for ΔT_{Data} and T_m is discussed in section 7.5.

In the second step the background and signal time PDFs are defined and a test statistic is calculated for each time window. The background time PDF is given by Eq. 6.12 and the signal time PDF is defined as a box function:

$$S^{\text{Time}}(t_i, \Delta t_j) = \frac{H(t_j^{max} - t_i)H(t_i - t_j^{min})}{\Delta t_j}, \tag{7.2}$$

where t_i is the arrival time of the event i and H is the Heaviside step function. With this definition events falling inside the time window Δt_j contribute to the signal time PDF with a factor $1/\Delta t_j$ whereas events falling outside this time window do not contribute.

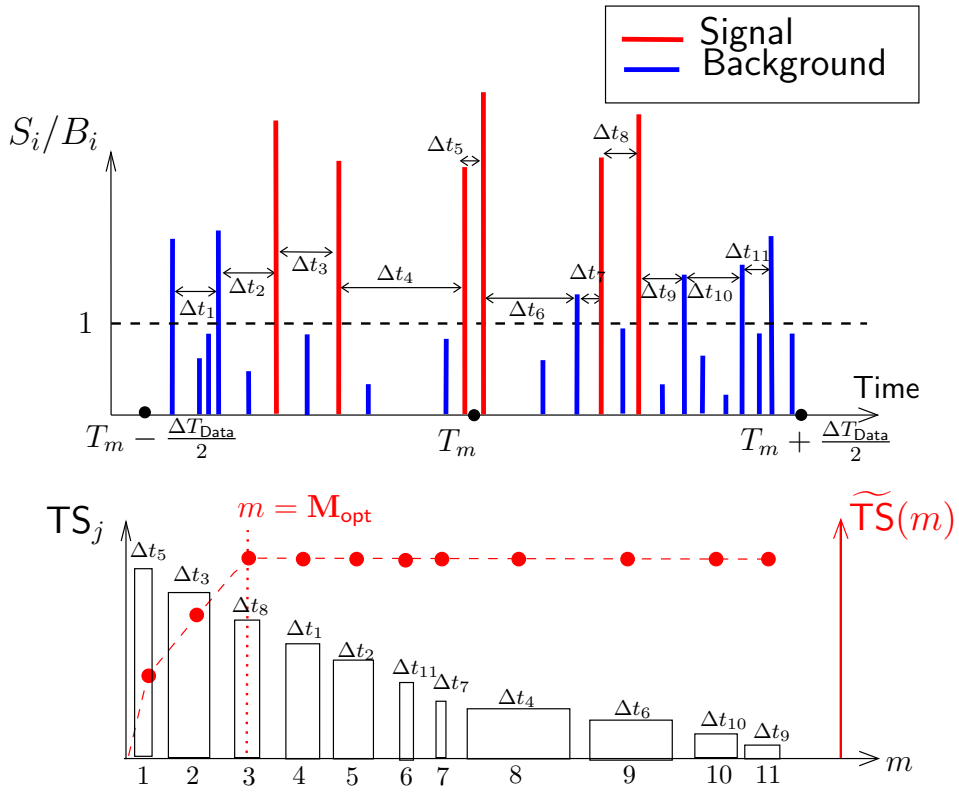

Figure 7.1: Steps in the Multi-flare analysis for an example of three signal time windows. **1.** (Top) Consecutive signal-like events $S_i/B_i > 1$ define time windows (doublets) of duration Δt_j and a signal PDF $1/\Delta t_j$ **2.** (Bottom) A test statistic TS_j is calculated for each time window and its value is used to create an ordered list of index m. **3.** A global test statistic $\widetilde{\text{TS}}(m)$ is calculated starting with the most significant time window $m = 1$ and following with the other time windows in the ordered list. **4.** The maximum of $\widetilde{\text{TS}}(m)$ is obtained for $m = M_{opt}$ time windows (in this example $M_{opt} = 3$). When the selected time windows are ordered in time, the total elapsed flaring time time $\Delta T(M_{\text{opt}})$ is defined as the time interval between the start of the first selected time window and the end of the last selected time window.

The test statistic TS_j is calculated for each time window j using in the likelihood function (Eq. 6.1) the background and signal PDFs including energy, space and time information (see Eq. 6.10 and Eq. 6.11). The test statistic is then defined as:

$$\mathrm{TS}_j = -2\log\left(\frac{\Delta T_{Data}}{\Delta t_j} \times \frac{\mathcal{L}(n_s = 0)}{\mathcal{L}(\hat{n}_s, \hat{\gamma}_s)}\right). \tag{7.3}$$

This is the test statistic described in Eq. 6.5 including an additional term $\Delta T_{Data}/\Delta t_j$. As shown in Refs. [140, 22], using a test statistic as defined in Eq. 6.5 will preferentially find short time windows, making it less powerful for time windows of durations longer than roughly one day. This is due to an effective trial factor, since many more short time windows may be found during the considered data-taking period than longer flares. The solution of this problem is to use the marginalization term $\Delta T_{Data}/\Delta t_j$ in the test statistic definition. This gives a more uniform exposure in order to be able to find flares with larger durations. In this third step the test statistic values are sorted in an ordered list with index m starting with the time widow j that gives the larger value of TS_j ($m = 1$).

In the final step the algorithm selects from the ordered list a subset of M_{opt} time windows. For this purpose a global likelihood $\mathcal{L}_{\mathrm{Global}}$ is defined using a modified signal term:

$$\mathcal{L}^{\mathrm{Global}}(n_s, \gamma_s, m) = \prod_{i=1}^{N}\left(\frac{n_s}{N} S_i^{\mathrm{Global}}(m) + \left(1 - \frac{n_s}{N}\right) B_i\right), \tag{7.4}$$

where

$$S_i^{\mathrm{Global}}(m) = \frac{\sum_{j=1}^{m} w_j \times S^{\mathrm{Space}}(\vec{x}_s, \vec{x}_i) S^{\mathrm{Energy}}(E_i, \gamma_s, \vec{x}_i) \times S^{\mathrm{Time}}(t_i, \Delta t_j)}{\sum_{j=1}^{m} w_j}. \tag{7.5}$$

The weights w_j are taken as the individual values of the test statistic TS_j (Eq. 7.3) and m is the number of time windows considered. A global test statistic is then calculated as:

$$\widetilde{\mathrm{TS}}(m) = -2\log\left[\frac{\mathcal{L}_{\mathrm{Global}}(n_s = 0)}{\mathcal{L}_{\mathrm{Global}}(\hat{n}_s, \hat{\gamma}_s, m)}\right]. \tag{7.6}$$

Starting from the time window that provided the largest value of TS_j, i.e. $m = 1$ and following with the next time windows in the ordered list, the final number of M_{opt} time windows that constitute the potential Multi-flare signal is chosen according to the maximum of $\widetilde{\mathrm{TS}}(m)$ [25].

As a result of this analysis the following parameters are extracted from a given data set:

- M_{opt}: the number of selected signal-like time windows.
- $\hat{n}_s$: the best fit of number of signal events distributed over the selected time windows.
- $\hat{\gamma}_s$: the best fit of energy spectral index.

- $\widetilde{TS}(M_{\text{opt}})$: the maximum value of the test statistic (Eq. 7.6).
- $\Delta T(M_{\text{opt}})$: the total elapsed flaring time calculated for M_{opt} time windows defined as the time between the start time of the first selected time window and the end time of the last selected time window.

The overall significance of the M_{opt} selected time windows is estimated from simulated signal and background pseudo-experiments as described in section 6.2.

7.3 Stacking of Multiple Sources

In a stacking approach several candidate sources are considered together in a single statistical test. In this way, the individual contributions of each candidate source are added up improving the discovery potential with respect to the single candidate search in the case of having several weak sources. Potential neutrino sources are grouped in categories according to their nature. As discussed in the next chapter in this thesis two categories are considered for AGNs: FSRQs and BL-Lacs (see chapter 3). The Multi-flare stacking approach described here is the time-dependent counterpart of the stacking searches performed in time-integrated analyses [13].

In a stacking analysis the signal term in the likelihood function (Eq. 7.4) is replaced by the weighted sum of the contributions of each source k:

$$S_i^{\text{Stacking}} = \frac{\sum_{k=1}^{N_s} W_k(\gamma_s, \vec{x}_k) \times S_{i,k}^{\text{Global}}(M_{\text{opt},k})}{\sum_{k=1}^{N_s} W_k(\gamma_s, \vec{x}_k)}, \tag{7.7}$$

where N_s is the number of sources in the selected category. The weight $W_k(\gamma_s, \vec{x}_k)$ correspond to the number of events expected from a source at a given location in the sky $\vec{x}_k$ following an energy distribution with a given spectral index γ_s. These weights are drawn from a 2D histogram calculated from Monte Carlo simulations. Figure 7.2 shows the distribution of these weights as function of the declination angle and the energy spectral index.

The signal PDF of each individual contribution, $S_{i,k}^{\text{Global}}(M_{\text{opt},k})$, is given by Eq. 7.5 with $M_{\text{opt},k}$ calculated by applying as a first step the Multi-flare method to each selected source k (see Figure 7.3).

Similarly to the the Multi-flare analysis described in the previous section, the energy spectral index (γ_s) and the total number of signal events (n_s) are free parameters in the likelihood maximization. In the stacking analysis, the spectral index is assumed to be the same for all the k sources in a particular category. The parameter n_s in this case accounts for the sum of signal events produced in all the sources in a given category.

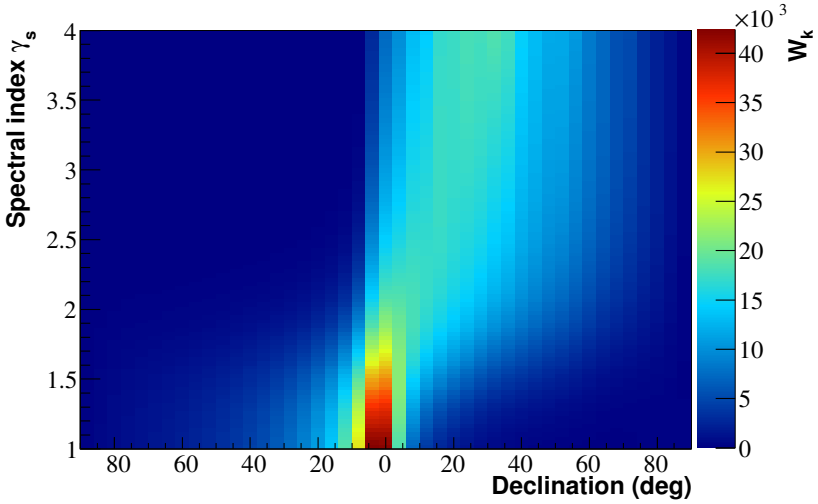

Figure 7.2: Acceptance weights $W_k(\gamma_s, \vec{x}_k)$ for the Multi-flare stacking analysis calculated from simulations.

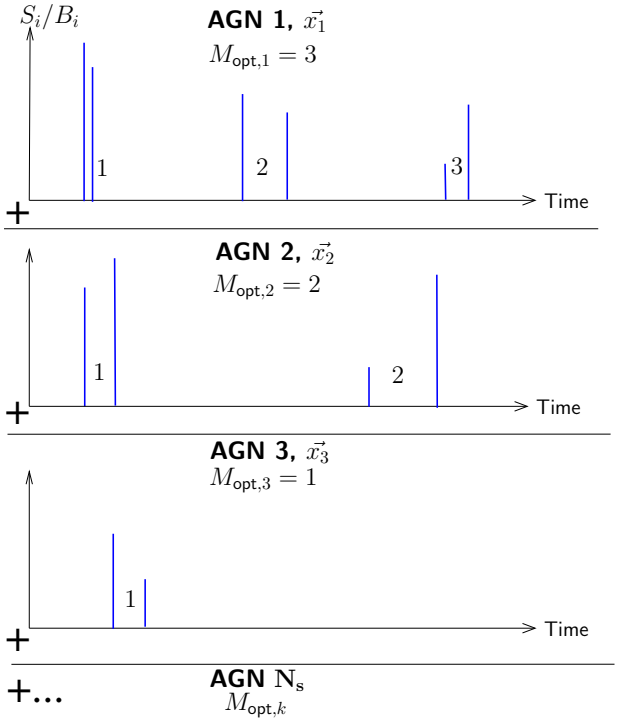

Figure 7.3: Sketch of the Multi-flare stacking approach. The contribution of several k flaring sources located at different positions in the sky is added up. Each source k contributes to the stacking likelihood according to the $M_{\text{opt},k}$ time windows selected by applying first the Multi-flare analysis for each source individually.

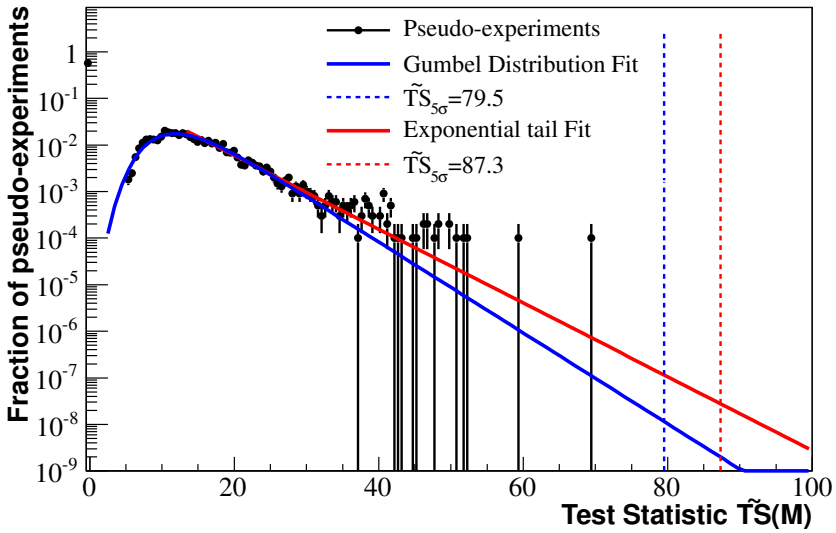

Figure 7.4: Test statistic distribution for a source at a declination 16° for 10^4 background-only pseudo-experiments. To estimate the test statistic value corresponding a a 5σ deviation two functions are used: an exponential function and a Gumbel distribution.

7.4 Simulated Flare Examples

In order to estimate the performance of the search methods described above, several sets of background-only pseudo-experiments, and signal plus background pseudo-experiments, are generated following the procedure described in section 6.2. This procedure is repeated for each one of the selected candidate sources and each one of the signal scenarios considered.

For each pseudo-experiment a test statistic value is calculated according to Eq. 7.6. An example of the resulting distribution for 10^4 background-only pseudo-experiments is shown in Figure 7.4. In order to estimate the test statistic values corresponding to a 5σ deviation $\mathrm{T}S_{5\sigma}$ (see section 6.2), two functions were fitted to the obtained distributions for each one of the candidate sources: an exponential function and a Gumbel distribution defined as [147]

$$f(x;\mu,\sigma) = A\exp\left(\frac{x-\mu}{\sigma} - \exp\left(\frac{x-\mu}{\sigma}\right)\right), \tag{7.8}$$

where the parameters μ and σ are the mode and the standard deviation respectively. The values of $\mathrm{T}S_{5\sigma}$ obtained with the two fitted functions differ in less than 10%.

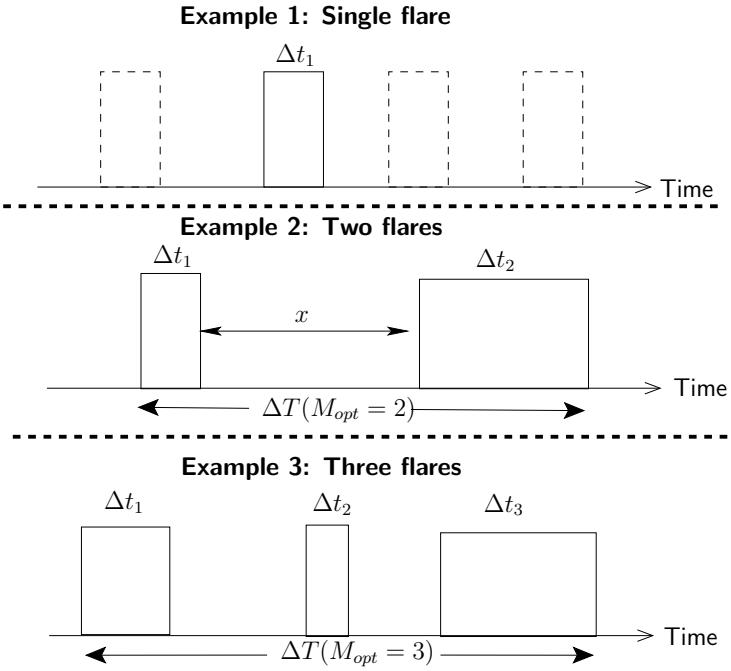

Figure 7.5: Simulated flaring scenarios: one (top), two (middle), and three flares (bottom). For the single-flare case the position in time of the signal time window is chosen randomly whereas for the other two cases the positions or the time windows are either fixed in time or their relative positions are varied to study the performance of the Multi-flare method as function of their separation time interval of duration x (sketch in the middle). A number of signal events following a Poisson distribution are injected in each time window for each simulated signal pseudo-experiment. The total elapsed flaring time $\Delta T(M_{opt})$ is defined as described in section 7.2.

7.4.1 Multiple Flares for a Single Source

Three simulated signal scenarios are considered (see Figure 7.5):

Example 1: A number of signal events (with Poisson-mean=8) are injected inside a time window of duration $\Delta t_1 = 9$ days. The starting point of this simulated flare is randomly chosen over a data taking period ΔT_{data} of 40 days. Note that this case would correspond to a rather "strong" flare since the number of events required for the discovery of a flare with this duration is larger than 7 events in case of a single-flare search [140].

Example 2: The total number of signal events (Poisson-mean=8) is the same as in Example 1, but individual events are injected over two time windows of duration $\Delta t_1 = 4$ and $\Delta t_2 = 9$ days respectively located $x = 22$ days apart. In this case, the total elapsed flaring time is $\Delta T(M_{opt} = 2) = 4 + 22 + 9 = 35$ days. The average number of injected signal events is the same for each time window (Poisson-mean=4).

Since in searches for single flares the expected discovery potential (number of events

required for a 5σ discovery) depends on the flare duration, being smaller for flares with shorter durations [22, 23, 24], this example can be interpreted as a simulated case of a "strong" flare (4 signal events in 4 days) and a "weak" flare (4 signal in events 9 days). The single-flare search method applied to this case will find only the strongest flare i.e. the first one. This is because this particular method looks only for the most significant cluster of events in time, from a given source location, neglecting other time windows.

Example 3: The total number of signal events (Poisson mean=8) is the same as in previous examples, but individual events are injected over three time windows separated in time with durations $\Delta t_1 = 4.5$ days, $\Delta t_2 = 4.5$ days and $\Delta t_3 = 9$ days, respectively ($\Delta T(M_{opt} = 3) = 28$ days). Each flare is simulated with a similar number of signal events with Poisson-mean 3, 3 and 2, respectively.

This example describes three "weak" flares. The "weak" connotation comes from a simple comparison with the discovery potential of the single-flare search [140] in which the number of events required to claim discovery at a 5σ level, for time windows with similar durations, is larger than 4 events and therefore neither of these flares would be detected with that approach[1]

Recovering the Parameters of the Simulated Flares

Example 1: one flare

Figure 7.6 shows the distribution of the output parameters, i.e. the number of signal events $\hat{n}_s$, the spectral index $\hat{\gamma}_s$, the optimal number of time windows $M_{\rm opt}$ and the flare duration ΔT as obtained for simulated background-only pseudo-experiments (A and C) and background plus signal pseudo-experiments (B and D). The background-only simulated example illustrates how signal-like flares can be mimicked with an average best fit number of signal events of around two. Figure 7.6 (B) shows that the Multi-flare method recovers in average the injected values of the spectral index ($\hat{\gamma}_s \approx 2$) and the number of injected signal events ($\hat{n}_s = 8$ events). Figure 7.6 (D) shows that the flare can be decomposed in about $M_{\rm opt} = 8$ time windows and that the flare duration is correctly estimated ($\Delta T \approx 9$ days)[2].

In Figure 7.7 (A) the correlation of the global test statistic $\widetilde{\rm TS}(M_{\rm opt})$ as a function of the number of injected signal events n_s is shown. The solid line represents a linear fit to the average values of the test statistic calculated for a fixed number of injected signal events.

[1] In this work signal events are injected according to a uniform distribution while in [140] a Gaussian distribution was considered. While a general comparison is still possible in some cases the exact numerical results are different. The definition of a flare duration, for example, is somewhat different. For a uniform distribution with non zero values in the interval Δt the standard deviation is defined according to $\sigma = \Delta t/\sqrt{12}$. Thus 4.5 and 9 days flare durations corresponds to σ about 1.3 and 2.6 days or to 0.0035 and 0.0070 years, respectively. Reference [140] simulates flares with Gaussian time structures. In this case for a flare with duration $\sigma_t = 0.0035$ (σ_t being the standard deviation of the assumed Gaussian structure) about 4 events are required for discovery.

[2] The exact duration of the flare can be slightly less since the signal events were randomly injected inside the 9 days time window.

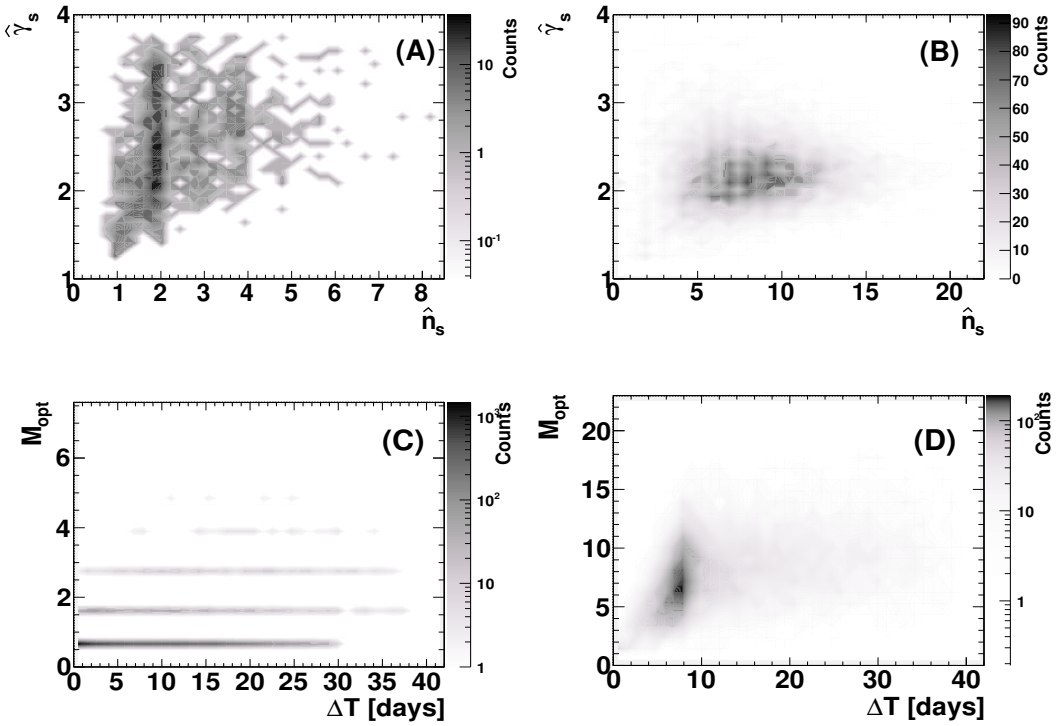

Figure 7.6: Distribution of the best fit values for the number of signal events $\hat{n}_s$ and the source spectral index $\hat{\gamma}_s$ for background-only pseudo-experiments (A) and with 8 (Poisson-mean) signal events injected on the top of the background (B) for a source at declination 15°. The optimal number of time windows $M_{\rm opt}$ as a function of the duration of the flare ΔT (i.e. the maximum time difference between any time windows yielding the best fit configuration $M_{\rm opt}$) is shown in (C) for background-only pseudo experiments and in (D) for background plus signal pseudo-experiments.

This linear relation justifies the use of the test statistic TS_j as a weight in the likelihood function (Eq. 7.4). As an additional test, the likelihood maximization was repeated with all weights fixed to one as well as to the square of the test statistic. It is found that such modifications lead to slightly worse results i.e. it was observed a 5-10% worse agreement between the injected and the estimated values of $\hat{n}_s$ and $\hat{\gamma}_s$.

In Figure 7.7 (B) the number of recovered signal events is shown as a function of the optimal number of time windows which compose the flare ($M_{\rm opt}$). The distribution shows a maximum corresponding to the number of injected signal events. The inset in Figure 7.7 (B) shows a Gaussian fit to the estimated number of signal events, $\hat{n}_s$ with a mean value of 8.2, which is good agreement with the injected value.

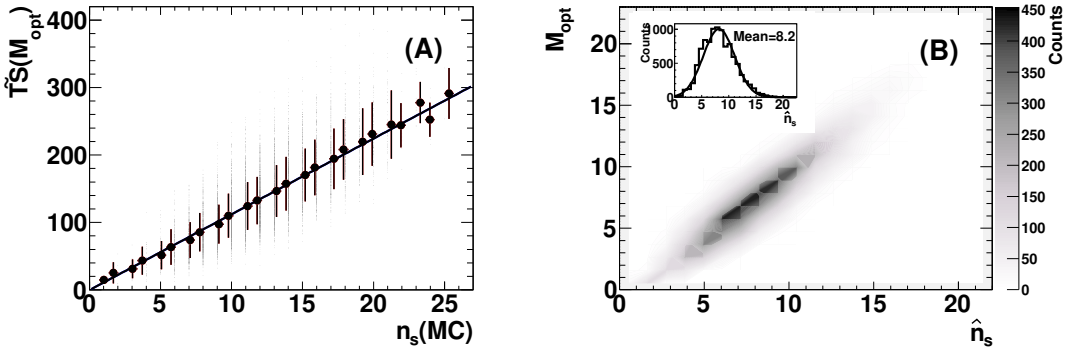

Figure 7.7: (A) Correlation of the test statistic and the number of injected signal events. The solid line represents a linear fit to data. Full circles correspond to an average value of the test statistic for a fixed number of injected signal events. (B) The optimal number of time windows which compose the flare with 9 days duration as a function of the average number of recovered signal events. The inset shows the distribution of the best fit values of the number of signal events which can be well fitted with a Gaussian.

Example 2: two flares separated in time

Figure 7.8 (A) shows the distribution of the optimal number of time windows $M_{\rm opt}$ as a function of the corresponding flare duration ΔT. In Figure 7.8 (B) the distribution of the best fit values for the spectral index $\hat{\gamma}_s$ and number of signal events $\hat{n}_s$ is shown. In this example the Multi-flare method also recovers in average the injected signal parameters. However, for this particular case, the differences between the injected and the recovered values are slightly worse than in the example 1 (about 5%). This is because for larger flare durations a larger contamination of background events is expected.

In Figure 7.8 (C) the distribution of the mean time $T_{0,j} = t_j + \Delta t_j/2$ calculated for each ($j^{\rm th}$) selected time window for each pseudo-experiment is shown. An accumulation of signal-like time windows for a time period below 5 days and between 25 and 35 days is visible, corresponding to the first and second injected flares, respectively. The Multi-flare analysis can therefore find not only the most significant flare, but also the weaker one separated in time. Such flare would not be detected by other existing methods like the single-flare search [140, 24, 23].

Information about the internal structure of the flare can be seen in test statistic distribution averaged over the 10^4 background plus signal pseudo-experiments. Figure 7.8 (D) shows changes of the average global test statistic as a function of the flare duration $\Delta T(m)$ calculated for $m < M_{\rm opt}$ time windows. The test statistic increases when more time windows are added in time, but finally reaches saturation for the time corresponding to the total elapsed flaring time considered as a signal $\Delta T(M_{opt}) = 35$ days. For the first flare (below 5 days) and second flare (from 25 to 35 days) the increment of the average global test statistic as a function of time is much larger than during the period corresponding to

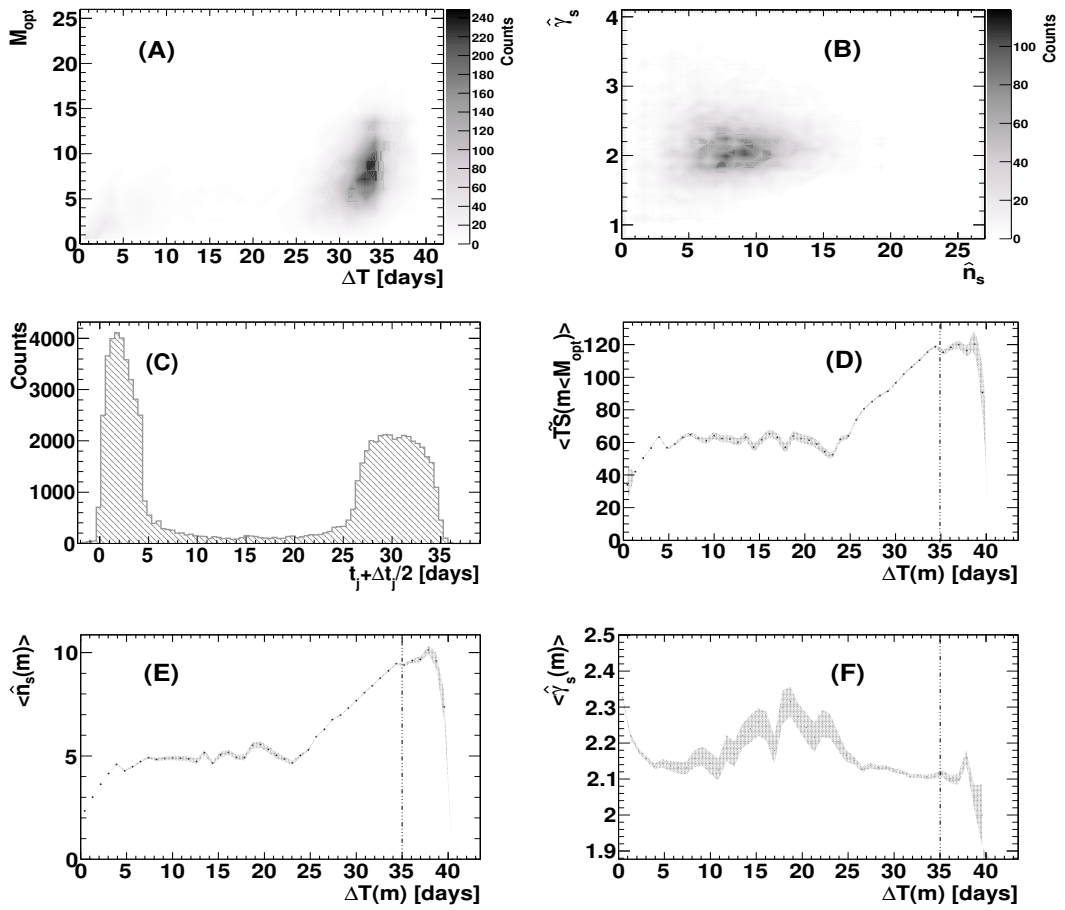

Figure 7.8: Results for the search of two individual flares separated in time (Example 2). (A) Distribution of the optimal number of time windows ($M_{\rm opt}$) as a function of the total flare duration ΔT; (B) Distribution of the best fit values for the spectral index and the number of signal events; (C) Distribution of the mean time of the time windows selected for each pseudo-experiment; (D), (E), and (F): The distributions of $\left\langle \widetilde{\rm TS}(m) \right\rangle$, $\langle \hat{n}_s(m) \rangle$ and $\langle \hat{\gamma}_s(m) \rangle$ as a function of the flare duration $\Delta T(m)$. The vertical dashed line indicates the total elapsed flaring time ($\Delta T(M_{\rm opt}) = 35$ days)

the 22 days time gap. During this last period variations can also be observed, which is an indication for background fluctuations. A similar behavior is shown in Figure 7.8 (E) for the average number of signal events $\langle \hat{n}_s(m) \rangle$ as a function of the flare duration[3].

For completeness, Figure 7.8 (F) shows the average spectral index $\langle \hat{\gamma}_s(m) \rangle$ as a function of the flare duration. The average best fit spectral index is about 2.2 and differs by about 8.5% from the injected value ($\gamma_s = 2$). Similarly to the previous distributions, the fluctu-

[3]Note that both distributions presented in Figure 7.8 (D) and (E) are averaged over 10^4 pseudo-experiments.

ations of the spectral index are strongly reduced during the periods corresponding to the injected signal. The effect is particularly visible for the second flare, between 25 days up to 35 days. The Multi-flare method can therefore recover the injected parameters describing the flares in this example too providing additional information about the time development even when each flare alone are below the threshold for detection using a single-flare search.

Example 3: three weak flares separated in time

In this case three individual weak flares were simulated. Each flare would not be individually detected at a 5σ level by using the single-flare search method. In principle, if all events are injected into a single flare of duration about 28 days ($\sigma_t \simeq 0.02$ year) the single-flare search would yield a discovery [140]. For a flare of such duration, more than about 7 events are needed for discovery at a 5σ level using the method labeled by Assumed Burst Time (Energy) in Figure 4 of Ref. [140]. However, the flare will be found only if these 7 events will form *one cluster of events compact in time*. This is because the single-flare search only looks for for a maximum test statistic that corresponds to the most significant flare (cluster of events following a Gaussian distribution in time) from a point source. This is certainly not the case for this example, where 8 events are distributed among three individual and well separated flares.

Figures 7.9 (A) and (B) show that also in this case the method can recover the injected values of the spectral index, the mean number of injected signal events and the total flare duration (28 days). In addition, the overall signal injection can be decomposed into about 8 time windows. Sorting these time windows in time the distribution of individual flares is recovered as shown in Figure 7.9 (C). Three flares can be clearly distinguished, with a duration of about 5 days, 5 days and 10 days, respectively. The average value of the test statistic and the number of signal events is presented in Figure 7.9 (D) and (E). Due to a smaller time gap between individual flares, a factor 4 smaller than for the flares studied in the Example 2, the structures are less pronounced. Note that the distributions presented in Figure 7.9 (D) and (E) start to saturate at a point corresponding to the total elapsed flaring time injected (above 28 days).

Finally, in Figure 7.9 (F) the average spectral index $\langle\hat{\gamma}_s(m)\rangle$ as a function of time is shown. The source spectral index has a value of about 2.2 and differs by about 10% from the true value ($\gamma_s = 2$). Fluctuations of the spectral index also increase for times greater than the total flare duration (above 28 days). This example demonstrates that the Multi-flare method can find weak flares separated in time,

7.4.2 Performance of the Method

Figure 7.10 shows the performance of the Multi-flare method in terms of number of events needed for discovery (or discovery potential as described in section 6.2) for a source at declination $\delta_s = 22^\circ$ as a function of the flare duration for two simulated cases: one and two flares.

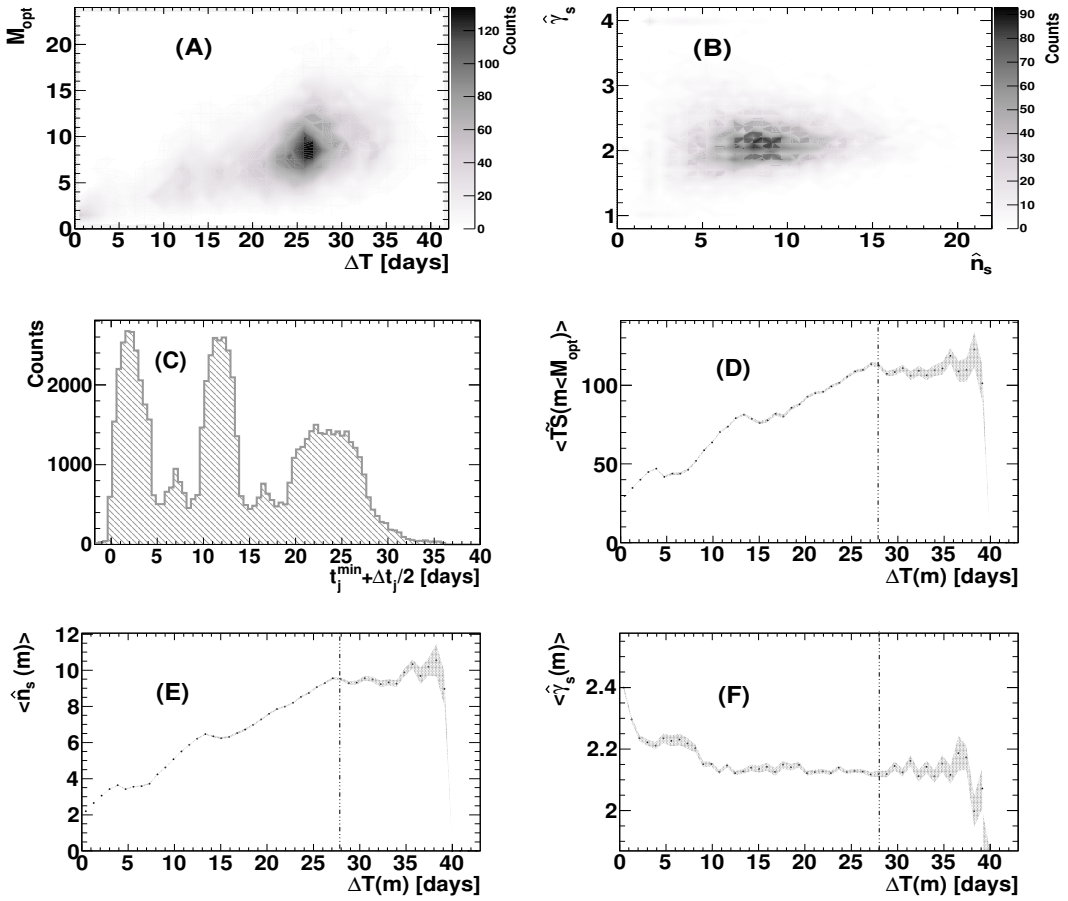

Figure 7.9: Example 3: Results of the search for three individual flares separated in time. (A) Distribution of the optimal number of time windows ($M_{\rm opt}$) as a function of the total flare duration ΔT; (B) Distribution of the best fit values for the spectral index and the number of signal events; (C) Distribution of the mean time of the time windows selected for each pseudo-experiment; (D), (E), and (F): The distributions of $\left\langle \widetilde{\rm TS}(m) \right\rangle$, $\langle \hat{n}_s(m) \rangle$ and $\langle \hat{\gamma}_s(m) \rangle$, respectively. The vertical dashed line indicates the overall period of total elapsed flaring time injected (28 days).

For a single flare the average number of events needed for discovery increases for larger flare durations (black curve). This is because for large flare durations the time term in the signal PDF becomes weaker than the energy and space terms. Since the overall background level decreases when short time windows are considered, the discovery potential is expected to become better for short flares as noted also in the single flare search [140]. For long enough flares the search method loses its power and the discovery potential becomes comparable and larger than the obtained with a time integrated analysis, i.e using only the energy and space terms, represented by the horizontal dashed line at around 14 events.

For comparison, the performance of a single-flare search (see section 6.4) is also shown

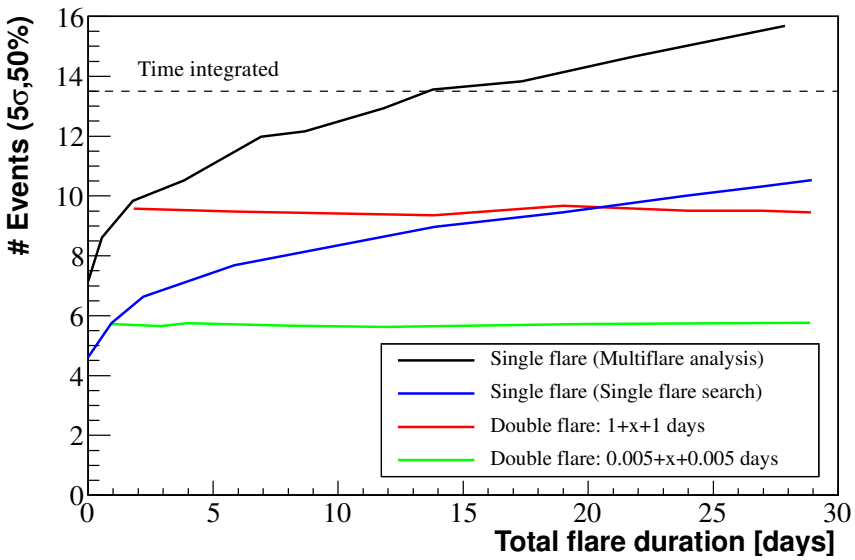

Figure 7.10: Discovery potential for two simulated flare examples: one and two flares. In the case of one flare (black and blue curves) its duration is defined by the duration of the time window chosen. For the examples of two flares separated a distance x (red and green curves), the duration correspond to the total elapsed flaring time time i.e the sum of the individual durations and the separation x (see Figure 7.5).

(blue curve). In the case of one simulated flare the single-flare search performs always better than the Multi-flare method. This is expected since the Multi-flare search method considers more independent time windows and the chance to pick up a background fluctuation increases.

For the case of two flares separated in time, Figure 7.10 shows one feature characteristic of the Multi-flare method developed in this thesis: its performance does not depend on the time separation x in between the individual flares (red and green horizontal lines). The number of events for discovery in this cases is equal the one obtained when the two flares are not separated in time ($x = 0$) i.e at the point in which the black and horizontal curves meet. This feature arises due to the fact that the selection of the M_{opt} signal-like time windows is performed in the test statistic domain (see step 3 in Figure 7.1) regardless of the overall time structure. For large time separations between individual flares the single-flare search loses power since it assumes a Gaussian time dependence.

As in the single flare case, the discovery potential decreases with the duration of the individual time windows as expected. This is shown when comparing the discovery potential obtained for a double flare with individual flare durations of 1 day and double flare with individual flare durations of 0.005 days.

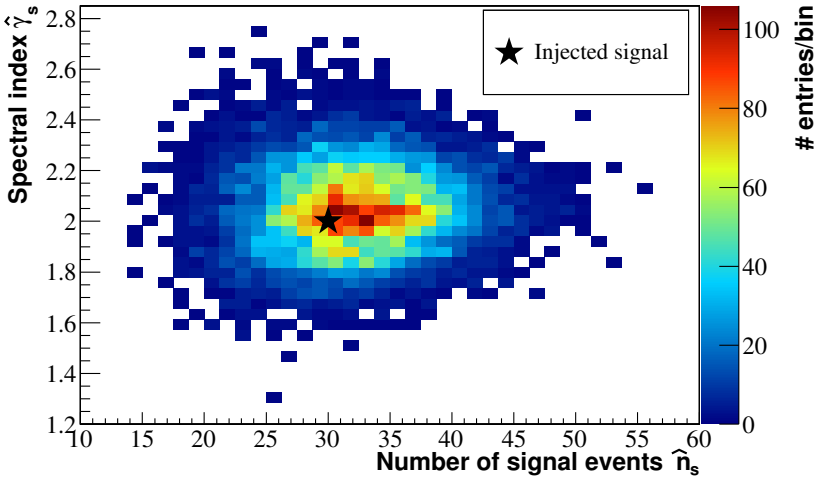

Figure 7.11: Best fit parameters of the number of signal events $\hat{n}_s$ and energy spectral index $\hat{\gamma}_s$ for a set of 10^5 background plus signal pseudo-experiments in the stacking analysis for 5 sources.

7.4.3 Multiple Flares for Multiple Sources

In order to study the performance of the stacking approach several flaring sources at different locations in the sky are considered. Signal events for each source are simulated as a double-flare structure: two flares of duration $\Delta t_1 = \Delta t_2 = 1$ days with different separation in time x (see Figure 7.5 (middle)). The signal events are injected in each location following a Poisson distribution with mean 6 (30 total events for 5 sources) and an E^{-2} energy spectrum for a total of 10^4 pseudo-experiments for each signal scenario. Figure 7.11 shows the resulting best fit parameters. The centroid of this 2D distribution is located approximately in $\hat{n}_s = 30$ and $\hat{\gamma}_s = 2$ showing that the Multi-flare stacking analysis is able to recover on average the parameters of the injected signal.

The discovery potential for the stacking case and for a single source in this simulated example is shown in Figure 7.12 . Assuming that each source contributes with the same number of signal events, the discovery potential per source is calculated as the number obtained for the stacking case divided by the number of sources that are stacked. Figure 7.12 shows that with this definition, each considered source in the stacking approach is required to contribute in average with a factor of ~ 2 less number of events to reach the 5σ threshold than if analyzed separately.

Figure 7.13 shows the discovery potential per source as a function of the total number of stacked sources for different simulated total elapsed flaring times. Adding sources improves the discovery potential per source as expected in a stacking analysis. The discovery potential for different values of the total elapsed flaring time is constant as discussed in the previous section.

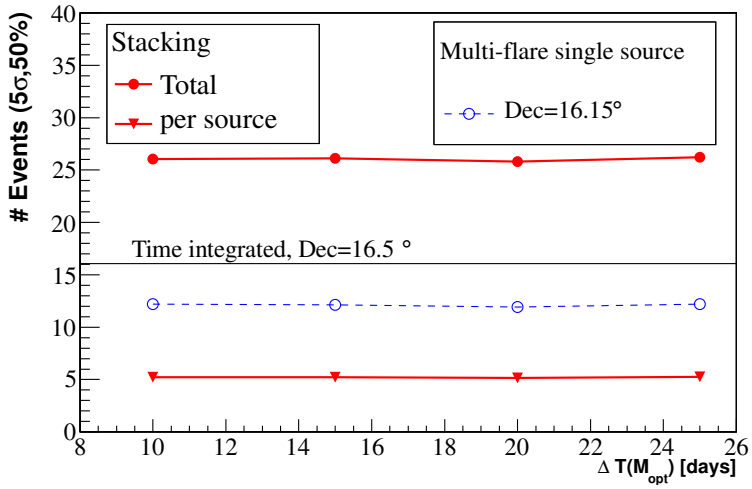

Figure 7.12: Discovery potential as a function of the simulated total elapsed flaring time, $\Delta T(M_{\text{opt}})$, for the double-flare example (see Example 2 in Figure 7.5) stacking five sources. The dashed blue points correspond to the discovery potential obtained for a single source. The lines corresponding to the other sources have similar values and are omitted. The solid lines correspond to the stacking case: total (filled red circles) and per source (filled red triangles). For this example the data sample 2010-2011 is used (see chapter 5).

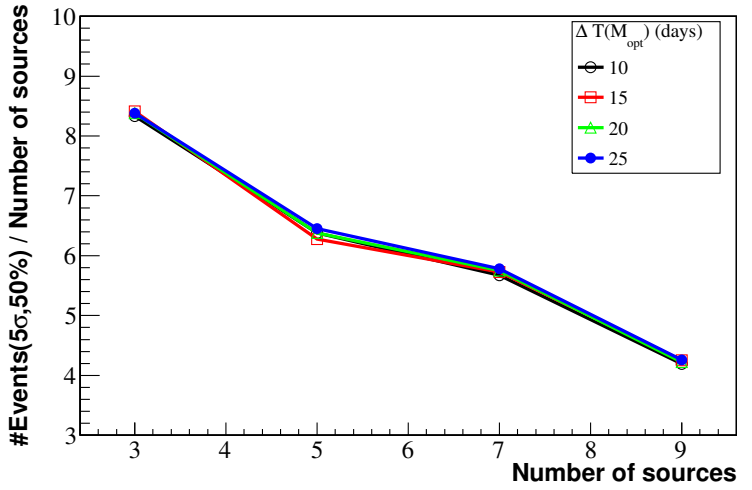

Figure 7.13: Discovery potential per source (total divided by the number of contributing sources) as a function of the number of stacked sources for different injected total elapsed flaring times. In this example two flares of 4 days duration are injected i.e $\Delta T(M_{\text{opt}}) = 4 + x + 4$.

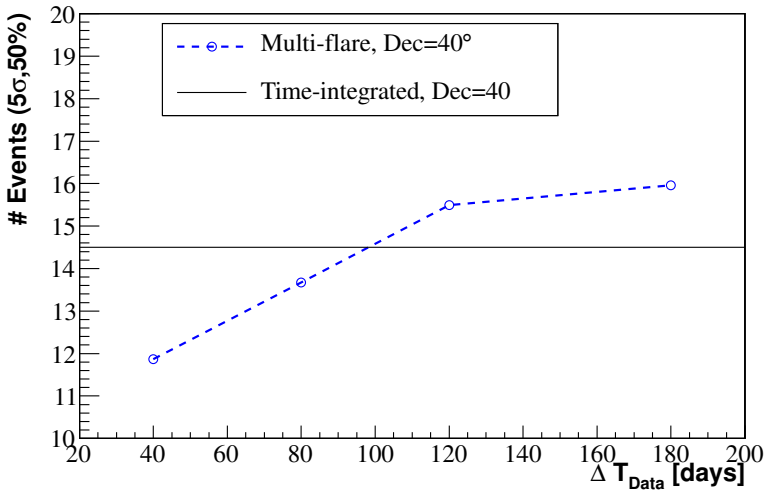

Figure 7.14: Discovery potential of the Multi-flare and time-integrated analyses as a function of the time search window ΔT_{Data}. In this example two flares of duration 4 days separated 10 days are simulated for a source at declination angle $= 40°$. The discovered potential for the Multi-flare analysis in this simulated example is slightly better than the time-integrated line only for values of $\Delta T_{\text{Data}} \lesssim 100$ days. A value of $\Delta T_{\text{Data}} = 80$ days is chosen for the 2009-2010 and 2010-2011 data sets used.

7.5 Discussion

Initial tests showed that the performance of the Multi-flare method gets worse with the amount of data used. Figure 7.14 shows the discovery potential calculated for a simulated example of two flares of duration 4 days separated by 10 days as function of the duration of the search time window ΔT_{Data}. The discovery potential get worse for large durations of the time search window because the number of background fluctuations mimicking a signal increases. The search time window was therefore restricted to $\Delta T_{\text{Data}} = 80$ days. This value was chosen as a compromise of improving the discovery potential with respect to the time integrated search, for the benchmark scenario of two flares separated in time, at expense of decreasing the elapsed time in which multiple neutrino flares are looked for. The center of the 80 days time search window T_m (see Figure 7.1) for the analysis of 2009-2010 and 2010-2011 data sets, was chosen according to photon flare alerts reported for each selected source as described in section 3.4.

For the analysis using of the 2011-2012 data set an improvement on the performance of the Multi-flare analysis was achieved by imposing a stronger cut on the S_i/B_i ratio used to select the initial "signal-like" events (See Figure 7.1). By choosing a stronger cut in this ratio the background level[4] decreases allowing to test larger time search windows with a

[4] The background here is defined as the number of short (less than one day) time windows found in

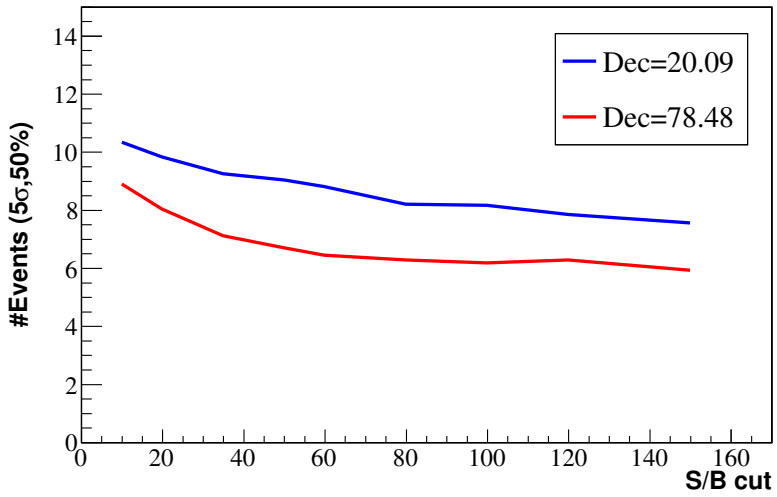

Figure 7.15: Discovery potential of the Multi-flare analysis for two declinations corresponding to two of the selected AGNs, as function of the S_i/B_i ratio cut. For this test the entire data-set available for the 2011-2012 season is used. A value of $S_i/B_i = 100$ is chosen for the analysis.

discovery potential below the obtained with a time-integrated analysis.

The discovery potential for the benchmark scenario of two flares separated in time was calculated for different values of the S_i/B_i cut and different declinations corresponding to the position of a sub-set of the selected AGNs (see section 3.4) as shown in Figure 7.15. These simulations were generated without imposing the restriction on the time search time window i.e using a whole year of data-taking. A value of $S_i/B_i > 100$ is chosen since the discovery potential does not change significantly ($\lesssim 1\%$) above this value. As a result of this improvement, the Multi-flare method became sensitive to multiple flares distributed over a complete year of data, without the need of defining an specific time search window based on photon observations, as was done in the analysis of the 2009-2010 and 2010-2011 data-sets.

A further improvement, not implemented in the final analysis described in this thesis, could be achieved by defining the initial signal-like time windows with larger multiplicities, for example using consecutive quadruplets instead of consecutive doublets. Background fluctuations with larger event multiplicities are less probable, so stacking quadruplets instead of doublets could result in a lower threshold for discovery and in principle larger search time windows (larger than a year) could be used.

background-only pseudo-experiments.

Chapter 8

Results

The Multi-flare method was applied to 3 different data-sets of IceCube operation corresponding to the seasons 2009-2010 (IC59), 2010-2011 (IC79) and 2011-2012 (IC86-I). A new set of flaring AGNs to be tested with this method was selected for each season following the criteria described in section 3.4. The analysis of the data corresponding to the 2009-2010 and 2010-2011 seasons were performed with the restriction on the duration of time search window, set at 80 days. For the analysis of the 2011-2012 data set this restriction was avoided as described in section 7.5 allowing to search of multiple neutrino flares over the entire year of data taking from the selected sources. The Multi-flare stacking method was applied to two data-sets corresponding to the 2010-2011 and 2011-2012 seasons.

8.1 Results for Single Sources

No significant time windows indicating multiple neutrino flares from astrophysical origin were found in the direction of the selected sources. Tables 8.1, 8.2, 8.3 and 8.4 show the parameters obtained for each data-set and for each source i.e:

- Pre-trial p-value.
- $\hat{n}_s$: Best fit of the number of signal events.
- $\hat{\gamma}_s$: Best fit of the power law spectral index.
- $\Delta T(M_{\text{opt}})$: Flare activity time.
- Fluence upper limit (u.l.)

The sources that resulted in the lowest p-value are highlighted in gray. These sources are 3C 454.3 with a pre-trial p-value of 0.08 (83% post-trial) for the 2009-2010 season, PKS 1830-211 with a pre-trial p-value of 0.13 (96% post-trial) for the 2010-2011 season and FSRQ PKS 2142-75 with a pre-trial p-value of 0.03 (70% post-trial) for the 2011-2011

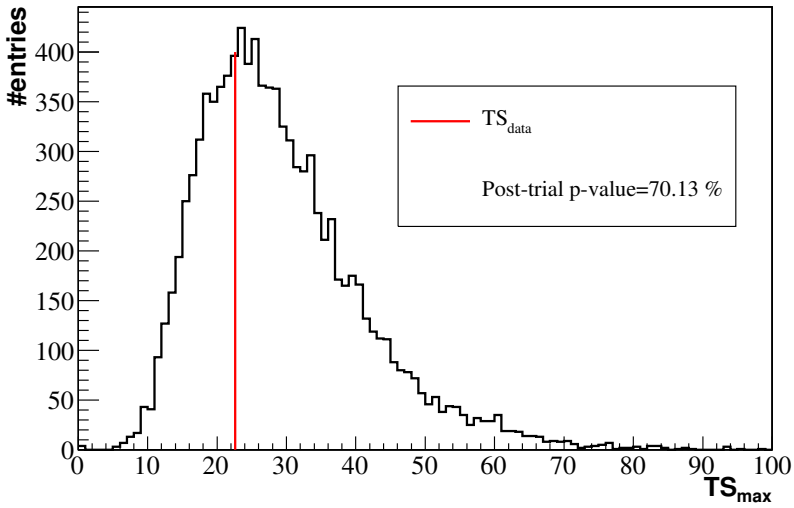

Figure 8.1: Distribution of the maximum test statistic TS_{max} obtained for 10^4 background-only pseudo-experiments simulated for each one of the 38 AGN locations tested for the 2011-2012 season (IC86-I). The red line marks the test statistic value obtained with real data for the source with the lowest pre-trial p-value of 0.03 (FSRQ PKS 2142-75). The post-trial p-value is calculated as the fraction of pseudo-experiments above this line which for this case is $\sim 70\%$.

season. It is interesting to note that the FSRQ PKS 2142-75, with the lowest pre-trial p-value obtained for the three data-sets and selected sources, was also the source with the lowest p-value in a triggered analysis that builds the time PDF on base of Fermi-LAT light curves [23].

As an example of the procedure to calculate the post-trial p-value, Figure 8.1 shows the distribution of maximum values of the test statistic (Eq. 7.6) obtained for 10^4 background-only pseudo-experiments for each one of the 38 sources selected for the 2011-2012 season. From this distribution the post-trial p-value is calculated as the fraction of pseudo-experiments with a test statistic larger or equal to the obtained in data.

Since the obtained p-values indicate compatibility with the background-only hypothesis upper limits are calculated as described in section 6.2 in terms of fluences (see section 6.4.1). The time interval to calculate this fluence is taken as the flare activity time $\Delta T(M_{\text{opt}})$ found for each source. As a convention within the IceCube Collaboration, if $\hat{n}_s = 0$ then no p-value or $\hat{\gamma}_s$ are reported and the upper limit matches the sensitivity [13, 14, 15]. As a comparison, the fluence sensitivities obtained in the simulation of a single flare with different durations (0.1 and 30 days) are shown in Figure 8.2 (Top) together with the the fluence upper limits obtained for the 2011-2012 season as function of the declination of the selected AGNs. As expected the fluence sensitivity and upper limits improve for shorter durations.

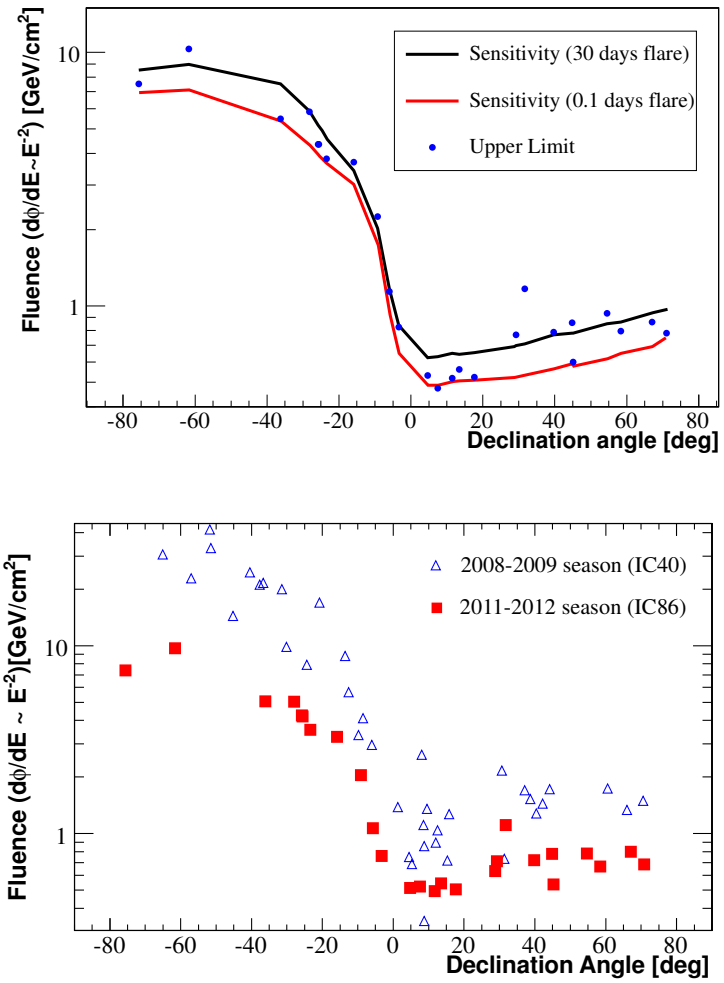

Figure 8.2: Top: Fluence upper limits for the selected AGNs in the 2011-2012 season and sensitivities for a single flare simulated for two durations: 0.5 and 30 days. Bottom: For comparison the fluence upper limits obtained with single-flare search method [22] applied to IceCube data taken in the 2008-2009 season are also shown.

Figure 8.2 (Bottom) shows the fluence upper limits for the season 2011-2012 together with the fluence upper limits obtained in Ref. [22] in which a single flare search was performed for selected sources using data of the incomplete detector taken in the season 2008-2009 (IC40). The fluence upper limits obtained in this thesis for the season 2011-2012 are on average a factor of 2 lower. Each IceCube data taking season brought improvements in the event selection techniques and in the angular resolution that resulted in lower upper limits as observed also in time-integrated analysis [13, 14, 15].

Source	Type	RA °)	DEC°)	Atel ID/Ref	T_m (MJD)	p-value	$\hat{n}_s$	$\hat{\gamma}_s$	$\Delta T(M_{\text{opt}})$ (days)	Fluence u.l. (GeV/cm^2)
PKS 0235+164	BL-Lac	39.67	16.62	2207	55085	0.27	1.98	1.89	0.006	0.54
Mkn 421	BL-Lac	166.12	38.21	2368	55200	-	0	-	4.11	0.9
Mkn 421	BL-Lac	166.12	38.21	2443	55255	0.34	1.94	3.95	0.134	0.73
PKS 0426-380	BL-Lac	67.16	-37.94	2366	55198	-	0	-	14.41	14.3
PKS 0537-441	BL-Lac	84.72	-44.08	2124	55020	0.45	1.83	3.95	7.21	15.7
PKS 0537-441	BL-Lac	84.72	-44.08	2454	55247	-	0	-	25.68	17.44
PKS 0537-441	BL-Lac	84.72	-44.08	2591	55313	-	0	-	1.18	15.2
S5 0716+714	BL-Lac	110.48	71.34	2353	55176	0.34	1.83	3.95	3.9	1.3
PKS 0447-439	BL-Lac	72.38	-43.84	2350	55180	-	0	-	4.8	15.5
PKS 1424+240	BL-Lac	216.75	23.8	2098	54977	-	0	-	0.44	0.59
PKS 0301-243	BL-Lac	45.89	-24.11	2610	55319	0.36	1.91	3.13	0.775	7.37
3C 454.3	FSRQ	343.49	16.15	2534	55289	-	0	-	1.84	0.64
3C 454.3	FSRQ	343.49	16.15	2329	55167	0.22	2.17	3.71	0.045	0.52
3C 454.3	FSRQ	343.49	16.15	2200	55089	0.08	5.3	2.4	28.67	0.86
3C 279	FSRQ	194.05	-5.79	2154	55044	-	0	-	1.1	1.4
PKS 2023-07	FSRQ	306.42	-7.6	2175	55066	-	0	-	0.81	1.8
3C 273	FSRQ	187.28	2.05	2200	55089	-	0	-	0.365	0.71
3C 273	FSRQ	187.28	2.05	2376	55203	-	0	-	1.28	0.81
4C +31.03	FSRQ	18.23	32.12	2054	54971	-	0	-	1.43	0.68
PKS 0805-07	FSRQ	122.05	-7.84	2136	55034	-	0	-	3.85	2.03
PKS 0805-07	FSRQ	122.05	-7.84	2048	54958	-	0	-	10.34	1.91
PKS 0402-362	FSRQ	60.98	-36.06	2484	55228	-	0	-	13.17	12.88
B2 1520+31	FSRQ	230.55	31.73	2026	54941	-	0	-	4.85	0.65
OX 169 325.87	FSRQ	325.87	17.72	2393	55214	-	0	-	1.54	0.64
PKS 2052-47	FSRQ	314.09	-47.24	2160	55052	-	0	-	0.62	15.36

Table 8.1: Results for the selected variable AGNs using the Multi-flare analysis and data from the 2009-2010 season (**IC59**). All the p-values are pre-trial (see text). If $\hat{n}_s = 0$ then no p-value or $\hat{\gamma}_s$ are reported. The gray column indicates the source with the lowest p-value obtained among the other sources in the list

Source	Type	RA (°)	DEC (°)	Atel ID/Ref	T_m (MJD)	p-value	$\hat{n}_s$	$\hat{\gamma}_s$	$\Delta T(M_{\text{opt}})$ (days)	Fluence u.l. (GeV/cm^2)
PKS 2326-502	FSRQ	352.31	-49.93	2783,3008	55415	-	0.0	-	15.97	12.15
PKS B1414-418	FSRQ	217.01	-42.10	3329,3337	55686	-	0.0	-	0.86	9.42
PKS 1830-211	FSRQ	278.41	-21.075	2943	55485	-	0.0	-	0.25	4.53
PKS 1830-211	FSRQ	278.41	-21.075	2950	55560	0.13	2.6	3.9	0.09	4.54
PKS 0727-11	FSRQ	112.57	-11.69	2895,2901	55460	-	0.0	-	6.409	2.38
PKS 1510-08	FSRQ	228.20	-9.10	3194,2385	55616	0.29	2.3	2.3	2.53	1.63
3C 279	FSRQ	194.04	-5.79	2886	55467	0.45	1.9	2.2	0.59	0.96
PKS 1329-049	FSRQ	203.01	-5.13	2728,2739	55384	-	0.0	-	8.33	1.04
PKS 1329-049	FSRQ	203.01	-5.13	2837	55450	-	0.0	-	0.19	0.84
3C 454.3	FSRQ	343.49	16.15	3064,3055	55520	-	0.0	-	0.10	0.49
4C+21.35	FSRQ	186.22	21.38	2684,2686	55364	-	0.0	-	7.44	0.59
Ton 599	FSRQ	179.87	29.24	2795	55423	-	0.0	-	0.67	0.56
B2 1520+31	FSRQ	230.54	31.74	3050	55519	0.39	1.8	2.0	0.41	0.57
4C +38.41	FSRQ	248.80	38.17	3238	55635	-	0.0	-	9.52	0.71
4C +38.41	FSRQ	248.80	38.17	3333	55689	-	0.0	-	1.37	0.61
PKS 2155-304	BL-Lac	329.71	-30.21	2944	55482	-	0.0	-	13.87	7.86
PKS 2155-304	BL-Lac	329.71	-30.21	2947	55600	-	0.0	-	13.85	7.82
PKS 0019+058	BL-Lac	5.64	6.12	2800	55387	0.40	1.6	2.2	0.43	0.66
MG1 J021114+1051	BL-Lac	32.80	10.83	3120,3129	55584	0.34	2.0	2.6	0.199	0.50
B2 2234+28A	BL-Lac	339.10	28.47	3056	55526	-	0.0	-	0.13	0.53
1ES 1215+303	BL-Lac	184.46	30.10	3100	55563	-	0.0	-	0.12	0.55
3C 66A	BL-Lac	35.66	43.036	3003	55503	-	0.0	-	0.15	0.62
MAGIC J2001+435	BL-Lac	300.28	43.87	2753	55393	-	0.0	-	0.37	0.63
5S5 1803+784	BL-Lac	270.14	78.48	3322,3323	55683	-	0.0	-	3.79	0.83

Table 8.2: Results for the selected variable AGNs using the Multi-flare analysis and data from the 2010-2011 season (**IC79**). All the p-values are pre-trial (see text). If $\hat{n}_s = 0$ then no p-value or $\hat{\gamma}_s$ are reported. The gray column indicates the source with the lowest p-value obtained among the other sources in the list.

Source	Type	ra (°)	dec (°)	Atel ID/Ref	T_m (MJD)	p-value	$\hat{n}_s$	$\hat{\gamma}_s$	$\Delta T(M_{\text{opt}})$ (days)	Fluence u.l. (GeV/cm^2)
4C +71.07	FSRQs	130.41	70.88	3831	-	0.33	4.87	2.57	43.28	0.68
S4 1849+67	FSRQs	282.35	67.10	3478	-	-	0	-	81.05	0.80
TXS 0059+581	FSRQs	15.68	58.46	3864	-	-	0	-	12.55	0.66
GB6 J0742+5444	FSRQs	115.65	54.71	3445	-	-	0	-	77.89	0.78
B3 0650+453	FSRQs	103.56	45.24	3580	-	0.38	4.01	3.95	15.45	0.53
B3 1343+451	FSRQs	206.37	44.89	3793	-	-	0	-	65.20	0.77
3C 345	FSRQs	250.75	39.83	[23]	-	0.13	3.23	2.39	5.07	0.72
B2 1520+31	FSRQs	230.54	31.74	[23]	-	0.04	4.06	2.38	43.76	1.10
Ton 599	FSRQs	179.88	29.25	[23]	-	-	0	-	144.76	0.71
4C +28.07	FSRQs	39.47	28.77	3670	-	-	0	-	14.62	0.63
OX 169	FSRQs	325.88	17.72	[23]	-	-	0	0	0.95	0.50
PKS 0528+134	FSRQs	82.71	13.55	3412, 3422	-	-	0	0	3.14	0.54
CTA 102	FSRQs	338.12	11.72	[23]	-	0.28	1.93	2.83	0.72	0.49

Table 8.3: Results for the selected variable AGNs using the Multi-flare analysis and data from the 2011-2012 season (**IC86-I** Part I). All the p-values are pre-trial (see text). If $\hat{n}_s = 0$ then no p-value or $\hat{\gamma}_s$ are reported.

Source	Type	ra (°)	dec (°)	Atel ID/Ref	T_m (MJD)	p-value	$\hat{n}_s$	$\hat{\gamma}_s$	$\Delta T(M_{\text{opt}})$ (days)	Fluence u.l. (GeV/cm^2)
OG 050	FSRQs	83.18	7.55	3750,3773	-	0.16	1.99	2.46	0.05	0.52
MG1 J123931+0443	FSRQs	189.88	4.73	3445	-	-	0	0	1.86	0.51
PKS 2320-035	FSRQs	50.91	-3.28	[23]	-	-	0	0	22.51	0.76
3C 279	FSRQs	194.04	-5.79	[23]	-	-	0	0	22.10	1.06
PKS 1510-08	FSRQs	228.20	-9.10	3470, 3473	-	0.07	3.61	3.07	14.81	2.04
PMN J2345-1555	FSRQs	356.27	-15.89	[23]	-	-	0	0	106.69	3.27
PKS 0454-234	FSRQs	74.26	-23.42	3703, 3713	-	0.29	1.96	1.74	0.73	3.56
PKS 1622-253	FSRQs	246.42	-25.44	3424	-	-	0	0	6.98	4.19
PKS 1244-255	FSRQs	191.68	-25.78	[23]	-	-	0	0	6.98	4.25
PKS 2255-282	FSRQs	344.50	-27.99	3948	-	-	0	0	17.18	5.03
PKS 0402-362	FSRQs	60.98	-36.06	3655, 3660	-	0.325	2.86	2.3	0.66	5.05
PKS 0235-618	FSRQs	39.29	-61.62	[23]	-	-	0	0	136.43	9.68
PKS 2142-75	FSRQs	326.87	-75.58	[23]	-	0.03	1.99	2.6	0.17	7.39

Table 8.4: Results for the selected variable AGNs using the Multi-flare analysis and data from the 2011-2012 season (**IC86-I** Part II.). All the p-values are pre-trial (see text). If $\hat{n}_s = 0$ then no p-value or $\hat{\gamma}_s$ are reported. The gray column indicates the source with the lowest p-value obtained among the other sources in the list.

IceCube Season	AGN Category	Number of sources	Hemisphere	p-value (post-trial)	$\hat{n}_s$	$\hat{\gamma}_s$	Fluence u.l. (GeV/cm^2)
2010-2011	FSRQs	7	South	0.16	7.4	3.6	1.00
	FSRQs	5	North	0.98	1.5	1.9	0.15
	BL-Lac	6	North	0.91	3.7	2.4	0.24
2011-2012	FSRQs	11	South	0.47	11.8	2.5	0.91
	FSRQs	15	North	0.62	9.0	2.4	0.12
	BL-Lac	9	North	0.91	3.8	2.3	0.19

Table 8.5: Results of the Multi-flare stacking searches

8.2 Results for Stacking Multiple Sources

For the stacking analysis the selected AGNs were grouped in categories. As described in chapter 3 there are different predictions in terms of neutrino production for two AGN classes: BL-Lacs and FSRQs. In order to test these predictions independently the selected AGNs were first grouped according to these classes.

Due to earth absorption and the event selection of high energy down-going events to reduce the atmospheric muon background (see section 5.3 and Ref. [139]), the energy range accessible to IceCube depends on the zenith angle of the events. While TeV neutrino energies are accessible for the northern sky (Declination angle > 0), PeV and EeV energies are accessible close and above the horizon (Declination angle < 0). In order to explore the same energy range in the stacking analysis the selected sources were also grouped according to their location in the sky (south and north).

The results for the Multi-flare stacking search applied to the selected categories are shown in Table 8.5. Given the post-trial p-values of these observations the results are compatible with the background-only hypothesis. The category with the lowest post-trial p-value for both data-sets considered are the FSRQs located in the southern hemisphere.

The fluence upper limits for the stacking analysis shown in Table 8.5 are calculated for the sum of the most significant time windows extracted for each source in each category divided by the number of contributing sources. This quantity represents an average fluence upper-limit per source. These upper-limits are below the upper limits calculated for single source showing the advantage of the stacking procedure.

Source of uncertainty	Uncertainty in the parameters	Uncertainty in the neutrino event rate
Time modeling of background	-	10%
Optical properties of the ice	$\pm 10\%$	10%
DOM absolute efficiency	$\pm 10\%$	7%
Total		15.7%

Table 8.6: Summary of systematic errors. The simulation data sets for the optical properties of the ice and the DOM absolute efficiency were generated for a neutrino flux with energy spectra $\propto E^{-2}$.

8.3 Systematic Uncertainties

One of the strengths of the search methods presented in this thesis, and in general of the likelihood approaches used in point source searches within IceCube, is that the background is estimated directly from data. Since the final p-values are calculated on base of background-only pseudo-experiments they are not affected by uncertainties in the theoretical estimations of the atmospheric neutrino and muon background. However, systematic uncertainties have to be taken into account in the sensitivity and upper limits calculations since they rely on simulations of the detector response [13, 14, 15]. Table 8.6 shows the main sources of uncertainties and their effect on the neutrino event rate as calculated with dedicated simulations, with exception of the time modeling of the background which is estimated from data (see section 6.4).

The optical properties of the ice are one of the major sources of uncertainties. Uncertainties in the scattering and absorption coefficients are introduced in the modeling of dust layers and air bubbles in the bulk ice (see section 5.1.2) as well as the modeling of ice columns with different optical properties product of water refreezing on the holes made to deploy the instrumentation (borehole ice). The estimated uncertainties in the scattering and absorption coefficients is about $\pm 10\%$ [109].

The light collection efficiency of the DOM PMTs was measured in the laboratory [124]. However, this efficiency is modified once the DOMs are deployed in the ice due to effects in the trasmision of light through the borehole ice and through the boundaries with the DOM glass sphere. Therefore, the DOM efficiency is correlated with the modeling of the optical properties of the ice, but as a conservative approach they are taken as independent for the estimation of systematic uncertainities here. The estimated DOM efficiency uncertainity is about $\pm 10\%$. Adding in cuadrature the different contributions the total systematic error in the neutrino event rate is 15.7%.

In order estimate the effect of the variations of the parameteres described above on the fluence sensitivity, the full analysis chain (generation of PDFs, generation of scrambled

maps and likelihood analysis) was repeated for dedicated simulation data-sets. The fluence sensitivities were calculated for a simulated single neutrino flare of different durations and two declinations: 5° and 70°.

The results are shown in Figures 8.3 and 8.5 for simulation data-sets with three DOM efficiency values (Baseline and Baseline $\pm 10\%$) and in Figures 8.4 and 8.6 for three values of the absorption and scattering coefficients (Baseline and Baseline $\pm 10\%$). The variations in the fluence sensitivity as function of the flare duration are dominated by statistical fluctuations and are in the range $2 - 8\%$ for the considered DOM efficiency variations and in the range $3 - 4\%$ for the considered variations in the absorption and scattering coefficients.

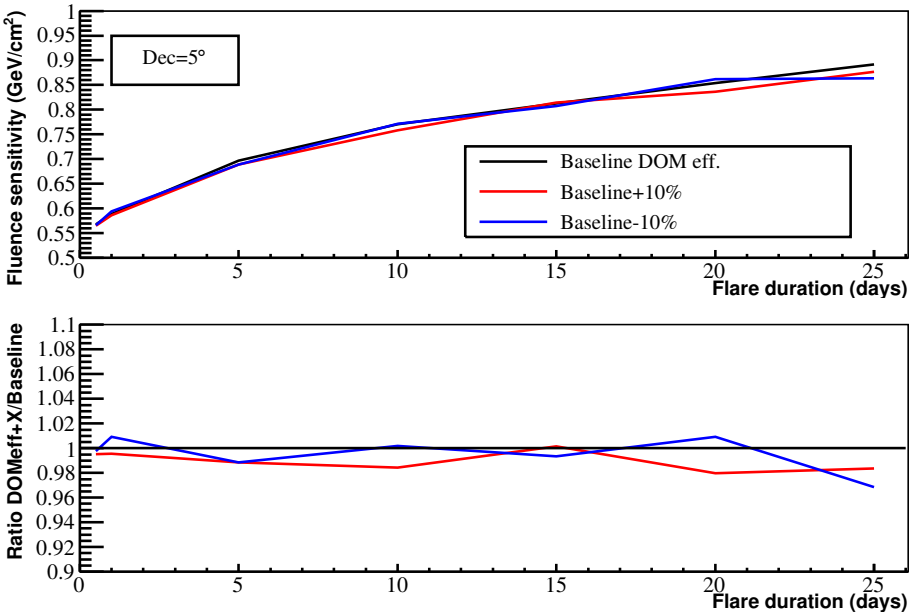

Figure 8.3: Fluence sensitivity as function of the flare duration for different simulated DOM efficiencies and a source at DEC= 5°.

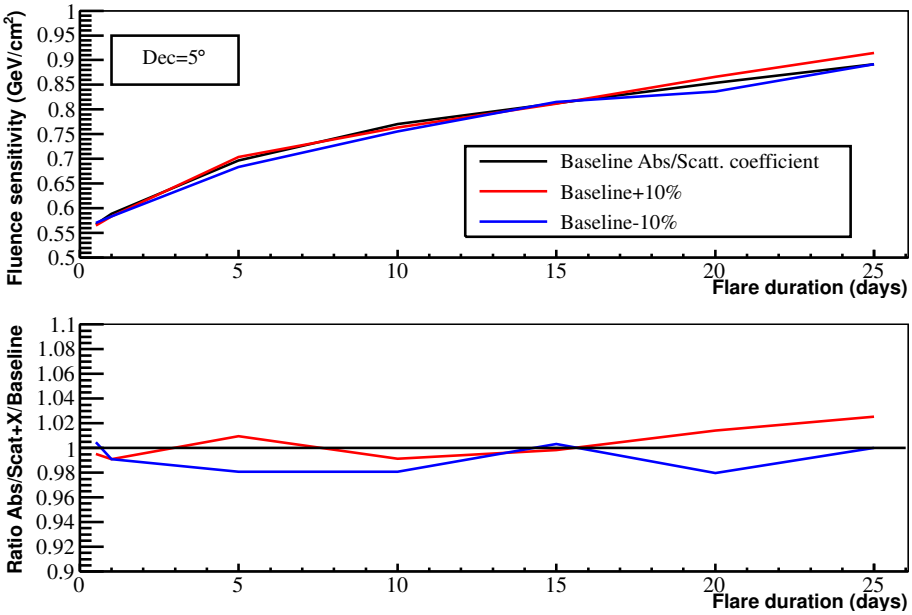

Figure 8.4: Fluence sensitivity as function of the flare duration for different simulated absorption and scattering coefficients and a source at DEC= 5°.

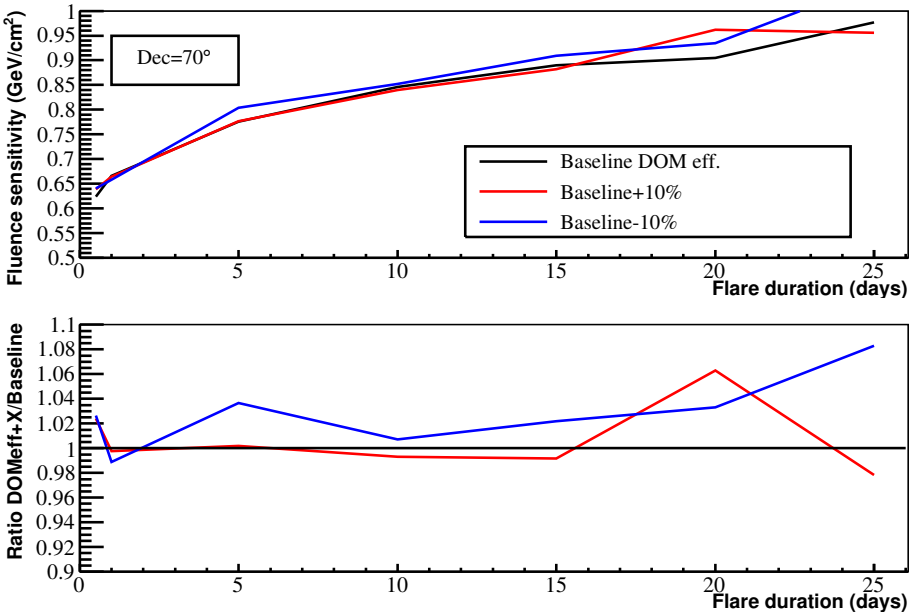

Figure 8.5: Fluence sensitivity as function of the flare duration for different simulated DOM efficiencies and a source at DEC= 70°.

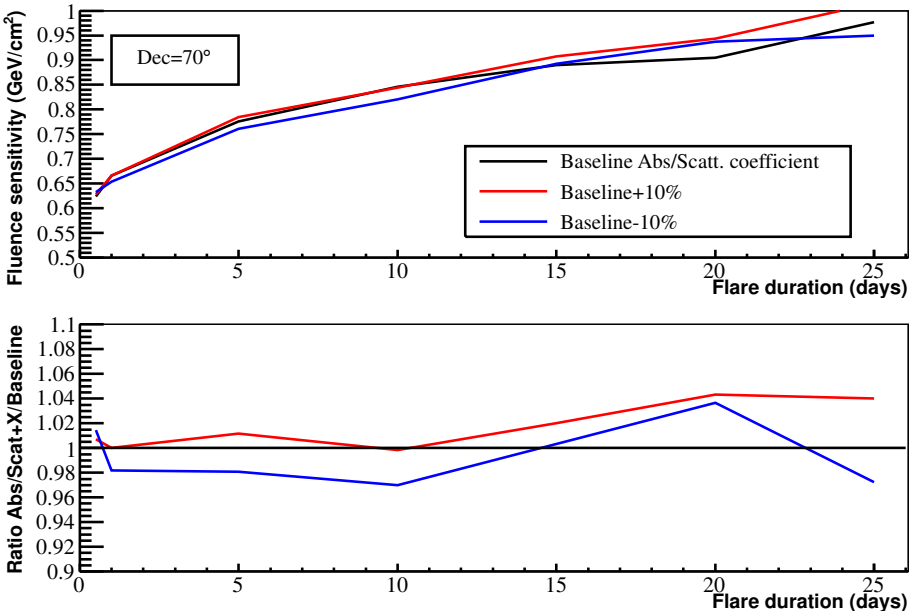

Figure 8.6: Fluence sensitivity as function of the flare duration for different simulated absorption and scattering coefficients and a source at DEC= 70°.

Chapter 9

Summary and Outlook

Active Galactic Nuclei (AGN), being known to be powerful emitters of electromagnetic radiation up to the TeV range, have been proposed as candidate sources of high-energy cosmic rays. However, there is not evidence of hadrons being accelerated in these objects yet. If high-energy hadrons interact with photon or matter fields present in the AGN vicinity, fluxes of high-energy gamma-rays and neutrinos are expected. In particular, the detection of high-energy neutrinos from these sources could provide the missing evidence.

Motivated by the extreme time variability observed at different wavelengths in AGNs, in this thesis two new methods to search for neutrino flares from selected AGNs were developed and tested with data of the IceCube Neutrino observatory: The Multi-flare and the Multi-flare stacking method. While the first method look for multiple neutrino flares from a single source the second method considers several sources in a stacking approach in order to improve the discovery potential if the sources are too week for individual detection.

The advantage of analyses that include time information is that the discovery potential improves with respect to analyses than include only space and energy information. This is because by looking at short time windows the atmospheric muon and neutrino background is reduced. Since the search methods developed here do not assume a time coincident between the possible high-energy neutrino flares and flares observed at other wavelengths, additional scenarios of neutrino emission are explored such as neutrino flares without a correlated photon counterpart or time lags between these astrophysical messengers, as suggested in some emission models. The Multi-flare method is sensitive not only to one strong flaring event, as in a single flare search, but to a set of several week flares separated in time.

It was shown that the developed methods can recover the values of the source spectral index, the flare duration, and the total number of injected signal events for several simulated examples of flaring neutrino emission. Applying these search methods to real data, no significant set of events indicating the presence of high-energy neutrino flares were found in the direction of the selected AGNs. Fluence upper limits were set for the most significant time windows found in data showing an improvement of a factor of ~ 2 with respect to previous single-flare searches [24, 22].

Even though no explicit time coincidence was assumed in the Multi-flare method, is interesting to note that from the list of selected sources for the 2011-2012 IceCube data-set, the source with the lowest p-value, the FSRQ PKS 2142-7, was also the source with the lowest p-value in a triggered analysis that builds the time PDF on base of Fermi-LAT light curves developed elsewhere [23].

After more than 5 decades after the first proposal of a neutrino telescope, the very first evidence of an astrophysical flux of high-energy neutrinos has been found with a different event selection than the used in this thesis. The IceCube Collaboration reported an excess of events above the atmospheric background at the 5.7σ level with observable energies above 100 TeV [16, 17]. No significant cluster of events in space or time was found in these analysis and therefore the sources of this astrophysical neutrino flux are still unknown. Additional years of data and planned extensions of the IceCube experiment, could provide the missing evidence to identify the sources of the observed events and provide additional information to identify the elusive sources of high-energy cosmic rays.

Bibliography

[1] J. Linsley. Evidence for a Primary Cosmic-Ray Particle with Energy 10^{20} eV. *Phys. Rev. Lett.*, 10:146–148, Feb 1963.

[2] A. Letessier-Selvon and T. Stanev. Ultrahigh energy cosmic rays. *Rev. Mod. Phys.*, 83:907–942, Sep 2011.

[3] K. Kotera and A. Olinto. The Astrophysics of Ultrahigh-Energy Cosmic Rays. *Ann. Rev. Astron. Astrophys.*, 49(1):119–153, 2011.

[4] F. Rieger. Non-thermal Processes in Black Hole-Jet Magnetospheres- Invited Review. *Int. J. Mod. Phys. D*, 20(09):1547–1596, 2011.

[5] M. Böttcher, D. Harris, and H. Krawczynski. *Relativistic jets from Active Galactic Nuclei*. Wiley-VCH, Weinheim, 2012.

[6] P. Abreu *et al.* (The Pierre Auger Collaboration). Update on the correlation of the highest energy cosmic rays with nearby extragalactic matter. *Astropart. Phys.*, 34(5):314 – 326, 2010.

[7] K. Hang and K. Jihyun. Revisit of Correlation Analysis between Active Galactic Nuclei and Ultra-High-Energy cosmic rays. *Int. J. Mod. Phys. D*, 22(08):1350045, 2013.

[8] C. Dermer and G. Menon. *High Energy Radiation from Black Holes*. Princeton University Press, 2009.

[9] M. Böttcher, A. Reimer, K. Sweeney, and A. Prakash. Leptonic and hadronic modeling of fermi-detected blazars. *Astrophys. J.*, 768(1):54, 2013.

[10] M. Ackermann *et al.* (Fermi Collaboration). Detection of the Characteristic Pion-Decay Signature in Supernova Remnants. *Science*, 339:807, 2013.

[11] U.F. Katz and C. Spiering. High-energy neutrino astrophysics: Status and perspectives. *Prog. Part. Nucl. Phys.*, 67(3):651 – 704, 2012.

[12] A. Achterberg *et. al* (IceCube Collaboration). First year performance of the IceCube neutrino telescope. *Astropart. Phys.*, 26(3):155 – 173, 2006.

[13] R. Abbasi *et al.* (IceCube Collaboration). Time-integrated Searches for Point-like Sources of Neutrinos with the 40-string IceCube Detector. *Astrophys. J.*, 732(1):18, 2011.

[14] M. Aartsen *et al.* (IceCube Collaboration). Search for Time-independent Neutrino Emission from Astrophysical Sources with 3 yr of IceCube Data. *Astrophys. J.*, 779(2):132, 2013.

[15] M. Aartsen *et al.* (IceCube Collaboration). Searches for Extended and Point-like Neutrino Sources with Four Years of IceCube Data. *Astrophys. J.*, 796(2):109, 2014.

[16] M. Aartsen *et al.* (IceCube Collaboration). Evidence for High-Energy Extraterrestrial Neutrinos at the IceCube Detector. *Science*, 342:1242856, 2013.

[17] M. Aartsen *et al.* (IceCube Collaboration). Observation of High-Energy Astrophysical Neutrinos in Three Years of IceCube Data. *Phys. Rev. Lett.*, 113:101101, Sep 2014.

[18] P. Padovani and E. Resconi. Are both bl lacs and pulsar wind nebulae the astrophysical counterparts of icecube neutrino events? *Monthly Notices of the Royal Astronomical Society*, 443(1):474–484, 2014.

[19] F. Aharonian *et al.* An Exceptional Very High Energy Gamma-Ray Flare of PKS 2155-304. *Astrophys. J. Lett.*, 664(2):L71, 2007.

[20] T. Arlen *et al.* Rapid TeV Gamma-Ray Flaring of BL Lacertae. *Astrophys. J.*, 762(2):92, 2013.

[21] A. Abdo *et al.* (Fermi Collaboration). Gamma-ray Light Curves and Variability of Bright Fermi-detected Blazars. *Astrophys. J.*, 722(1):520, 2010.

[22] R. Abbasi *et al.* (IceCube Collaboration). Time-dependent Searches for Point Sources of Neutrinos with the 40-string and 22-string Configurations of IceCube. *Astrophys. J.*, 744(1):1, 2012.

[23] M. Aartsen (IceCube Collaboration). Searches for Time-dependent Neutrino Sources with IceCube Data from 2008 to 2012. *The Astrophysical Journal*, 807(1):46, 2015.

[24] J. L. Bazo Alba. *Search for steady and flaring astrophysical neutrino point sourcs with the IceCube Detector*. PhD Thesis, Humboldt-Universitat zu Berlin, 2010.

[25] D. Gora, E. Bernardini, and A.H. Cruz-Silva. A method for untriggered time-dependent searches for multiple flares from neutrino point sources. *Astropart. Phys.*, 35(4):201 – 210, 2011.

[26] C. Dermer, E. Ramirez-Ruiz, and T. Le. Correlation of Photon and Neutrino Fluxes in Blazars and Gamma-Ray Bursts. *Astrophys. J. Lett.*, 664(2):L67, 2007.

[27] B. Eichmann, R. Schlickeiser, and W. Rhode. Differences of Leptonic and Hadronic Radiation Production in Flaring Blazars. *Astrophys. J.*, 749(2):155, 2012.

[28] J. Beringer *et al.* (Particle Data Group). Review of particle physics. *Phys. Rev. D*, 86:010001, Jul 2012.

[29] A. Hillas. Can diffusive shock acceleration in supernova remnants account for high-energy galactic cosmic rays? *J. Phys. G. Nucl. Part. Phys.*, 31(5):R95, 2005.

[30] J. R. Hoerandel, N. N. Kalmykov, and A. V. Timokhin. Propagation of super-high-energy cosmic rays in the galaxy. *Astropart. Phys.*, 27(2-3):119 – 126, 2007.

[31] M. Longair. *High Energy Astrophysics*. Cambridge University Press, 2011.

[32] J. Bluemer, R. Engel, and J. R. Horeandel. Cosmic rays from the knee to the highest energies. *Prog. Part. Nucl. Phys.*, 63(2):293 – 338, 2009.

[33] R. Aloisio, V. Berezinsky, and A. Gazizov. Transition from galactic to extragalactic cosmic rays. *Astropart. Phys.*, 39-40(0):129 – 143, 2012.

[34] K. Greisen. End to the Cosmic-Ray Spectrum? *Phys. Rev. Lett.*, 16:748–750, Apr 1966.

[35] A. Hillas. The Origin of Ultrahigh-Energy Cosmic Rays. *Ann. Rev. Astron. Astrophys.*, 22:425–444, 1984.

[36] E. Fermi. On the origin of the cosmic radiation. *Phys. Rev.*, 75:1169–1174, Apr 1949.

[37] A. R. Bell. The acceleration of cosmic rays in shock fronts. I. *MNRAS*, 182:147–156, 1978.

[38] R.D. Blandford and J.P. Ostriker. Particle Acceleration by Astrophysical Shocks. *Astrophys. J.*, 221:L29–L32, 1978.

[39] A. Achterberg, Y. A. Gallant, J. G. Kirk, and A. W. Guthmann. Particle acceleration by ultrarelativistic shocks: theory and simulations. *MNRAS*, 328(2):393–408, 2001.

[40] F. W. Stecker, M. G. Baring, and E. J. Summerlin. Blazar gamma-rays, shock acceleration, and the extragalactic background light. *Astrophys. J. Lett.*, 667(1):L29, 2007.

[41] Meli, A. and Biermann, P. L. Active galactic nuclei jets and multiple oblique shock acceleration: starved spectra. *A & A*, 556:A88, 2013.

[42] J. W. Cronin. The highest-energy cosmic rays. *Nucl. Phys. B - Proc. Supp.*, 138(0):465 – 491, 2005.

[43] M. Kachelrieß, E. Parizot, and D.V. Semikoz. The GZK horizon and constraints on the cosmic ray source spectrum from observations in the GZK regime. *JETP Lett.*, 88(9):553–557, 2008.

[44] J. Abraham *et al.* (The Pierre Auger Collaboration). Correlation of the highest-energy cosmic rays with the positions of nearby Active Galactic Nuclei. *Astropart. Phys.*, 29(3):188 – 204, 2008.

[45] R. Abbasi *et al.* (HiRes Collaboration). Search for correlations between hires stereo events and active galactic nuclei. *Astropart. Phys.*, 30(4):175 – 179, 2008.

[46] S. R. Kelner and F. A. Aharonian. Energy spectra of gamma rays, electrons, and neutrinos produced at interactions of relativistic protons with low energy radiation. *Phys. Rev. D*, 78:034013, Aug 2008.

[47] A. Mücke, R. Engel, J. Rachen, R. Protheroe, and T. Stanev. Monte carlo simulations of photohadronic processes in astrophysics. *Comput. Phys. Commun.*, 124(2-3):290 – 314, 2000.

[48] S. Hummer, M. Ruger, F. Spanier, and W. Winter. Simplified Models for Photohadronic Interactions in Cosmic Accelerators. *Astrophys. J.*, 721(1):630, 2010.

[49] S. Hummer, M. Maltoni, W. Winter, and C. Yaguna. Energy dependent neutrino flavor ratios from generic cosmic accelerators on the HILLAS plot. *Astropart. Phys.*, 34:205–224, 2010.

[50] S. R. Kelner, F. A. Aharonian, and V. V. Bugayov. Energy spectra of gamma rays, electrons, and neutrinos produced at proton-proton interactions in the very high energy regime. *Phys. Rev. D*, 74:034018, Aug 2006.

[51] A. Mücke, R. Protheroe, R. Engel, J. Rachen, and T. Stanev. Bl-lac objects in the synchrotron proton blazar model. *Astropart. Phys.*, 18(6):593 – 613, 2003.

[52] P. Lipari, M. Lusignoli, and D. Meloni. Flavor Composition and Energy Spectrum of Astrophysical Neutrinos. *Phys.Rev.*, D75:123005, 2007.

[53] S. Pakvasa. Neutrino Flavor Detection at Neutrino Telescopes and Its Uses. astro-ph/1004.5413, 2010.

[54] M. Aartsen *et al.* (IceCube Collaboration). Flavor Ratio of Astrophysical Neutrinos above 35 TeV in IceCube. *Phys. Rev. Lett.*, 114:171102, Apr 2015.

[55] F. Rieger, E. de Ona-Wilhelmi, and F. Aharonian. TeV astronomy. *Front. Phys.*, 8(6):714–747, 2013.

[56] S. Adrián-Martínez *et al.* (ANTARES Collaboration). Searches for Point-like and Extended Neutrino Sources Close to the Galactic Center Using the ANTARES Neutrino Telescope. *Astrophys. J. Lett.*, 786(1):L5, 2014.

[57] F. Halzen, H. Landsman, and T. Montaruli. TeV photons and neutrinos from giant soft-gamma repeaters flares. astro-ph/0503348, 2005.

[58] B. Zhang, Z. Dai, P. Mészáros, E. Waxman, and A. K. Harding. High-energy neutrinos from magnetars. *Astrophys. J.*, 595(1):346, 2003.

[59] D. Band, J. Matteson, L. Ford, B. Schaefer, D. Palmer, et al. BATSE observations of gamma-ray burst spectra. 1. Spectral diversity. *Astrophys.J.*, 413:281–292, 1993.

[60] N. Gehrels, E. Ramirez-Ruiz, and D. B. Fox. Gamma-Ray Bursts in the Swift Era. *ARAA*, 47:567–617, September 2009.

[61] E. Waxman and J. Bahcall. High energy neutrinos from cosmological gamma-ray burst fireballs. *Phys. Rev. Lett.*, 78:2292–2295, Mar 1997.

[62] J. K. Becker. High-energy neutrinos in the context of multimessenger astrophysics. *Phys. Rep.*, 458(4-5):173 – 246, 2008.

[63] R. Abbasi et al. An absence of neutrinos associated with cosmic-ray acceleration in γ-ray bursts. *Nature*, 484:351–353, 2012.

[64] S. Hümmer, P. Baerwald, and W. Winter. Neutrino Emission from Gamma-Ray Burst Fireballs, Revised. *Phys. Rev. Lett.*, 108:231101, Jun 2012.

[65] B. C. Lacki, T. A. Thompson, E. Quataert, A. Loeb, and E. Waxman. On The GeV & TeV Detections of the Starburst Galaxies M82 & NGC 253. *Astrophys.J.*, 734:107, 2011.

[66] I. Yoshiyuki. High Energy Gamma-ray Absorption and Cascade Emission in Nearby Starburst Galaxies. *Astrophys.J.*, 728:11, 2011.

[67] G. E. Romero and D. F. Torres. Signatures of hadronic cosmic rays in starbursts? high-energy photons and neutrinos from ngc 253. *Astrophys. J. Lett.*, 586(1):L33, 2003.

[68] K. Murase. High-energy neutrinos from extragalactic cosmic-ray sources. *Nucl. Phys. B - Proc. Supp.*, 217(1):291 – 293, 2011.

[69] K. Murase, J. F. Beacom, and H. Takami. Gamma-ray and neutrino backgrounds as probes of the high-energy universe: hints of cascades, general constraints, and implications for TeV searches. *J. Cosmology & Astro-Part. Phys.*, 2012(08):030, 2012.

[70] G. Brunetti and T. W. Jones. Cosmic rays in galaxy clusters and their nonthermal emission. *Int. J. Mod. Phys. D*, 23(4):1430007, 2014.

[71] M. Schmidt. 3C 273 : A Star-Like Object with Large Red-Shift. *Nature*, 197:1040, March 1963.

[72] C. M. Urry and P. Padovani. Unified Schemes for Radio-Loud Active Galactic Nuclei. *Publications of the Astronomical Society of the Pacific*, 107:803, September 1995.

[73] J. Bennet, M. Donahue, N. Schneider, and M. Volt. *The Cosmic Perspective: Stars and Galaxies. 7th edition*. Addison-Wesley, 2013.

[74] P. Padovani. High-energy emission from AGN and unified schemes. astro-ph/9901130, 1999.

[75] Zhaohui S. *et al.* Quasars and the Big Blue Bump. *Astrophys. J.*, 619(1):41, 2005.

[76] M. Böttcher. Modeling the emission processes in blazars. *Astrophysics and Space Science*, 309(1-4):95–104, 2007.

[77] M. Böttcher, A. Reimer, K. Sweeney, and A. Prakash. Leptonic and hadronic modeling of fermi-detected blazars. *Astrophys. J.*, 768(1):54, 2013.

[78] A. Reimer. Hadron-initiated emission processes in blazar jets. *Int. J. Mod. Phys. D*, 18(10):1511–1515, 2009.

[79] W. Bednarek and R. Protheroe. Gamma-ray and neutrino flares produced by protons accelerated on an accretion disc surface in active galactic nuclei. *MNRAS*, 302(2):373–380, 1999.

[80] A. Neronov and D. Semikoz. Which blazars are neutrino loud? *Phys. Rev. D*, 66:123003, Dec 2002.

[81] A. Atoyan and C. Dermer. High-energy neutrinos from photomeson processes in blazars. *Phys. Rev. Lett.*, 87:221102, Nov 2001.

[82] A. Atoyan and C. Dermer. Neutral beams from blazar jets. *Astrophys. J.*, 586(1):79, 2003.

[83] A. Atoyan and C. Dermer. Neutrinos and gamma-rays of hadronic origin from agn jets. *New Astronomy Reviews*, 48(5-6):381 – 386, 2004.

[84] A. Abdo *et al.* (Fermi Collaboration). Spectral Properties of Bright Fermi-Detected Blazars in the Gamma-Ray Band. *Astrophys. J.*, 710(2):1271, 2010.

[85] A. Neronov and M. Ribordy. IceCube sensitivity for neutrino flux from Fermi blazars in quiescent states. *Phys. Rev. D*, 80:083008, Oct 2009.

[86] R. Protheroe. High-energy neutrinos from blazars. *ASP Conf.Ser.*, 121:585, 1997.

[87] R. Chatterjee, C. D. Bailyn, E. W. Bonning, M. Buxton, P. Coppi, G. Fossati, J. Isler, L. Maraschi, and C. M. Urry. Similarity of the Optical-Infrared and Gamma-Ray Time Variability of Fermi Blazars. *Astrophys. J.*, 749(2):191, 2012.

[88] T. *et al.* Hovatta. Connection between optical and γ-ray variability in blazars. *Mon. Not. Roy. Astron. Soc.*, 439(1):690–702, 2014.

[89] D. Cohen *et al.* Temporal Correlations between optical and gamma-ray activity in Blazars. *Astrophys. J.*, 797(137):11, 2014.

[90] M. Böttcher and C. Dermer. Timing Signatures of the Internal-Shock Model for Blazars. *Astrophys. J.*, 711(1):445, 2010.

[91] J. León-Tavares *et al.* The connection between gamma-ray emission and millimeter flares in Fermi/LAT blazars. *A&A*, 532:A146, 2011.

[92] A. Reimer, M. Böttcher, and S. Postnikov. Neutrino Emission in the Hadronic Synchrotron Mirror Model: The "Orphan" TeV Flare from 1ES 1959+650. *Astrophys. J.*, 630(1):186, 2005.

[93] M. Böttcher and C. Dermer. Timing Signatures of the Internal-Shock Model for Blazars. *Astrophys. J.*, 711(1):445, 2010.

[94] R. Chatterjee *et al.* Similarity of the Optical-Infrared and Gamma-Ray Time Variability of Fermi Blazars. *Astrophys. J.*, 749(2):191, 2012.

[95] M. Böttcher. Models for the Spectral Energy Distributions and Variability of Blazars. astro.ph/1006.5048, 2010.

[96] M. Weidinger *et al.* Hadronic Modeling of AGN variability. *Int. J. Mod. Phys.*, 8:293–298, 2012.

[97] P. L. Nolan *et al.* (Fermi Collaboration). Fermi Large Area Telescope Second Source Catalog. *Astrophys. J. Supplement Series*, 199(2):31, 2012.

[98] R. Rutledge. The Astronomer's Telegram: A Web-based Short-Notice Publication System for the Professional Astronomical Community. http://www.astronomerstelegram.org/. *Publ.Astron.Soc.Pac.*, 110:754, 1998.

[99] C. Giunti and C. W. Kim. *Fundamentals of Neutrino Physics and Astrophysics*. Oxford University Press, Oxford, UK, 2007. ISBN 978-0-19-850871-7.

[100] M.C. Gonzalez-Garcia and M. Maltoni. Phenomenology with massive neutrinos. *Phys. Rep.*, 460(1-3):1–129, 2008.

[101] M. Aartsen *et al.* (IceCube Collaboration). Determining neutrino oscillation parameters from atmospheric muon neutrino disappearance with three years of IceCube DeepCore data. *Phys. Rev. D*, 91:072004, Apr 2015.

[102] H. Athar, M. Jeżabek, and O. Yasuda. Effects of neutrino mixing on high-energy cosmic neutrino flux. *Phys. Rev. D*, 62:103007, Oct 2000.

[103] L. Anchordoqui. Cosmic neutrino pevatrons: A brand new pathway to astronomy, astrophysics, and particle physics. *Journal of High Energy Astrophysics*, 1-2(0):1 – 30, 2014.

[104] V. Barger, Lingjun Fu, G. Learned, J. D. Marfatia, S. Pakvasa, and J. Weiler, T.˙ Glashow resonance as a window into cosmic neutrino sources. *Phys. Rev. D*, 90:121301, Dec 2014.

[105] S. L. Glashow. Resonant scattering of antineutrinos. *Phys. Rev.*, 118:316–317, Apr 1960.

[106] J. Formaggio and G. Zeller. From eV to EeV: Neutrino cross sections across energy scales. *Rev. Mod. Phys.*, 84:1307–1341, Sep 2012.

[107] A. L'Abbate, T. Montaruli, and I. Sokalski. Effect of neutral current interactions on high energy muon and electron neutrino propagation through the earth. *Astropart.Phys.*, 23:57–63, 2005.

[108] D. Groom, N. Mokhov, and S. Striganov. Muon Stopping Power And Range Tables 10 MeV-100 TeV. *At. Data Nucl. Data Tables*, 78(2):183 – 356, 2001.

[109] M. Ackermann *et al.* (IceCube Collaboration). Optical properties of deep glacial ice at the South Pole. *J. Geophys. Res.*, 111(D13), 2006.

[110] J.G. Learned and K. Mannheim. High-energy neutrino astrophysics. *Ann. Rev. Nucl. Part. Sci.*, 50:679–749, 2000.

[111] J. Ahrens *et al.* (IceCube Collaboration). Sensitivity of the icecube detector to astrophysical sources of high energy muon neutrinos. *Astropart. Phys.*, 20(5):507 – 532, 2004.

[112] F. Halzen and A. O'Murchadha. Neutrinos from Auger Sources. astro-ph/0802.0887, 2008.

[113] R. Abbasi *et al.* (IceCube Collaboration). Measurement of the atmospheric neutrino energy spectrum from 100 GeV to 400 TeV with IceCube. *Phys. Rev. D*, 83:012001, Jan 2011.

[114] P. Desiati and T. Gaisser. Seasonal variation of atmospheric leptons as a probe of charm. *Phys. Rev. Lett.*, 105:121102, Sep 2010.

[115] M. Aartsen *et al.* (IceCube Collaboration). Measurement of the Atmospheric ν_e Flux in IceCube. *Phys. Rev. Lett.*, 110:151105, Apr 2013.

[116] R. Enberg, M. Reno, and I. Sarcevic. Prompt neutrino fluxes from atmospheric charm. *Phys. Rev. D*, 78:043005, Aug 2008.

[117] M. Honda, T. Kajita, K. Kasahara, S. Midorikawa, and T. Sanuki. Calculation of atmospheric neutrino flux using the interaction model calibrated with atmospheric muon data. *Phys. Rev. D*, 75:043006, Feb 2007.

[118] M. Ackerman. *Searches for signals from cosmic point-like sources of highenergy neutrinos in 5 years of AMANDA-II data*. PhD Thesis, Humboldt-Universitat zu Berlin, 2006.

[119] J. Braun, J. Dumm, F. De Palma, C. Finley, A. Karle, and T. Montaruli. Methods for point source analysis in high energy neutrino telescopes. *Astropart. Phys.*, 29(4):299 – 305, 2008.

[120] R. Abbasi *et al.* (IceCube Collaboration). IceTop: The surface component of IceCube. *Nucl. Instrum. Meth. A*, 700(0):188 – 220, 2013.

[121] R. Abbasi *et al.* (IceCube Collaboration). All-particle cosmic ray energy spectrum measured with 26 IceTop stations. *Astropart. Phys.*, 44(0):40 – 58, 2013.

[122] Hamamatsu Photonics K.K. Editorial Committee. *Photo-multiplier tubes. Basics and applications*. Hamamatsu Photonics K.K, 2006.

[123] R. Abbasi *et al.* (IceCube Collaboration). The design and performance of IceCube DeepCore. *Astropart. Phys.*, 35(10):615 – 624, 2012.

[124] R. Abbasi *et al.* (IceCube Collaboration). Calibration and characterization of the IceCube photomultiplier tube. *Nucl. Instrum. Meth. A*, 618(1-3):139 – 152, 2010.

[125] R. Abbasi *et al.* (IceCube Collaboration). The IceCube data acquisition system: Signal capture, digitization, and timestamping. *Nucl. Instrum. Meth. A*, 601(3):294 – 316, 2009.

[126] K. Hanson and O. Tarasova (IceCube Collaboration). Design and production of the icecube digital optical module. *Nucl. Instrum. Meth. A*, 567(1):214 – 217, 2006.

[127] M. Aartsen *et al.* (IceCube Collaboration). Measurement of South Pole ice transparency with the IceCube LED calibration system. *Nucl. Instrum. Meth. A.*, 711(0):73 – 89, 2013.

[128] N. Whitehorn. *A Search for High-Energy Neutrino Emission from Gamma-Ray Bursts*. PhD Thesis, University of Wisconsin-Madison, 2014.

[129] J. Ahrens *et al.* (AMANDA Collaboration). Muon track reconstruction and data selection techniques in AMANDA. *Nucl. Instrum. Meth. A*, 524(1-3):169 – 194, 2004.

[130] G. Japaridze and M. Ribordy. Realistic arrival time distribution from an isotropic light source. arXiv:astro-ph/0506136v1, 2005.

[131] T. Neunhoffer. Estimating the angular resolution of tracks in neutrino telescopes based on a likelihood analysis. *Astropart. Phys.*, 25(3):220 – 225, 2006.

[132] M. Aartsen *et al.* (IceCube Collaboration). Observation of the cosmic-ray shadow of the Moon with IceCube. *Phys. Rev. D*, 89:102004, May 2014.

[133] M. Aartsen *et al.* (IceCube Collaboration). Energy reconstruction methods in the IceCube neutrino telescope. *JINST*, 9(03):P03009, 2014.

[134] S. Odrowski. *High-Energy Neutrino Scan of the Galactic Plane*. PhD Thesis, Max-Planck-Institut fur Kernphysik, Ruperto-Carola University of Heidelberg, 2012.

[135] M. Baker. *Time-Dependent Searches for Neutrino Point Sources with the IceCube Observatory*. PhD Thesis, University of Wisconsin, Madison,, 2011.

[136] G. Bohm and Z. Gunter. *Introduction to Statistics and Data Analysis for Physicists*. Verlag Deutsches Elektronen-Synchrotron, 2010.

[137] G. Hill and K. Rawlins. Unbiased cut selection for optimal upper limits in neutrino detectors: the model rejection potential technique. *Astropart. Phys.*, 19(3):393 – 402, 2003.

[138] E. Gross and O. Vitells. Trial factors for the look elsewhere effect in high energy physics. *The European Physical Journal C*, 70(1-2):525–530, 2010.

[139] R. Lauer. *Extending the search for cosmic point sources of neutrinos with IceCube beyond PeV energies and above the horizon*. PhD Thesis, Humboldt-Universitat zu Berlin, 2009.

[140] J. Braun, M. Baker, J. Dumm, C. Finley, A. Karle, and T. Montaruli. Time-dependent point source search methods in high energy neutrino astronomy. *Astropart. Phys.*, 33(3):175 – 181, 2010.

[141] M. Baker, J.A. Aguilar, J. Dumm, N. Kurahashi, and T. Montaruli. Searches for time-variable neutrino point sources with the icecube observatory. *Proc. 32nd ICRC*, 2011.

[142] R. Franke and E. Bernardini. Neutrino triggered high-energy gamma-ray follow-up with icecube. *Proc. 32nd ICRC*, 2011.

[143] R. Franke. *Design, Implementation and First Results of the Neutrino Triggered Target of Opportunity Program with the IceCube Neutrino Telescope*. PhD Thesis, Humboldt-Universitat zu Berlin, 2014.

[144] W. Winter. Interpretation of neutrino flux limits from neutrino telescopes on the Hillas plot. *Phys. Rev. D*, 85:023013, Jan 2012.

[145] C. Diltz and M. Böttcher. Time dependent leptonic modeling of fermi ii processes in the jets of flat spectrum radio quasars. *Journal of High Energy Astrophysics*, 1-2(0):63 – 70, 2014.

[146] A. Abdo *et al.* (Fermi Collaboration). A change in the optical polarization associated with a gamma-ray flare in the blazar 3C-279. *Nature*, 463(7283):919, 2010.

[147] C. Walck. *HandBook of Statistical Distributions for Experimentalists*. Internal Report SUF-PFY/96-01, 2007.

List of Figures

List of Tables

Acknowledgments

I would like to thank in first place to my supervisor Elisa Bernardini and to Hermann Kolanoski and Christian Spiering for giving me the chance to be part of the IceCube Collaboration. I thank Elisa Bernardini for her strong support and guidance specially in though moments.

I thank Jose Luis Bazo for helping me getting started in the first months at DESY. I thank specially Dariuz Gora for his support, countless hours of discussion and deep physics and technical insights without which the methods presented in this thesis would not exist.

I thank all the people at the DESY-Zeuthen group, specially Markus Ackermann, Thorsten Glüsenkamp, Arne Shönwald and Robert Franke who were always available to discuss physics/technical stuff and provided a very nice working atmosphere.

My gratitude goes specially to Juan Pablo Yañez and David Altmann for the extra push during the last months of the thesis writing. I thank Rolf Buehler and Johannes Knapp for proof-reading the thesis in a very short time frame and for provide me useful comments.

I thank the members of the point-source group who helped in polish and carry to an end the analyses presented here. Specially my gratitude goes to the Chad Finley and Naoko Kurahashi. I also thank Mike Richman, Juan Antonio Aguilar, Erik Blaufuss, Asen Chistov, Jhon Felde, David Boersma and Julia Tjus for accepting being referees of the analysis and provide useful insights.

Finally, I would like to thank my family who always supported me from Colombia. This thesis is dedicated to them.

Selbständigkeitserklärung

Ich erkläre, dass ich die Dissertation selbständig und nur unter Verwendung der von mir gemäß § 7 Abs. 3 der Promotionsordnung der Mathematisch-Naturwissenschaftlichen Fakultät, veröffentlicht im Amtlichen Mitteilungsblatt der Humboldt-Universität zu Berlin Nr. 126/2014 am 18.11.2014 angegebenen Hilfsmittel angefertigt habe.

Berlin, den 04.08.2015 Angel Humberto Cruz Silva